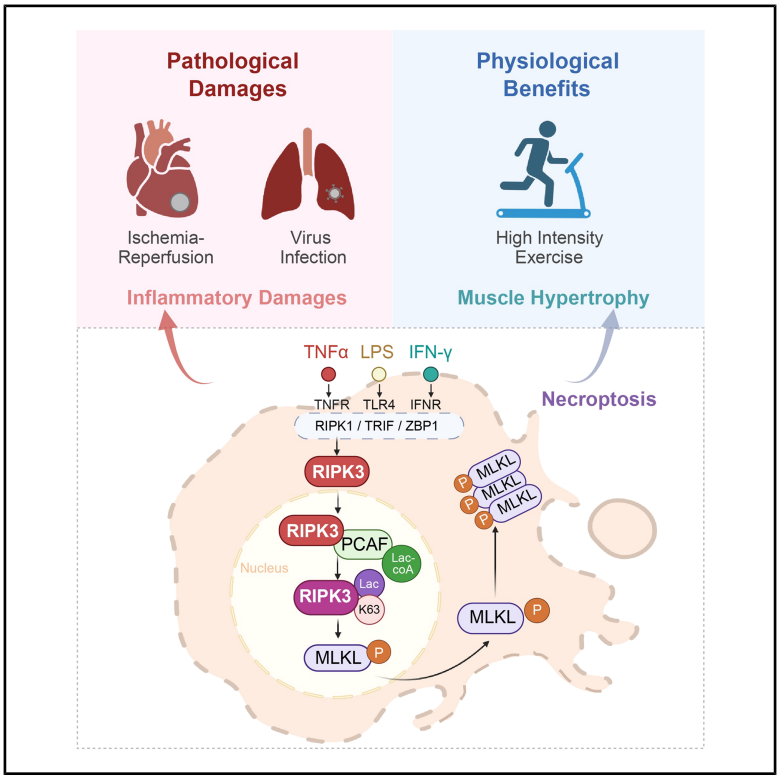
Cell Metabolism

Article

Lactate couples metabolic state to necroptosis across pathological and physiological conditions

Graphical abstract



Highlights

- Lactate homeostasis regulates necroptosis through RIPK3 lactylation at lysine 63 (K63)
- PCAF-mediated RIPK3-K63 lactylation enhances kinase activity
- RIPK3-K63 lactylation blockade protects against ischemia-reperfusion and viral injury
- Exercise-induced lactate drives RIPK3-K63 lactylation to promote muscle remodeling

Authors

Naijin Zhang, Xinyue Huang, Saien Lu, ..., Liu Cao, Liming Sun, Yingxian Sun

Correspondence

liming.sun@sibcb.ac.cn (L.S.), yxsun@cmu.edu.cn (Y.S.)

In brief

Zhang et al. show that lactate regulates necroptosis via RIPK3 lactylation at lysine 63, enhancing kinase activity. This drives tissue injury in ischemia-reperfusion and viral infection, while exercise-induced lactate uses the same mechanism to support muscle remodeling, revealing lactate-promoted necroptosis as key to both pathological and physiological processes.

Zhang et al., 2026, Cell Metabolism *38*, 2036–2053
October 6, 2026 © 2026 Elsevier Inc. All rights are reserved, including those for text and data mining, AI training, and similar technologies.
https://doi.org/10.1016/j.cmet.2026.08.022

CellPress

CellPress

Cell Metabolism

Article

Lactate couples metabolic state to necroptosis across pathological and physiological conditions

Naijin Zhang,[1,2,3,8] Xinyue Huang,[1,2,8] Saien Lu,[1,2,8] Yuanming Zou,[1,2,4,8] Guozhe Sun,[1,2,8] Wei Zhang,[5] Huijun Lu,[6] Limin Wang,[5] Xinxin Lu,[1,2] Zhaobo Zhang,[1,2] Cheng Cheng,[1,2] Shilong You,[1,2] He Zhang,[6] Ying Zhang,[1,2] Pengbo Wang,[1,2] Pan Zhou,[1,2] Juan Luo,[1,2] Yuyi Chen,[1,2] Feng Wu,[1,2] Jiayan Guo,[1,2] Anqi Ning,[1,2] Yushan Guo,[1,2] Liu Cao,[2] Liming Sun,[5,9,*] and Yingxian Sun[1,2,7,*]

[1]Department of Cardiology, The First Hospital of China Medical University, Shenyang, Liaoning, China
[2]Institute of Health Sciences, China Medical University, Shenyang 110122, Liaoning, China
[3]Department of Central Laboratory, the First Hospital of China Medical University, Shenyang, China
[4]Division of Cardiology, State Key Laboratory of Systems Medicine for Cancer, Renji Hospital, School of Medicine, Shanghai Jiao Tong University, 160 Pujian Road, Shanghai 200127, China
[5]Center for Excellence in Molecular Cell Science, Chinese Academy of Sciences, Shanghai, China
[6]Key Laboratory of Jilin Province for Zoonoses Prevention and Control, State Key Laboratory of Pathogen and Biosecurity, Academy of Military Medical Sciences, Changchun, Jilin, China
[7]Key Laboratory of Environmental Stress and Chronic Disease Control and Prevention, Ministry of Education, China Medical University, Shenyang, Liaoning, China
[8]These authors contributed equally
[9]Lead contact
*Correspondence: liming.sun@sibcb.ac.cn (L.S.), yxsun@cmu.edu.cn (Y.S.)
https://doi.org/10.1016/j.cmet.2026.08.022

SUMMARY

How fluctuations in central metabolites are transduced into cell-death decisions remains poorly understood. Here we show that lactate directly promotes necroptosis through lactylation of receptor-interacting protein kinase 3 (RIPK3) at lysine 63 (K63). Large-scale screening identified LDH inhibition as a suppressor of mixed lineage kinase domain-like pseudokinase (MLKL)-dependent necroptosis, implicating intracellular lactate as a pivotal modulator. PCAF-mediated K63 lactylation enhances RIPK3 kinase activity and stabilizes the RIPK3-MLKL complex, driving membrane disruption. K63R mutation or PCAF loss potently suppresses necroptosis. This pathway operates in both pathological and physiological contexts: K63R knockin mice and LDH/PCAF inhibition protect against injury in myocardial ischemia-reperfusion and influenza A infection, whereas exercise-induced lactate engages the identical cascade to drive myofiber necroptosis, activating muscle stem cells and enhancing athletic performance. These findings reveal RIPK3-K63 lactylation as a pivotal mechanism linking lactate fluctuations to cell-death outcomes across disease and physiology.

INTRODUCTION

Programmed cell death plays a key role in balancing cell survival and proliferation during development and disease.[1,2] Necroptosis is a membrane-lytic form of programmed cell death characterized by organelle swelling, cell enlargement, and plasma membrane rupture, leading to the release of damage-associated molecular patterns (DAMPs).[3] Although necroptosis deficiency does not cause major developmental defects, uncontrolled necroptosis drives inflammatory pathologies, including systemic inflammatory response syndrome (SIRS), ischemia-reperfusion (I/R) injury, and pulmonary damage during influenza virus infection.[4–7] Conversely, under physiological conditions, necroptotic myofibers release tenascin-C (TNC) to activate muscle stem cells (MuSCs) and promote tissue regeneration following acute injury.[8] Necroptosis therefore occupies a dual role in adult health, acting as both a pathological instigator and a physiological regulator depending on context.

At the molecular level, necroptosis is executed through a tightly regulated signaling cascade. It can be activated by the ligation of death receptors, such as tumor necrosis factor receptor (TNFR), TNF-related apoptosis-inducing ligand receptor (TRAILR), and Fas cell surface death receptor (FAS).[9] Alternatively, it can be initiated by left-handed structured Z-form RNA (zRNA) or Z-form DNA (zDNA), which are predominantly of viral origin.[10] Regardless of the initiating signals, necroptotic cells ultimately undergo plasma membrane rupture mediated by the cell-intrinsic membrane-damaging protein mixed lineage kinase domain-like pseudokinase (MLKL).[11–17] Activation of MLKL is central to the execution of necroptosis and occurs through phosphorylation by receptor-interacting protein kinase 3 (RIPK3) on MLKL's C-terminal pseudokinase domain, relieving

All rights are reserved, including those for text and data mining, AI training, and similar technologies.

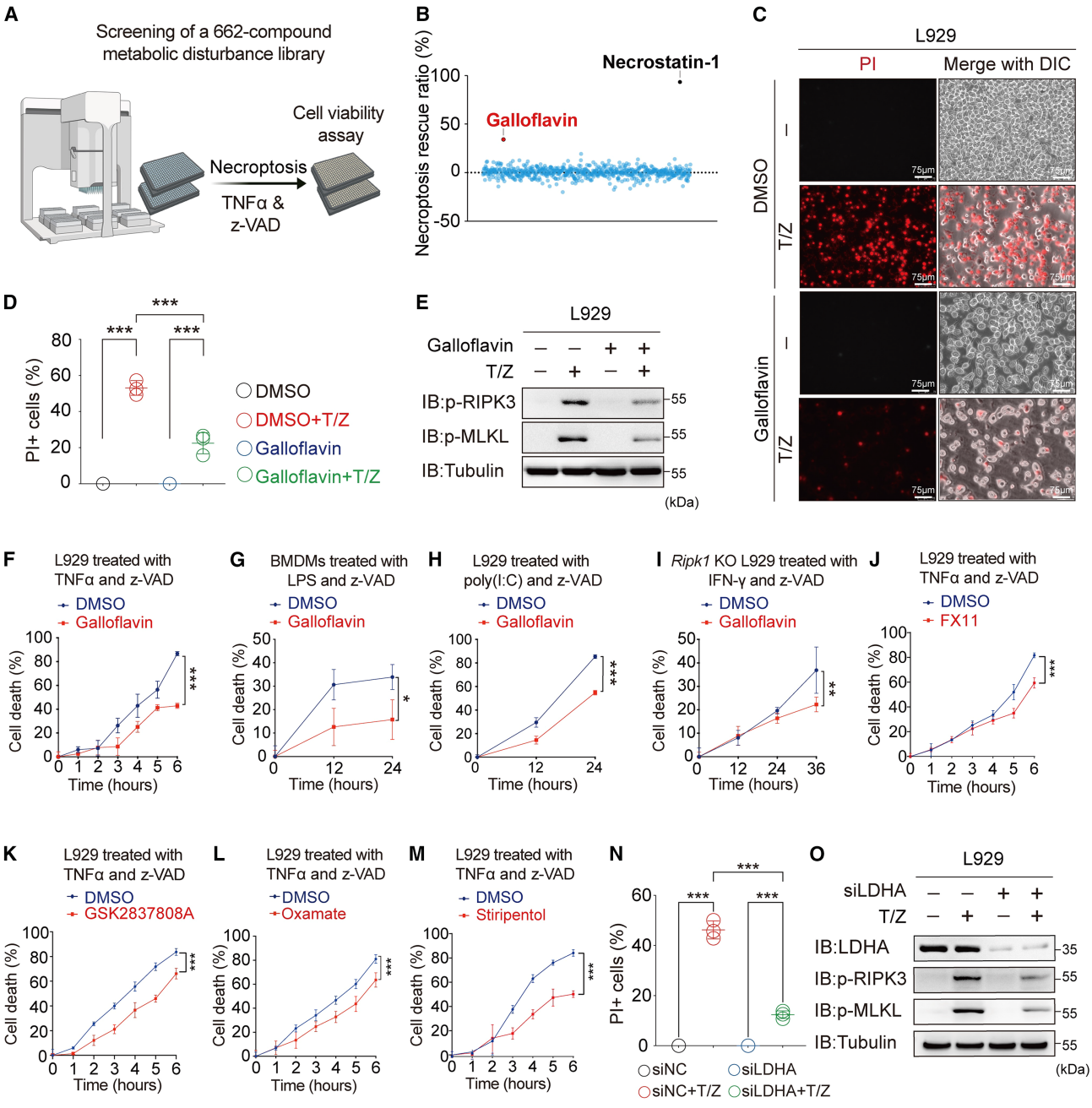


Figure 1. Lactate dysregulation inhibits necroptosis

(A) Screening of a library containing 662 metabolic compounds to identify necroptosis regulators. L929 cells were seeded in 96-well plates and pretreated with compounds (10 μM) for 12 h, followed by T/Z treatment (TNF-α: 50 ng/mL; z-VAD: 20 μM) to induce necroptosis. Cell viability was measured via ATP levels after 6 h.

(B) The LDH inhibitor galloflavin was identified as an effective necroptosis inhibitor. Nec-1 (10 μM), a known necroptosis inhibitor, was used as a positive control.

(C) Representative fluorescence microscopy images of L929 cells stained with propidium iodide (PI) to visualize necroptotic cells. Cells were treated with DMSO or galloflavin (100 μM) for 24 h, followed by treatment with or without T/Z for 3 h to induce necroptosis. Plasma membrane breakdown was detected by PI staining. Scale bar: 75 μm.

(D) Quantification of PI-positive cells shown in (C) was performed using ImageJ.

(E) Immunoblot analysis of p-RIPK3 and p-MLKL levels in L929 cells pretreated with DMSO or galloflavin (100 μM) for 24 h, followed by treatment with or without T/Z for 6 h. Tubulin was used as a loading control.

(F–I) Time course analysis of necroptosis in cells pretreated with DMSO or galloflavin (100 μM, 24 h), followed by induction with: (F) T/Z in L929 cells; (G) LPS + z-VAD in bone marrow-derived macrophages (BMDMs); (H) poly(I:C) + z-VAD in L929 cells; and (I) IFN-γ + z-VAD in *Ripk1*-knockout L929 cells. Cell viability was assessed by ATP levels.

(legend continued on next page)

its autoinhibition.[18] RIPK3 activation depends on the recruitment of upstream adaptor proteins, including receptor-interacting protein kinase 1 (RIPK1), Toll/interleukin-1 receptor domain-containing adaptor-inducing interferon-β (TRIF), and Z-DNA binding protein 1 (ZBP1), which facilitate its kinase activity.[19–21] Because RIPK3 sits at the convergence point of multiple necroptotic stimuli, its regulation is central to controlling the cell-death outcome.

Metabolic homeostasis in adults fluctuates continuously with diet, physical activity, and pathological stress, yet how such fluctuations are transduced into necroptotic signaling decisions remains unknown. Lactate, generated during glycolysis by lactate dehydrogenase A (LDHA), accumulates under high metabolic demand conditions and provides a compelling candidate for such a link—but whether elevated lactate could directly instruct necroptotic cell-death decisions has never been explored. During myocardial I/R injury, lactate accumulates to pathological levels; phosphorylated MLKL (p-MLKL), the hallmark of necroptosis execution, has been detected in the failing hearts of patients,[22] and necroptosis-driven DAMP release amplifies cardiac damage and inflammation.[23,24] In influenza A virus (IAV) infection, dysregulated lactate production coincides with RIPK3-MLKL-dependent lung injury and excessive immune activation.[25–28] At the same time, during high-intensity exercise, lactate rises as a normal physiological byproduct of anaerobic metabolism and has been positively correlated with muscle hypertrophy, though the underlying mechanism has remained unresolved.[29] Recent findings that necroptotic myofibers promote muscle regeneration after acute injury raise the intriguing possibility that exercise-induced lactate elevation and myofiber necroptosis may be mechanistically coupled—functioning as an adaptive rather than destructive event.[8]

Together, these observations suggest a unifying hypothesis: that lactate fluctuations, both pathological and physiological, are decoded by the necroptotic machinery to produce context-dependent cell-death outcomes. Here we identify the molecular mechanism linking these two phenomena. By screening a library of 662 metabolic interference compounds, we discovered that LDHA inhibition suppresses MLKL-dependent necroptosis across multiple stimuli, implicating intracellular lactate as a direct modulator of this pathway. We show that lactate drives necroptosis through lactylation of RIPK3 at lysine 63 (K63), a modification catalyzed by the nuclear lactyltransferase PCAF (P300/CBP-associated factor) that enhances RIPK3 kinase activity and stabilizes the RIPK3-MLKL complex. This finding also provides a mechanistic explanation for how nuclear-translocated RIPK3 promotes a process that is predominantly executed in the cytoplasm.[30–32] Blocking this modification protects mice from necroptotic tissue damage in I/R injury and IAV infection, while the same pathway mediates the adaptive myofiber necroptosis that supports muscle growth following intense exercise—establishing RIPK3-K63 lactylation as a metabolic rheostat that determines whether lactate drives pathological destruction or physiological remodeling.

RESULTS

Lactate dysregulation inhibits necroptosis

Unlike other forms of cell death associated with metabolic dysregulation, such as ferroptosis or cuproptosis, necroptosis is tightly regulated through signaling cascades that lead to RIPK3 kinase activation, ultimately executing membrane-lytic cell death via the membrane-damaging protein MLKL.[1,2,9] The potential impact of metabolic homeostasis on the regulation of the RIPK3-MLKL axis in necroptosis remains an open question, despite the current lack of clarity on how cellular metabolic changes might directly influence this pathway. To explore this, we used necroptosis-sensitive L929 cells to screen a library of 662 compounds that interfere with metabolic homeostasis, with the goal of identifying metabolic perturbations that may modulate necroptosis.

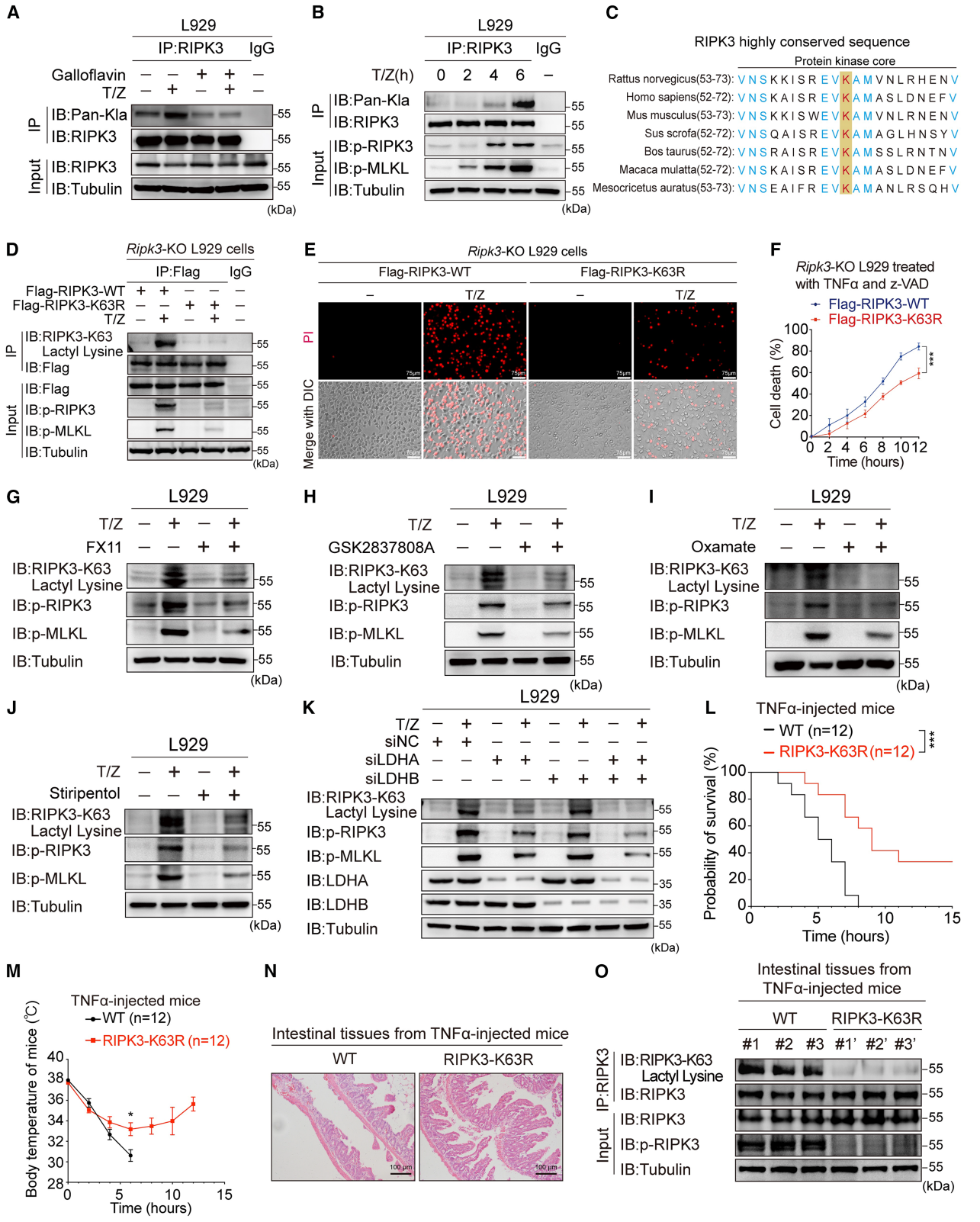
In this screening, L929 cells were treated with TNF-α (T) in combination with the pan-caspase inhibitor z-VAD-FMK (benzyloxycarbonyl-Val-Ala-Asp (OMe)-fluoromethylketone) (Z) to induce necroptosis. Given that the perturbation of metabolic homeostasis is a time-dependent process, the cells were pretreated with metabolic disturbance compounds for 12 h, followed by the addition of T/Z-necroptosis stimuli for an additional 6 h to ensure a sustained disruption of metabolite homeostasis (Figure 1A). To validate our screening approach, we utilized necrostatin-1 (Nec-1), a well-characterized RIPK1 inhibitor,[33] as a positive control for inhibiting necroptosis signaling.

Interestingly, we observed that prolonged inhibition of LDH enzymatic activity by its specific inhibitor, galloflavin, emerged as the most potent inhibitor of necroptosis (Figure 1B). Time course analysis confirmed that galloflavin treatment progressively reduced both intracellular lactate levels and RIPK3 lactylation, with concomitant suppression of p-RIPK3 and p-MLKL signals (Figures S1A and S1B). To assess membrane damage, a key feature of necroptosis, we conducted a membrane-damaging assay using propidium iodide (PI) staining. This assay confirmed that necroptosis was indeed blocked by galloflavin treatment, as evidenced by a reduction in PI staining (Figures 1C and 1D). Furthermore, we examined the levels of phosphorylated RIPK3 (p-RIPK3) and p-MLKL, which are crucial markers of necroptosis activation. Consistent with the results from the PI staining, we observed that both p-RIPK3 and p-MLKL signals were downregulated in cells treated with galloflavin during necroptosis induction (Figure 1E). Galloflavin treatment did not alter intracellular acetyl-coenzyme A (CoA) levels, supporting its specificity toward lactate metabolism (Figures S1C and S1D). Acetyl-CoA levels were measured independently by targeted liquid

(J–M) Pharmacological inhibition of LDH attenuates necroptosis. Time course analysis of cell viability in L929 cells pretreated with DMSO or (J) FX11 (20 μM), (K) GSK2837808A (40 μM), (L) oxamate (10 mM), or (M) stiripentol (250 μM) for 24 h prior to T/Z treatment. Cell viability was assessed by ATP levels.

(N and O) Genetic knockdown of LDHA suppresses necroptosis. (N) L929 cells were transfected with siNC or siLDHA for 48 h and then treated with or without T/Z for 3 h. Cell death was assessed by PI staining. (O) Immunoblot analysis of p-RIPK3 and p-MLKL levels in L929 cells transfected with siNC or siLDHA, followed by treatment with or without T/Z for 6 h. Tubulin was used as a loading control.

Data are presented as mean ± SD; individual data points represent independent experiments. Statistical analysis for (D) and (F)–(N) was performed using two-way ANOVA with Bonferroni's multiple comparisons test. $^{*}p < 0.05$; $^{**}p < 0.01$; $^{***}p < 0.001$. Unless otherwise indicated, $n = 3$ independent experiments. All experiments were repeated at least three independent times; statistical analysis was conducted on pooled data from all replicates.



(legend on next page)

chromatography-tandem mass spectrometry (LC-MS/MS) (Figure S1C) and a colorimetric assay (Figure S1D), with both approaches producing consistent results.

In addition to TNF-induced necroptosis, this process can also be triggered by other stimuli, such as interferon (IFN)-γ/Z treatment in L929 cells,[34] poly(I:C)/Z treatment in L929 cells, or lipopolysaccharide (LPS)/Z treatment in bone marrow-derived macrophages (BMDMs).[34,35] Using these assays, we found that all of these necroptotic signals were attenuated by the LDH inhibitor galloflavin (Figures 1F–1I).

To further validate the role of LDHA in necroptosis, we tested multiple structurally distinct LDHA inhibitors. FX11 suppressed T/Z-induced necroptosis in L929 cells (Figure 1J) and reduced intracellular lactate accumulation (Figure S1E). Similarly, FX11 inhibited necroptosis induced by LPS + z-VAD in BMDMs and poly(I:C) + z-VAD in L929 cells (Figures S1F and S1G). GSK2837808A, another LDHA inhibitor, also suppressed T/Z-induced necroptosis (Figure 1K) and poly(I:C) + z-VAD-induced necroptosis (Figure S1H). Oxamate similarly attenuated T/Z-induced necroptosis (Figure 1L). Additionally, stiripentol, a clinically used LDH inhibitor, suppressed necroptosis induced by both T/Z and poly(I:C) + z-VAD (Figure 1M; Figure S1I).

Genetic approaches further supported these findings. Small interfering RNA (siRNA)-mediated knockdown of LDHA in L929 cells significantly reduced T/Z-induced necroptosis, as assessed by both ATP-based viability assays and PI staining (Figure 1N; Figure S1J). Immunoblot analysis confirmed that LDHA knockdown attenuated p-RIPK3 and p-MLKL levels during necroptosis induction (Figure 1O). Simultaneous knockdown of both LDHA and LDHB further enhanced protection against necroptosis induced by T/Z or poly(I:C) + z-VAD (Figures S1K and S1L), with efficient knockdown confirmed by immunoblotting (Figure S1M). Notably, combined LDHA/LDHB knockdown significantly reduced intracellular lactate accumulation during necroptosis (Figure S1N), reinforcing the link between lactate production and necroptotic signaling.

Together, our results suggest that disruption of lactate homeostasis can prevent multiple stimuli-induced necroptosis.

RIPK3-K63 lactylation promotes necroptosis

Given that RIPK3 is a key central determinant of necroptosis across various stimuli, we next investigated whether lactate targets RIPK3 to modulate necroptosis. To this end, we used L929 cells to induce necroptosis via T/Z treatment and tested the lactylation of RIPK3. Endogenous RIPK3 was immunoprecipitated using an anti-RIPK3 antibody, and the enriched RIPK3 was subsequently analyzed by immunoblotting with a pan-L-lactyl lysine (pan-Kla) antibody. RIPK3 lactylation was observed upon necroptosis, which was effectively blocked by the LDH inhibitor galloflavin (Figure 2A). Importantly, galloflavin treatment did not affect RIPK3 acetylation, nor did it alter MLKL acetylation or lactylation, indicating that the effect of LDH inhibition is specific to RIPK3 lactylation (Figures S2A–S2C). Additionally, as necroptosis progressed, we noted a time-dependent accumulation of RIPK3 lactylation, which correlated with increased phosphorylation of both RIPK3 and MLKL (Figure 2B).

Further, we utilized mass spectrometry to analyze the lactylation site of RIPK3. Data-dependent acquisition (DDA) LC-MS/MS

Figure 2. RIPK3-K63 lactylation promotes necroptosis

(A) Immunoblot analysis of RIPK3 lactylation using a pan-L-lactyl lysine (pan-Kla) antibody. L929 cells were pretreated with the LDH inhibitor galloflavin (100 μM) for 24 h, followed by treatment with or without T/Z (TNF-α: 50 ng/mL; z-VAD: 20 μM) for 6 h. RIPK3 was immunoprecipitated from whole-cell lysates using an anti-RIPK3 antibody or control immunoglobulin G (IgG) and probed for lactylation.

(B) Time course analysis of RIPK3 lactylation during necroptosis. L929 cells were treated with T/Z, and RIPK3 was immunoprecipitated at 0, 2, 4, and 6 h. Necroptosis markers (p-RIPK3 and p-MLKL) were detected in whole-cell lysates by immunoblotting.

(C) Sequence alignment of mouse RIPK3-K63 shows conservation of the lysine residue across species, including *Rattus norvegicus*, *Homo sapiens*, *Mus musculus*, *Sus scrofa*, *Bos taurus*, *Macaca mulatta*, and *Mesocricetus auratus*.

(D) Validation of RIPK3-K63 lactylation using a custom-made anti-lactylated RIPK3-K63 antibody. *Ripk3*-knockout L929 cells were transfected with FLAG-RIPK3-WT or FLAG-RIPK3-K63R constructs, followed by treatment with or without T/Z for 6 h. RIPK3 was enriched using anti-FLAG beads and immunoblotted for lactylation. Levels of p-RIPK3 and p-MLKL were also assessed in whole-cell lysates. Tubulin was used as a loading control.

(E) Representative fluorescence images of PI staining in *Ripk3*-knockout L929 cells expressing FLAG-RIPK3-WT or FLAG-RIPK3-K63R treated with T/Z for 3 h. Scale bar: 75 μm.

(F) R*ipk3*-knockout L929 cells reconstituted with FLAG-RIPK3-WT or FLAG-RIPK3-K63R were treated with T/Z for the indicated time. Cell viability was assessed by ATP levels.

(G–J) Inhibition of LDH reduces RIPK3-K63 lactylation. L929 cells were treated with T/Z for 6 h in the presence or absence of: (G) FX11 (20 μM, 24 h); (H) GSK2837808A (40 μM, 24 h); (I) oxamate (10 mM, 24 h); or (J) stiripentol (250 μM, 24 h). Immunoblot analysis was performed to detect RIPK3-K63 lactylation, p-RIPK3, and p-MLKL. Tubulin was used as a loading control.

(K) L929 cells were transfected with siNC, siLDHA, siLDHB, or siLDHA plus siLDHB, followed by treatment with or without T/Z (6 h). Immunoblotting was performed to detect RIPK3-K63 lactylation, p-RIPK3, p-MLKL, LDHA, and LDHB. Tubulin was used as a loading control.

(L) Kaplan-Meier survival analysis showing that K63R mutation protects mice from TNF-α-induced SIRS. Wild-type (WT) mice or RIPK3-K63R mutant mice were injected intravenously with TNF-α (430 ng/kg), and survival was monitored over time (n = 12 mice per group).

(M) RIPK3-K63R mutant mice were protected from TNF-α-induced hypothermia. Body temperature was measured at the indicated intervals after TNF-α injection (n = 12 mice per group at baseline; the number of surviving mice decreased over time due to mortality). Statistical comparison was performed at 6 h post-injection, with n = 5 WT and n = 10 RIPK3-K63R mice remaining at this time point.

(N) Representative H&E staining of intestinal tissue sections from WT and RIPK3-K63R mice following TNF-α injection. Scale bar: 100 μm.

(O) Immunoblot analysis of RIPK3-K63 lactylation in intestinal tissue after TNF-α-induced SIRS. Intestinal lysates from three individual mice per group were subjected to the same analysis as described in (D).

Data are presented as mean ± SD; individual data points represent independent experiments (F) or individual mice (M). Statistical analysis for (F) was performed using two-way ANOVA with Bonferroni's multiple comparisons test; (L) was analyzed using the log-rank (Mantel-Cox) test; and (M) was analyzed using an unpaired two-tailed t test with Welch's correction. $^{*}p < 0.05$; $^{***}p < 0.001$. *In vitro* experiments were repeated at least three independent times; statistical analysis was conducted on pooled data from all replicates.

analysis of nuclear-enriched RIPK3 immunoprecipitates from T/Z-treated L929 cells identified the K63 residue as the lactylation site (Figure S3A). Targeted LC-MS/MS further confirmed this modification within the modified peptide sequence ISWEV(Kla)AMVNLR (Figure S3B). Sequence alignment revealed that this site is conserved across species, including *Rattus norvegicus*, *Homo sapiens*, *Mus musculus*, *Sus scrofa*, *Bos taurus*, *Macaca mulatta*, and *Mesocricetus auratus* (Figure 2C). Based on this finding, we developed a polyclonal antibody specifically to recognize lactylated RIPK3 at K63. Additionally, we generated a FLAG-tagged K63R mutant of RIPK3 and transiently transfected it into *Ripk3*-knockout L929 cells as a negative control to validate RIPK3 K63 lactylation during necroptosis. Upon induction of necroptosis by T/Z treatment, we detected RIPK3 and MLKL phosphorylation, as well as RIPK3-K63 lactylation, in wild-type (WT) RIPK3-expressing cells. In contrast, FLAG-tagged K63R mutant RIPK3 showed no lactylation and significantly reduced RIPK3/MLKL phosphorylation after T/Z treatment (Figure 2D). Notably, the K63R mutation abolished T/Z-induced RIPK3 lactylation while leaving RIPK3 acetylation unaffected, confirming the specificity of K63 as the lactylation site (Figure S2D).

Consistently, cell death was significantly protected in *Ripk3* knockout L929 cells reconstituted with the RIPK3-K63R mutant (Figures 2E and 2F). Incucyte live-cell imaging further confirmed that the K63R mutation conferred resistance to necroptosis, mimicking the protective effect of galloflavin treatment (Figure S2E). To determine whether the protective effect of LDH inhibition depends on RIPK3-K63, we performed siRNA-mediated knockdown of LDHA and LDHB in Ripk3-knockout L929 cells reconstituted with either WT-RIPK3 or RIPK3-K63R. Combined knockdown of LDHA and LDHB significantly protected WT-reconstituted cells from necroptosis but failed to further protect K63R-reconstituted cells, indicating that the anti-necroptotic effect of LDH inhibition is mediated through RIPK3-K63 lactylation (Figures S2F and S2G).

We further validated these findings using multiple LDHA inhibitors. Treatment with FX11, GSK2837808A, oxamate, or stiripentol each reduced RIPK3-K63 lactylation along with p-RIPK3 and p-MLKL levels during T/Z-induced necroptosis (Figures 2G–2J). Similarly, siRNA-mediated knockdown of LDHA, LDHB, or both resulted in decreased RIPK3-K63 lactylation and attenuated necroptosis signaling (Figure 2K).

This finding was further confirmed in human HEK293T cells, where expression of the K62R mutant of human RIPK3 (corresponding to mouse K63) also blocked T/S/Z-induced necroptosis, as assessed by PI staining and ATP-based viability assays (Figures S2H–S2J). Additionally, we generated K63R mutant knockin (KI) mice (Figure S2K), and primary mouse embryonic fibroblast (MEF) cells isolated from these mice displayed resistance to necroptosis induced by T/C/Z (Figure S2L). BMDMs from K63R KI mice were also protected from necroptosis induced by LPS + z-VAD or poly(I:C) + z-VAD (Figures S2M and S2N). In these K63R KI primary MEF cells, RIPK3-K63 lactylation was undetectable (Figure S2O).

Furthermore, in a TNF-induced SIRS model of multi-organ damage, K63R KI mice exhibited significantly improved survival rates and better preservation of body temperature compared with WT mice (Figures 2L and 2M). Intestinal damage was also markedly reduced in the K63R KI mice, as shown by H&E staining and quantification of intestinal pathology injury scores (Figure 2N; Figure S2P). Immunoblot analysis revealed that K63 lactylation was absent in the isolated intestine of these mice (Figure 2O).

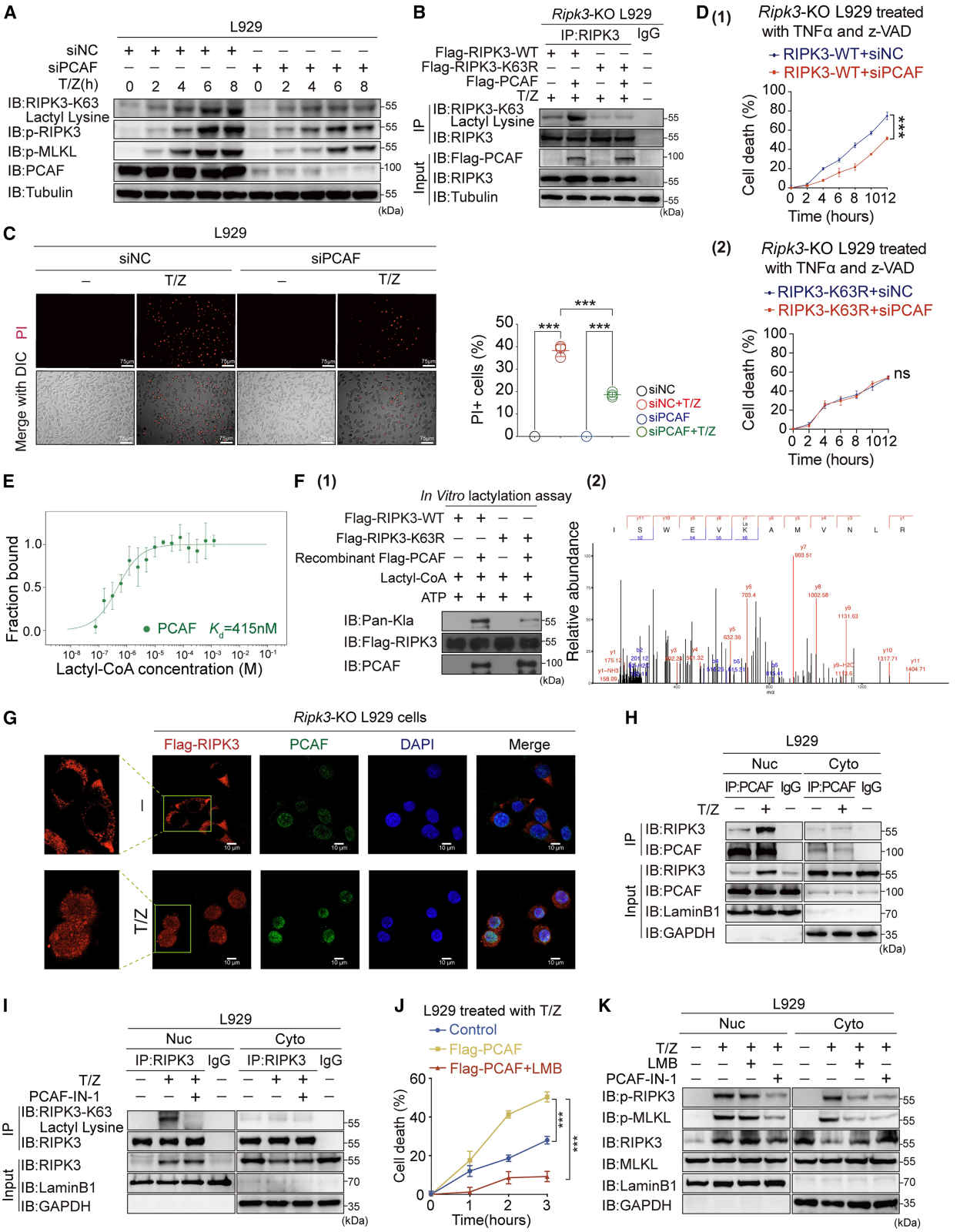
Together, these data demonstrate that lactylation of RIPK3 at K63 (or K62 in human RIPK3) occurs following necroptosis induction and serves as an upstream signal for RIPK3 or MLKL activation (phosphorylation). Loss of this lactylation provides protection against necroptosis induced by multiple stimuli, both in cell culture and *in vivo*.

PCAF functions as the lactyltransferase for RIPK3-K63 in the nucleus

Ever since protein lactylation (Kla) has newly been identified as an emerging post-translational modification in 2019 and 2020,[36,37] only limited number of lactyltransferases have been reported in mammalian cells. Given the chemical similarities between lactylation and acetylation, involving the addition of acyl groups to lysine residues on target proteins, the traditionally categorized acetyltransferases were recently identified lactyltransferases.[36,38–42] Based on this rationale, we hypothesized that enzymes traditionally classified as acetyltransferases may also exhibit lactyltransferase activity catalyzing the lactylation on RIPK3-K63.

To test this hypothesis, we screened a panel of acetyltransferases, including PCAF, p300, CBP, GCN5, and AARS1 for their potential to catalyze RIPK3 lactylation at K63. Using a co-transfection approach with RIPK3, we assessed lactylation signals on RIPK3-K63 with the pan-Kla antibody. Strikingly, only PCAF co-immunoprecipitated with RIPK3 and its overexpression significantly enhanced RIPK3-K63 lactylation, as shown in Figure S4A. To extend this screening, we tested additional candidate enzymes in HEK293T cells, including GCN5, AARS2, MOF, TIP60, GTF3C4, HBO1, HAT1, and NAA60. Among all candidates tested, only PCAF robustly promoted RIPK3 lactylation (Figure S4A). In L929 cells, knockdown of PCAF expression significantly reduced RIPK3-K63 lactylation during necroptosis (Figure 3A). WT RIPK3 lactylation was markedly increased by overexpressing PCAF but not RIPK3-K63R mutant (Figure 3B). Knocking down PCAF expression inhibited necroptotic cell death, as evidenced by reduced PI staining (Figure 3C). Time course analysis further confirmed that PCAF knockdown protected *Ripk3*-knockout L929 cells reconstituted with WT-RIPK3 from necroptosis, whereas cells reconstituted with RIPK3-K63R were already resistant and showed no additional protection upon PCAF knockdown (Figure 3D). Importantly, PCAF knockdown did not affect the acetylation of either RIPK3 or MLKL, indicating that PCAF specifically regulates RIPK3 lactylation rather than acetylation during necroptosis (Figure S4C). Consistently, PCAF inhibitor PCAF-IN-1 effectively blocked necroptotic cell death in L929 cells (Figure S4B) and suppressed RIPK3-K63 lactylation (Figure S4D) as well as RIPK3/MLKL phosphorylation (Figure S4E) upon necroptosis induction. Another PCAF inhibitor, CPTH2, similarly reduced RIPK3-K63 lactylation and attenuated p-RIPK3 and p-MLKL levels in a time-dependent manner (Figure S4F) and dose-dependently protected L929 cells from T/Z-induced necroptosis (Figure S4G).

To rule out contributions from other acetyltransferases, we systematically knocked down HBO1, TIP60, HAT1, AARS2,



(legend on next page)

GTF3C4, and NAA60 in L929 cells. None of these knockdowns significantly affected T/Z-induced necroptosis (Figures S5A–S5F). Although knockdown of MOF or GCN5 partially attenuated necroptosis, neither affected RIPK3 lactylation, indicating that their effects on necroptosis are independent of RIPK3-K63 lactylation (Figures S5G–S5J).

These findings demonstrate that PCAF is essential for the lactylation of RIPK3-K63, which in turn promotes necroptosis, and highlights its potential role in linking metabolic regulation to post-translational modifications in necroptosis pathways.

Next, we investigated whether PCAF directly functions as a lactyltransferase for RIPK3-K63 lactylation. PCAF was traditionally recognized as an acetyl-CoA transferase.[43,44] Lactylation modification is an actively enzymatic post-translational process reliant on lactoyl CoA (lactyl-CoA) as a substrate.[45] Based on these, we hypothesized that PCAF might also utilize lactyl-CoA as a cofactor for lactylation reaction. To test this, we used purified recombinant PCAF (Figure S4H) and evaluated its interaction with lactyl-CoA through microscale thermophoresis (MST) analysis. By mixing purified PCAF with serial dilutions of lactyl-CoA at room temperature, we determined a dissociation constant (K_d) of approximately 415 nM, confirming direct binding of lactyl-CoA to PCAF (Figure 3E). An *in vitro* lactylation assay demonstrated that recombinant PCAF could catalyze the lactylation of WT-RIPK3, but not RIPK3-K63R, in the presence of lactyl-CoA and ATP. LC-MS/MS analysis of the reaction product confirmed the presence of the lactylated peptide ISWEV(Kla)AMVNLR, providing direct evidence that PCAF acts as the lactyltransferase for RIPK3 at K63 (Figure 3F).

Given that PCAF predominantly exerts its enzymatic function in the nucleus,[46,47] we hypothesized that PCAF might mediate RIPK3 lactylation within the nucleus to regulate necroptosis. To investigate this, we performed co-immunofluorescence staining and observed nuclear colocalization of PCAF with RIPK3 following necroptosis induction (Figure 3G). Co-immunoprecipitation analysis further confirmed that the interaction between PCAF and RIPK3 primarily occurred in the nucleus under necroptosis conditions (Figure 3H).

Based on the above findings, we proposed that RIPK3 undergoes lactylation by PCAF in the nucleus, after which it is exported to the cytoplasm to promote necroptosis. To test this hypothesis, we pretreated L929 cells with the PCAF inhibitor PCAF-IN-1 and performed nuclear/cytoplasmic fractionation. PCAF inhibition blocked the accumulation of lactylated RIPK3 in the nucleus (Figure 3I). Consistent with this, LDH inhibitors galloflavin and FX11 also reduced global protein lactylation in the nucleus (Figures S4I and S4J), and combined knockdown of LDHA and LDHB similarly decreased nuclear lactylation levels (Figure S4K).

PCAF overexpression enhanced necroptosis, an effect that was prevented by leptomycin B (LMB), a nuclear export inhibitor that blocks RIPK3 nuclear export (Figure 3J). Immunoblot analysis of cytoplasmic and nuclear fractions showed that PCAF inhibition suppressed the phosphorylation of RIPK3 and MLKL in the nucleus, whereas LMB inhibited p-RIPK3/MLKL cytoplasmic translocation from the nucleus (Figure 3K). Similar results were obtained using selinexor, another nuclear export inhibitor, which reversed PCAF-mediated enhancement of

Figure 3. PCAF functions as the lactyltransferase for RIPK3-K63 in the nucleus

(A) L929 cells were transfected with non-targeting control (siNC) or PCAF-targeting (siPCAF) siRNA, followed by treatment with or without T/Z (TNF-α: 50 ng/mL; z-VAD: 20 μM) for the indicated times (0, 2, 4, 6, or 8 h). RIPK3-K63 lactylation, p-RIPK3, p-MLKL, PCAF expression, and tubulin were detected by immunoblotting.

(B) RIPK3-K63R mutation abolished lactylation mediated by PCAF overexpression. *Ripk3*-knockout L929 cells were co-transfected with FLAG-PCAF and either FLAG-RIPK3-WT or FLAG-RIPK3-K63R plasmids, followed by treatment with or without T/Z for 6 h, and RIPK3 lactylation analysis.

(C) PCAF knockdown suppresses T/Z-induced necroptosis. L929 cells were transfected with siNC or siPCAF, followed by treatment with or without T/Z for 3 h. Left: representative fluorescence images of PI staining showing necroptotic cell death. Scale bar: 75 μm. Right: quantification of PI-positive cells.

(D) PCAF promotes necroptosis via RIPK3-K63. Time course analysis of cell death in *Ripk3*-knockout L929 cells reconstituted with FLAG-RIPK3-WT (1) or FLAG-RIPK3-K63R (2). Cells were transfected with non-targeting (siNC) or PCAF-targeting (siPCAF) siRNAs for 48 h, followed by T/Z treatment. PCAF knockdown protected WT-reconstituted cells from necroptosis, an effect that was lost in K63R-reconstituted cells.

(E) Microscale thermophoresis (MST) analysis showing the direct binding affinity between recombinant PCAF and lactyl-CoA (K_d = 415 nM)

(F) *In vitro* lactylation assay demonstrating PCAF-mediated lactylation of RIPK3 at K63. (1) FLAG-RIPK3-WT or FLAG-RIPK3-K63R was expressed and immunoprecipitated from HEK293T cells, then incubated with recombinant FLAG-PCAF in the presence of lactyl-CoA and ATP. RIPK3 lactylation was detected by immunoblotting with a pan-Kla antibody. FLAG-RIPK3 levels are shown as controls. (2) LC-MS/MS analysis identified the lactylated RIPK3 peptide ISWEV(Kla)AMVNLR, confirming lactylation at K63. The analyzed sample was an independent *in vitro* reaction in which purified His-tagged RIPK3 kinase domain was incubated with recombinant FLAG-PCAF in the presence of lactyl-CoA and ATP.

(G) Nuclear colocalization of RIPK3 and PCAF. Immunofluorescence of FLAG-RIPK3 (red) and endogenous PCAF (green) in necroptotic L929 cells treated with T/Z. Nuclei were counterstained with DAPI. Enlarged views of the boxed areas showing nuclear localization of RIPK3 under T/Z treatment are shown. Scale bar: 10 μm.

(H) Interaction of PCAF and RIPK3 in the nucleus analyzed by cytoplasmic and nuclear fractionation followed by immunoprecipitation with an anti-PCAF antibody or control IgG. Lamin B1 and glyceraldehyde-3-phosphate dehydrogenase (GAPDH) served as nuclear and cytoplasmic markers, respectively.

(I) The PCAF inhibitor PCAF-IN-1 blocked RIPK3-K63 lactylation in the nucleus. L929 cells were pretreated with PCAF-IN-1 (10 μM, 72 h), followed by treatment with or without T/Z for 6 h, and RIPK3 lactylation analysis in nuclear and cytoplasmic fractions.

(J) Overexpression of PCAF promoted T/Z-induced necroptosis, an effect reversed by LMB. L929 cells were transfected with FLAG-vector or FLAG-PCAF, with or without the nuclear export inhibitor leptomycin B (LMB, 1 μM). Cell viability was assessed by ATP levels.

(K) Blocking RIPK3 nuclear export reduced RIPK3 and MLKL phosphorylation, similar to PCAF inhibition. Immunoblot analysis of p-RIPK3, p-MLKL, and RIPK3/MLKL expression in cytoplasmic and nuclear fractions following treatment with T/Z in the presence or absence of LMB (1 μM) or PCAF-IN-1 (10 μM). Lamin B1 and GAPDH served as nuclear and cytoplasmic markers, respectively.

Data are presented as mean ± SD; individual data points represent independent experiments. Statistical analysis for (C), (D), and (J) was performed using two-way ANOVA with Bonferroni's multiple comparisons test. *ns*, not significant; ***$p < 0.001$. Unless otherwise indicated, $n = 3$ independent experiments. All experiments were repeated at least three independent times; statistical analysis was conducted on pooled data from all replicates.

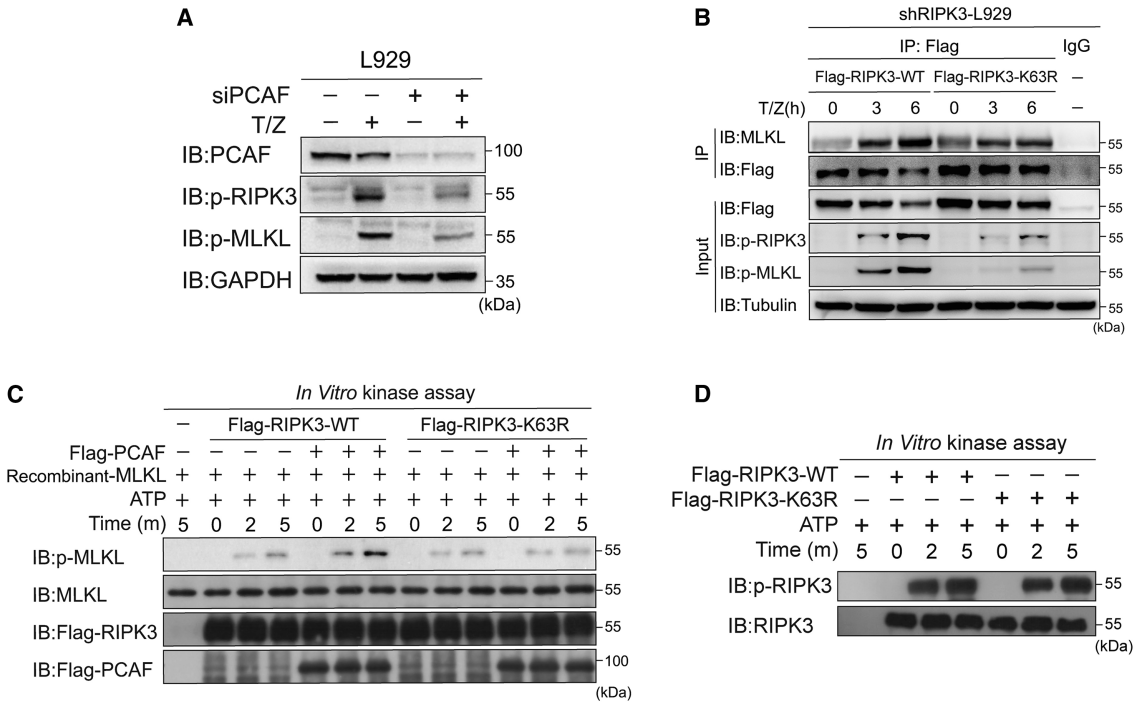


Figure 4. RIPK3-K63 lactylation promotes its kinase activity

(A) Knockdown of PCAF attenuates RIPK3 and MLKL phosphorylation. L929 cells were transfected with siNC or siPCAF and treated with or without T/Z (TNF-α: 50 ng/mL; z-VAD: 20 μM) for 6 h. p-RIPK3 and p-MLKL were detected by immunoblotting. GAPDH was used as a loading control.

(B) The RIPK3-K63R mutation disrupts the RIPK3-MLKL interaction. *Ripk3*-knockdown L929 cells (shRIPK3-L929) were reconstituted with FLAG-RIPK3-WT or FLAG-RIPK3-K63R. At 24 h post-transfection, cells were treated with T/Z for 0, 3, or 6 h. Whole-cell lysates were subjected to immunoprecipitation using an anti-FLAG antibody or control IgG, and the interaction with MLKL was analyzed by immunoblotting.

(C) *In vitro* kinase assay to evaluate p-MLKL levels mediated by RIPK3 with or without PCAF-mediated lactylation. FLAG-RIPK3-WT or FLAG-RIPK3-K63R was expressed and immunoprecipitated from HEK293T cells, then incubated with recombinant MLKL (residues 181–464), and ATP in the presence or absence of FLAG-PCAF for the indicated times (0, 2, and 5 min). MLKL phosphorylation levels were assessed by immunoblotting.

(D) *In vitro* kinase assay showing that the K63R mutation did not apparently alter the basal kinase activity of RIPK3. FLAG-RIPK3-WT or FLAG-RIPK3-K63R was expressed and immunoprecipitated from HEK293T cells, then incubated with ATP for the indicated time (0, 2, and 5 min), and autophosphorylation was detected by immunoblotting with anti-p-RIPK3 antibody.

All experiments were repeated at least three independent times.

necroptosis (Figure S4L) and blocked cytoplasmic accumulation of p-RIPK3 and p-MLKL (Figure S4M).

To further confirm that nuclear RIPK3 lactylation is required for necroptosis, we reconstituted *Ripk3*-knockout L929 cells with either WT-RIPK3 or nuclear-localized nuclear localization signal (NLS)-RIPK3. Cells expressing NLS-RIPK3 showed enhanced sensitivity to T/Z-induced necroptosis, which was reversed by CPTH2 treatment (Figure S4N). Fractionation analysis confirmed that NLS-RIPK3 accumulated in the nucleus and exhibited elevated RIPK3-K63 lactylation, which was blocked by CPTH2 (Figure S4O).

Taken together, these results suggest that PCAF acts as a nuclear lactyltransferase, catalyzing RIPK3-K63 lactylation within the nucleus. This modification subsequently enhances RIPK3-MLKL axis-mediated necroptosis signaling.

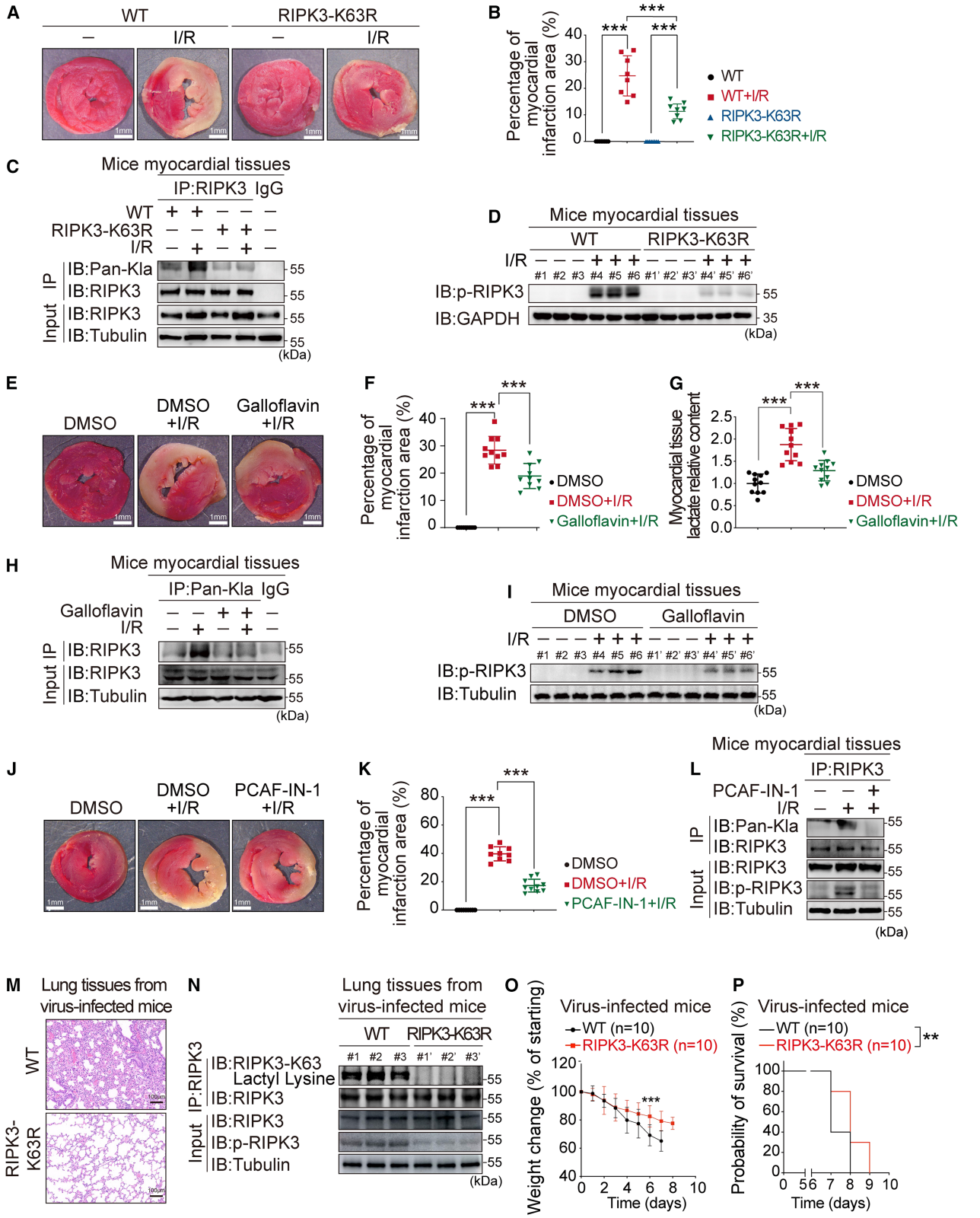
RIPK3-K63 lactylation promotes its kinase activity

After identifying PCAF as the lactyltransferase responsible for RIPK3-K63 lactylation, we next sought to understand the molecular mechanism by which this modification enhances necroptosis signaling.

First, knockdown of PCAF significantly reduced the phosphorylation of both RIPK3 and MLKL (Figure 4A). These data together imply that K63 lactylation contributes to the increased kinase activity of RIPK3.

Since RIPK3 auto-phosphorylation (on Ser227 of human RIPK3; on Ser232 of mouse RIPK3) is a prerequisite for its substrate MLKL recruitment,[11] next, we examined how RIPK3-K63 lactylation affects RIPK3-MLKL complex assembly. *Ripk3*-knockdown L929 cells (shRIPK3-L929) were reconstituted with FLAG-RIPK3-WT or FLAG-RIPK3-K63R, treated with T/Z for 0, 3, or 6 h, and subjected to co-immunoprecipitation analysis. This revealed that without K63 lactylation—achieved by expressing the RIPK3-K63R mutant—the RIPK3-MLKL interaction was substantially disrupted (Figure 4B). This suggests that RIPK3-K63 lactylation enhances the recruitment of MLKL.

Importantly, *in vitro* kinase assays demonstrated that in the presence of PCAF, WT-RIPK3 exhibited enhanced phosphorylation of recombinant MLKL (residues 181–464). In contrast, this phosphorylation was markedly weaker in the absence of PCAF. Notably, PCAF did not promote the K63R mutant RIPK3-catalyzed phosphorylation of MLKL (Figure 4C).



(legend on next page)

To determine whether the K63R mutation itself affects the intrinsic kinase activity of RIPK3, we performed an *in vitro* autophosphorylation assay. FLAG-RIPK3-WT or FLAG-RIPK3-K63R was expressed and immunoprecipitated from HEK293T cells, then incubated with ATP for the indicated times (0, 2, and 5 min). Autophosphorylation was detected by immunoblotting with an anti-p-RIPK3 antibody. The results showed that the K63R mutation did not affect the basal autophosphorylation kinetics of RIPK3 (Figure 4D), indicating that the reduced necroptosis signaling observed with RIPK3-K63R is due to the loss of lactylation rather than an intrinsic defect in kinase activity.

Together, these results indicate that RIPK3-K63 lactylation enhances its kinase activity, which promotes RIPK3 autophosphorylation and stabilizes its interaction with MLKL, thereby promoting MLKL phosphorylation and amplifying necroptosis signaling.

Inhibiting RIPK3-K63 lactylation reduces necroptosis-driven damage in myocardial and lung injury

Necroptosis is a key contributor to tissue damage during ischemia-reperfusion (I/R) injury and IAV infection. Elevated lactate levels in these pathological conditions have been shown to amplify inflammation.[48–50] However, the underlying mechanisms, particularly the role of lactate accumulation for necroptosis-mediated tissue damage, remain unclear. We hypothesize that RIPK3-K63 lactylation promotes necroptosis-mediated tissue damage in these scenarios.

Using a cardiac I/R injury model, we compared WT mice with RIPK3-K63R mutant mice. Remarkably, K63R mutant mice showed significant protection against myocardial damage (representative images, Figure 5A; quantitative analysis, Figure 5B). RIPK3-K63 lactylation was detected in WT myocardial tissue following I/R injury, whereas this modification was absent in K63R mutant mice (Figure 5C). Similarly, RIPK3 activation, indicated by phosphorylation, was robust in WT mice but markedly reduced in K63R mutant mice (Figure 5D).

To further explore the role of lactylation, we treated WT mice with the LDH inhibitor galloflavin. This treatment reduced I/R-induced myocardial damage (Figures 5E and 5F), lowered myocardial lactate levels (Figure 5G), and blocked RIPK3 lactylation and phosphorylation (Figures 5H and 5I). These results were corroborated in myocardial-specific LDHA knockout mice (*Myh6-Cre*+; *Ldha*$^{flox/flox}$), which also exhibited reduced RIPK3 lactylation, phosphorylation, and weaker tissue damage after I/R injury (Figures S6A–S6E). Consistently, PCAF inhibitor PCAF-IN-1 provided similar protection to mice from myocardial damage by reducing RIPK3 lactylation and subsequent phosphorylation (Figures 5J–5L).

Figure 5. Inhibition of RIPK3-K63 lactylation mitigates necroptosis-driven damage in myocardial ischemia/reperfusion and lung injury

(A–D) The RIPK3-K63R mutation attenuates necroptosis-driven damage in myocardial ischemia/reperfusion (I/R).

(A) Representative 2,3,5-triphenyltetrazolium chloride (TTC) staining of myocardial infarct areas in hearts from wild-type (WT) and RIPK3-K63R mice with or without I/R injury (45 min ischemia/4 h reperfusion). Hearts were harvested immediately following reperfusion, frozen at −80°C for 10 min, sectioned into 1–2 mm slices, and incubated in 2% TTC at 37°C for 20 min. Scale bar: 1 mm.

(B) Quantification of infarct size in hearts from WT and RIPK3-K63R mice with or without I/R injury. n = 8 mice per group.

(C) RIPK3 lactylation in myocardial tissue from WT and RIPK3-K63R mice with or without I/R injury. Whole heart lysates were immunoprecipitated using an anti-RIPK3 antibody or control IgG, followed by immunoblotting with an anti-pan-Kla antibody.

(D) Immunoblot analysis of p-RIPK3 expression in myocardial tissue from WT and RIPK3-K63R mice with or without I/R injury. Lysates from three mice per condition were analyzed, with GAPDH as the loading control.

(E–I) The effect of the LDH inhibitor galloflavin on necroptosis-driven damage in myocardial I/R.

(E) Representative TTC staining of infarct areas in hearts from WT mice treated with DMSO or galloflavin (50 mg/kg/day, intraperitoneal [i.p.]) for 3 days with or without subsequent I/R injury (45 min ischemia/4 h reperfusion). Scale bar: 1 mm.

(F) Quantification of infarct size in hearts from WT mice treated with DMSO or galloflavin with or without I/R injury. n = 10 mice per group.

(G) Relative lactate content in myocardial tissue from WT mice treated with DMSO or galloflavin with or without I/R injury, normalized to the DMSO group without I/R. n = 11 mice per group.

(H) The effect of galloflavin on RIPK3 lactylation in myocardial tissue. Whole heart lysates were immunoprecipitated using an anti-pan-Kla antibody or control IgG, followed by immunoblotting with an anti-RIPK3 antibody.

(I) Immunoblot analysis of p-RIPK3 levels in myocardial tissue. Lysates from three mice per condition were analyzed. Tubulin served as the loading control.

(J–L) The effect of the PCAF inhibitor PCAF-IN-1 on necroptosis-driven damage in myocardial I/R.

(J) Representative TTC staining of infarct areas in hearts from WT mice treated with DMSO or PCAF-IN-1 (0.25 mg/kg/day, i.p.) for 3 days with or without subsequent I/R injury (45 min ischemia/4 h reperfusion). Scale bar: 1 mm.

(K) Quantification of myocardial infarct size in WT mice from three groups: DMSO-treated sham controls (n = 10), DMSO-treated mice subjected to I/R injury (n = 9), and PCAF-IN-1-treated mice subjected to I/R injury (n = 10).

(L) The effect of PCAF-IN-1 on RIPK3 lactylation in myocardial tissue. Whole heart lysates were immunoprecipitated using an anti-RIPK3 antibody or control IgG, followed by immunoblotting with an anti-pan-Kla antibody.

(M–P) RIPK3-K63 lactylation promotes IAV-induced necroptosis-mediated lung injury.

(M) Representative H&E staining of lung tissue from WT and RIPK3-K63R mice intranasally infected with H5N1 virus (median lethal dose [LD_{50}] = $10^{-7.0}$, 50 μL/animal; n = 3 mice per group). Lung tissues were collected on day 7 post-infection, fixed in 4% paraformaldehyde at 4°C for 48 h, paraffin-embedded, and stained with H&E. Scale bar: 100 μm.

(N) RIPK3 lactylation in lung tissue from H5N1-infected WT and RIPK3-K63R mice. Whole lung tissue lysates were immunoprecipitated using an anti-RIPK3 antibody, followed by immunoblotting using the indicated antibodies.

(O) Body weight changes (expressed as percentage of starting body weight) in WT and RIPK3-K63R mice following H5N1 infection. n = 10 mice per group on day 0.

(P) Kaplan-Meier survival curve showing that the RIPK3-K63R mutation confers protection against H5N1-induced lethality (n = 10 mice per group).

Data are presented as mean ± SD; individual data points represent individual mice. Statistical analysis for (B) was performed using two-way ANOVA with Bonferroni's multiple comparisons test; (F), (G), and (K) were analyzed using one-way ANOVA with Bonferroni's multiple comparisons test; (O) was analyzed at day 6 using an unpaired two-tailed t test with Welch's correction; (P) was analyzed using the log-rank (Mantel-Cox) test. $^{**}p < 0.01$; $^{***}p < 0.001$.

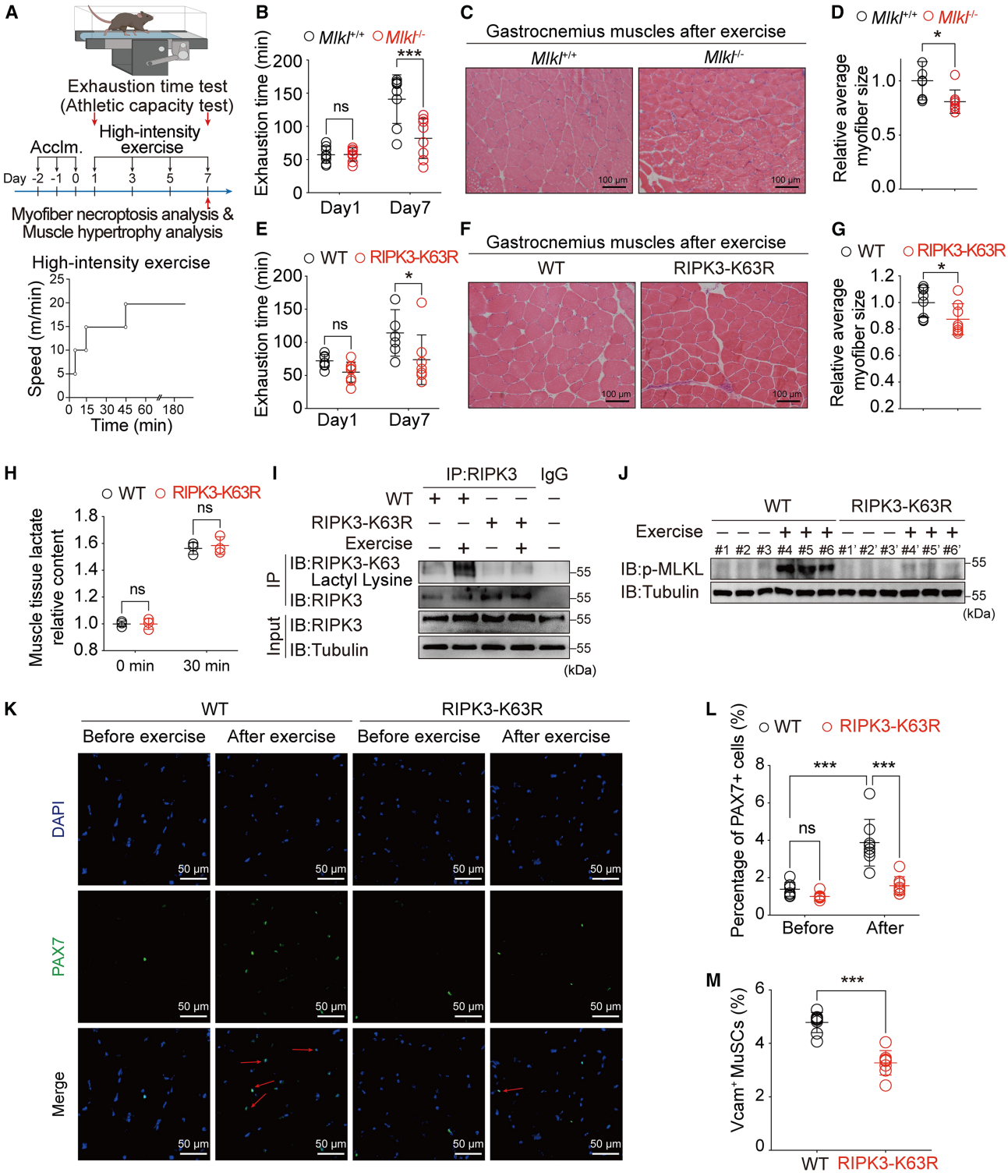


Figure 6. RIPK3-K63 lactylation enhances myofiber necroptosis-induced MuSC activation during high-intensity exercise

(A) Schematic of high-intensity exercise training. Mice (8–10 weeks old) were acclimated to a motorized treadmill for 3 days before being subjected to high-intensity exercise. Mice ran until exhaustion every other day, with the treadmill equipped with an audible stimulus and an electric shock grid at the rear. The exercise protocol included a 5-min warm-up at 5 m/min on a 0° incline, followed by gradual speed increases: 10 m/min for 10 min, 15 m/min for 30 min, and a final increase to 20 m/min until exhaustion. The time to exhaustion was used to assess running endurance, which was measured on days 1 and 7 to evaluate exercise-induced muscle adaptation.

(B–D) The role of MLKL-dependent necroptosis in exercise-induced muscle adaptation.

(legend continued on next page)

We next assessed whether RIPK3-K63 lactylation influences necroptosis-mediated tissue damage during H5N1 influenza virus infection. Strikingly, RIPK3-K63R mutant mice displayed significant protection against lung tissue damage after IAV infection (Figure 5M). In these mice, RIPK3-K63 lactylation was abolished, and phosphorylation of RIPK3 was substantially reduced (Figure 5N). Furthermore, RIPK3-K63R mutant mice experienced less weight loss and exhibited a higher survival rate compared with WT mice following IAV infection (Figures 5O and 5P).

Since RIPK3 has been reported to possess MLKL-independent functions, including scaffold-mediated transcriptional regulation of inflammatory genes,[51] we investigated whether RIPK3-K63 lactylation affects these non-cell death roles. To address this, we performed reverse-transcription quantitative PCR (RT-qPCR) analysis on Ripk3-knockout L929 cells reconstituted with FLAG-RIPK3-WT or FLAG-RIPK3-K63R following T/Z treatment. We examined the expression of multiple previously reported RIPK3-dependent genes, including *Il-6*, *Ccl2*, *Cxcl10*, *Ifi47*, *Ifi44*, *Inhba*, *Cxcl1*, *Cxcl2*, *Il-23α*, *Tgtp1*, *Ccr2*, *Cxcl12*, *Il-1β*, *Cxcr3*, and *Gbp4*. Notably, we observed no significant differences in the induction of these transcripts between WT- and K63R-reconstituted cells (Figure S6F). These results indicate that RIPK3-K63 lactylation does not measurably affect RIPK3-dependent transcriptional responses, suggesting that the protective phenotypes observed in K63R mutant mice are primarily attributable to reduced necroptotic cell death rather than alterations in RIPK3-driven inflammatory gene regulation.

Together, these findings suggest that RIPK3-K63 lactylation is a critical driver of necroptosis-mediated tissue damage in both I/R injury and IAV infection. Pharmacological or genetic inhibition of this modification effectively reduces RIPK3 activation and mitigates associated tissue damage, highlighting its potential as a therapeutic target.

RIPK3-K63 lactylation enhances myofiber necroptosis-induced MuSC activation during high-intensity exercise

Although excessive necroptosis is primarily associated with pathological conditions such as I/R injury and IAV infection, we next investigated whether RIPK3-K63 lactylation also plays a role in physiological contexts where necroptosis occurs at moderate levels and is involved in tissue repair homeostasis. High-intensity exercise is associated with elevated lactate levels, which correlate positively with muscle hypertrophy, though the underlying mechanisms remain unclear. Previous studies have shown that myofiber necroptosis promotes MuSC proliferation after acute injury, aiding muscle repair.[8] Thus, exploring the relationship of RIPK3 lactylation with muscle hypertrophy offers new insight into the beneficial roles of necroptosis in physiological contexts.

To test this, we first evaluated the role of necroptosis in exercise-induced muscle adaptation, with the assay design outlined in Figure 6A. MLKL knockout ($Mlkl^{-/-}$) mice exhibited poorer exercise performance (Figure 6B) and reduced muscle mass (Figures 6C and 6D) compared with their littermates WT ($Mlkl^{+/+}$) mice following high-intensity exercise, indicating that necroptosis contributes to muscle hypertrophy.

RIPK3-K63R mutant mice, which cannot undergo K63 lactylation, displayed phenotypes similar to MLKL-deficient mice. They failed to improve athletic performance (Figure 6E) or increase muscle mass (Figures 6F and 6G) after high-intensity exercise, although both WT and RIPK3-K63R mice exhibited comparable lactate elevations after exercise (Figure 6H). WT mice muscle showed increased RIPK3-K63 lactylation, which was absent in RIPK3-K63R mutants (Figure 6I). Moreover, MLKL phosphorylation—a hallmark of necroptosis activation—was significantly reduced in RIPK3-K63R mutant mice (Figure 6J). These findings demonstrate that RIPK3-K63 lactylation facilitates necroptosis, driving exercise-induced muscle hypertrophy.

Given the established role of myofiber necroptosis in MuSC activation, we examined MuSC markers after high-intensity exercise. Immunofluorescence staining for the MuSC marker PAX7 revealed fewer PAX7+ cells in RIPK3-K63R mice compared with WT mice (Figures 6K and 6L). Fluorescence-activated cell sorting (FACS) analysis further confirmed a reduced number of MuSCs in RIPK3-K63R mutants following exercise (Figure 6M).

(B) Running endurance capacity was measured in $Mlkl^{+/+}$ and $Mlkl^{-/-}$ mice using the exhaustion time as an index of endurance. $n = 8$ per group.
(C) Representative images of H&E-stained gastrocnemius muscle cross-sections from $Mlkl^{+/+}$ and $Mlkl^{-/-}$ mice after the exhaustion test on day 7. Mice underwent high-intensity exercise from days 1 to 7. Scale bar: 100 μm.
(D) Quantification of the average myofiber size from muscle cross-sections of exercised $Mlkl^{+/+}$ and $Mlkl^{-/-}$ mice. $n = 8$ per group.
(E–M) The effect of RIPK3-K63 lactylation on exercise-induced muscle adaptation.
(E) Running endurance of WT and RIPK3-K63R mice was measured on days 1 and 7 by assessing the exhaustion time. $n = 8$ per group.
(F) Representative H&E staining of gastrocnemius muscle cross-sections from WT and RIPK3-K63R mice after the exhaustion test on day 7, following high-intensity exercise from days 1 to 7. Scale bar: 100 μm.
(G) Quantification of the average myofiber size from cross-sectional areas of exercised muscles. $n = 8$ per group.
(H) Relative lactate content in gastrocnemius muscle from WT and RIPK3-K63R mice, measured before and immediately after 30 min of running. Lactate content was normalized to the 0 min value of each genotype. $n = 3$ per group.
(I) Effect of high-intensity exercise on RIPK3-K63 lactylation in gastrocnemius muscle from WT and RIPK3-K63R mice with or without exercise. Immunoprecipitation with anti-RIPK3 antibody or control IgG was followed by immunoblotting for the indicated antibodies.)
(J. Immunoblot analysis of p-MLKL expression in gastrocnemius muscle from WT and RIPK3-K63R mice with or without exercise on day 7. Lysates from three mice per condition were analyzed. Tubulin was used as the loading control.
(K) Immunofluorescence staining of muscle stem cell (MuSC) marker PAX7 (green) in gastrocnemius muscle cross-sections from WT and RIPK3-K63R mice before and after high-intensity exercise (day 7). Nuclei were stained with DAPI. Scale bar: 50 μm.
(L) Quantification of the percentage of $PAX7^+$ cells in gastrocnemius muscle cross-sections before and after high-intensity exercise. $n = 8$ per group.
(M) Flow cytometry (FACS) analysis of MuSCs in gastrocnemius muscle after high-intensity exercise. Quantification of the percentage of MuSCs (SYTOX $Green^-CD11b^-CD31^-CD45^-Sca1^-Vcam^+$) among total digested mononuclear cells. $n = 8$ per group.
Data are presented as mean ± SD; individual data points represent individual mice. p values for (D), (G), and (M) were determined by unpaired two-tailed t test with Welch's correction; p values for (B), (E), (H), and (L) were determined by two-way analysis of variance with Bonferroni's multiple comparisons test. *ns*, not significant; $^*p < 0.05$; $^{***}p < 0.001$.

To further validate the role of lactate metabolism in exercise-induced muscle adaptation, we pharmacologically inhibited LDHA using two structurally distinct inhibitors, galloflavin and GSK2837808A. Mice were administered galloflavin (50 mg/kg) or GSK2837808A (40 mg/kg) via intramuscular injection prior to high-intensity treadmill running. Both inhibitors effectively reduced tissue lactate levels in gastrocnemius muscle following exercise (Figure S7A). Importantly, LDHA inhibition with either galloflavin or GSK2837808A markedly reduced RIPK3 lactylation in muscle tissue (Figures S7B and S7G) and attenuated MLKL phosphorylation (Figures S7C and S7H). Consistent with the phenotypes observed in RIPK3-K63R mutant mice, LDHA inhibitor-treated mice showed a significant reduction in MuSC numbers following exercise, as assessed by flow cytometry (Figures S7D and S7I). Furthermore, both galloflavin- and GSK2837808A-treated mice exhibited smaller myofiber size (Figures S7E and S7J) and impaired running endurance compared with vehicle-treated controls (Figures S7F and S7K). These pharmacological data corroborate our genetic findings and further support the conclusion that LDHA-dependent lactate production and subsequent RIPK3-K63 lactylation are essential for necroptosis-mediated MuSC activation and exercise-induced muscle hypertrophy.

These data indicate that under physiological conditions, RIPK3-K63 lactylation enhances skeletal muscle hypertrophy by driving necroptosis-induced MuSC activation during high-intensity exercise. This process strengthens muscle size and improves exercise performance, highlighting the beneficial role of necroptosis in muscle adaptation.

DISCUSSION

Metabolic regulation of the necroptotic machinery

Programmed cell death is traditionally seen as a tightly regulated biological process, coordinated by specific signaling cascades and executed through defined cell-death effector proteins. These executioners encompass caspase-3/caspase-7 in apoptosis, MLKL in necroptosis, and gasdermins (GSDMs) in pyroptosis.[1,2,52] While cellular metabolic dysregulation has been linked to cell dysfunction and death in processes like ferroptosis, programmed cell death pathways have generally been considered distinct from metabolic regulation.

Our findings reveal that cellular metabolism, particularly lactate homeostasis, is an integral component of necroptosis regulation. We demonstrate that lactate-driven PCAF-mediated lactylation of RIPK3 at K63 is essential for necroptotic signal amplification (graphical abstract), uncovering a previously unappreciated connection between metabolic state and the molecular machinery of programmed cell death.

Lactate, a metabolic byproduct long associated with hypoxia and inflammation, functions here as a signaling molecule with direct regulatory input into necroptotic execution. The lactylation of RIPK3-K63 by PCAF provides a mechanistic explanation for how intracellular lactate is transduced into a cell-death decision, illustrating how metabolic cues can fine-tune programmed cell death pathways. Whether analogous metabolite-driven post-translational modifications regulate other programmed cell death executioners—such as caspases or GSDMs—remains an open question that warrants future investigation.

Nuclear RIPK3 and the role of PCAF-mediated lactylation

The translocation of RIPK3 to the nucleus, alongside its well-documented cytoplasmic localization, has been observed during necroptosis.[32] While nuclear-localized RIPK3 has been implicated in promoting necroptosis, the underlying mechanism has remained unclear. Our findings demonstrate that nuclear RIPK3 is modified by PCAF-mediated lactylation, which enhances its interaction with MLKL and facilitates MLKL phosphorylation. Given that activated PCAF is predominantly enriched in the nucleus,[53,54] these data establish a direct mechanistic link between RIPK3 nuclear translocation and its functional activation during necroptosis.

This nuclear-specific regulatory mechanism clarifies the distinct contribution of RIPK3's subcellular localization to necroptotic signaling and raises new questions about the factors governing RIPK3 nuclear import and export. The observation that lactylated RIPK3 is exclusively retained in the nucleus implies that de-lactylation occurs following nuclear export. Future studies should aim to dissect the molecular machinery governing RIPK3 nucleocytoplasmic trafficking and de-lactylation, which may represent additional regulatory checkpoints in necroptotic control.

PCAF, traditionally recognized as a nuclear acetyltransferase that catalyzes the transfer of acetyl groups to lysine residues,[43,55] had not previously been reported to exhibit lactyltransferase activity. We identify PCAF as the lysine lactyltransferase responsible for RIPK3-K63 lactylation within the nucleus, an activity supported by the structural similarity between acetyl and lactyl groups.[36,42] The identification of PCAF as a lactyltransferase therefore extends the catalog of enzymes capable of mediating this modification beyond p300 and its closest relatives, reinforcing the emerging view that lactylation is a broadly deployed regulatory mechanism executed by multiple members of the acetyltransferase family. This finding expands the functional repertoire of PCAF and broadens the regulatory landscape of lysine post-translational modifications.

Lactate accumulation, necroptosis, and tissue injury

It is well-established that elevated lactate levels are frequently observed in patients with heart failure and are associated with poor outcomes.[56–58] Ischemia activates glycogen breakdown, accelerates glycolysis, and increases lactate production.[59] Lactate accumulation during ischemia has long been associated with cardiac dysfunction and clinical symptoms.[60,61] How lactate accumulation exacerbates acute cardiac damage at the molecular level has, however, remained unclear.

Our data demonstrate that lactate contributes to I/R-induced cardiac damage by promoting RIPK3 lactylation, thereby enhancing RIPK3-mediated necroptosis and driving myocardial injury. These findings provide a molecular explanation for the clinical association between hyperlactataemia and poor cardiac outcomes. Preclinical evidence presented here suggests that targeting lactate metabolism through LDH inhibition or disrupting RIPK3 lactylation through PCAF inhibition may reduce necroptosis-driven myocardial damage. These represent hypotheses to be tested in future studies; important caveats include the limited selectivity of available LDH and PCAF inhibitors and the

potential for systemic metabolic or transcriptional effects that would need to be carefully evaluated before clinical translation.

Similarly, IAV infection induces lactate accumulation,[62] and reducing lactate levels has been shown to have antiviral effect.[63] Elevated lactate levels correlate with the severity of IAV infection-induced lung damage.[50,62,64] Our data demonstrate that IAV-induced lactate accumulation promotes necroptosis-mediated lung injury. Targeting this axis—either through LDH inhibition or PCAF inhibition—may therefore also reduce IAV-associated pulmonary pathology, though the same considerations regarding inhibitor selectivity and off-target effects apply.

It is also worth noting that galloflavin has been reported to exert protective effects in other disease contexts through distinct mechanisms—for example, suppressing the pyruvate dehydrogenase complex (PDHC) and reducing histone acetylation in acute liver failure.[65] Together, these findings suggest that galloflavin may act through multiple metabolic pathways in a context-dependent manner. Our study identifies RIPK3 lactylation as an additional mechanism by which galloflavin attenuates necroptosis, thereby extending the current understanding of its pleiotropic metabolic effects.

Exercise, lactate, and adaptive myofiber necroptosis

Muscle hypertrophy, the process of muscle growth, has long been hypothesized to involve microtrauma—microscopic myofiber damage that triggers repair and subsequent growth. This process is chemically mediated rather than purely mechanical and typically manifests in the days following strenuous exercise.[66] Despite these insights, the precise molecular pathways linking microtrauma to muscle growth have remained poorly understood.

During exercise, increased energy demand in glycolytic fibers drives glucose catabolism and elevated pyruvate production; when pyruvate production exceeds oxidative capacity, the surplus is converted to lactate by LDHA.[67] Although lactate production during exercise has been recognized since Berzelius first documented it in 1808,[68] its precise role in exercise-induced microtrauma and subsequent muscle growth has remained unresolved.

Our data demonstrate that lactate, beyond its role as a metabolic byproduct, functions as a signaling molecule that promotes myofiber necroptosis following intense exercise. This necroptotic process induces microtrauma and creates a permissive niche for MuSC activation, ultimately facilitating muscle repair and hypertrophy. By linking exercise-induced lactate production, myofiber necroptosis, and MuSC activation, these findings offer a molecular framework for understanding how a single metabolite can serve opposing roles—driving pathological tissue destruction in I/R injury and IAV infection, while mediating adaptive remodeling in the context of exercise.

Limitations of the study

Several limitations of the present study should be acknowledged. First, the identity of PCAF as a lactyltransferase rests on biochemical and cellular evidence, but the precise mechanism by which PCAF differentiates a lactyl from an acetyl group for transfer to RIPK3-K63 remains to be fully resolved. A central unresolved question in the broader lactylation field concerns the acyl-donor substrate: whether lactyltransferases utilize lactyl-CoA directly or whether lactylation proceeds through a non-enzymatic or alternative enzymatic route remains actively debated.[36,42] Based on current understanding of protein lactylation, lactyl-CoA represents the most plausible acyl-donor molecule for PCAF-mediated RIPK3-K63 lactylation; however, the precise role of lactyl-CoA in the context of necroptosis remains to be fully established. Direct biochemical demonstration that PCAF utilizes lactyl-CoA as the acyl donor for RIPK3 lactylation, together with structural evidence for lactyl-group accommodation within the PCAF active site, will therefore be important priorities for future investigation. It should also be noted that the complete metabolic pathway linking intracellular lactate metabolism to RIPK3-K63 lactylation remains to be fully elucidated, and the intermediate steps governing this process warrant further investigation. Second, the *in vivo* models employed—cardiac I/R injury, IAV infection, and resistance exercise—involve complex systemic responses, and the contribution of RIPK3-K63 lactylation relative to other concurrent necroptotic and inflammatory signals cannot be fully disentangled from the current data. In addition, while our exercise studies demonstrate that exercise-induced lactate accumulation promotes RIPK3-K63 lactylation-associated myofiber necroptosis and is linked to muscle adaptation, the complete physiological sequence connecting these events to enhanced exercise performance remains more inferential and requires further investigation. Third, the pharmacological tools used to inhibit LDH and PCAF *in vivo* lack complete selectivity, and potential off-target metabolic or epigenetic effects cannot be excluded. Cell-type-specific genetic models will be required to establish causality more rigorously. Finally, all therapeutic evidence presented here is preclinical; whether RIPK3-K63 lactylation is similarly operative in human disease contexts and whether its inhibition would be safe and efficacious in patients remain to be determined.

Taken together, our findings establish lactate as a metabolic input that is decoded by the necroptotic machinery through PCAF-mediated RIPK3-K63 lactylation, coupling the dynamic fluctuations of a single metabolite to cell-death outcomes across both pathological injury and adaptive physiology.

RESOURCE AVAILABILITY

Lead contact

The lead contact, Liming Sun (liming.sun@sibcb.ac.cn), is responsible for all communications with the journal before and after publication, as well as for conveying relevant information and updates to all co-authors.

Materials availability

Plasmids and cell lines are available on request, but we may require a completed materials transfer agreement if there is potential for commercial application. The mouse lines used are all available at the Shanghai Model Organisms Center, as listed in the key resources table. The LC-MS/MS data for lysine lactylation of RIPK3 (Figures 3F2, S3A, and S3B) have been deposited in the iProX database (https://www.iprox.cn/). Accession numbers are listed in the key resources table.

Data and code availability

- Please refer to Data S1 for all raw data used to plot the figures as well as the raw immunoblot scans.
- This paper does not report original code.
- The corresponding author can provide additional supporting data for the findings of this study upon reasonable request.

ACKNOWLEDGMENTS

We sincerely thank Professor Dangsheng Li for his critical insights and discussions in this work. This study was supported by the Noncommunicable Chronic Diseases-National Science and Technology Major Project (2025ZD0547800), the Strategic Priority Research Program of the Chinese Academy of Science (XDB0990000), the National Natural Science Foundation of China (82471595, 82470283, and 81970211), National Key Research and Development Program of China (2023YFA0914903), CAS Youth Interdisciplinary Team, the Liaoning Revitalization Talents Program (XLYC1901003 and XLYC2403104), and the Science Foundation for Outstanding Young Scientists Fund of Liaoning Province (2026JH6/101100006).

AUTHOR CONTRIBUTIONS

Y.S., N.Z., and L.S. contributed to the conception and design of the study. X.H., S.L., Y. Zou, W.Z., L.W., S.Y., X.L., H.L., Y. Zhang, G.S., H.Z., P.Z., J.L., C.C., Z.Z., Y.C., F.W., J.G., A.N., and Y.G. performed all the molecular and biochemistry experiments and the mouse experiments. C.C., Z.Z., and Y.G. prepared samples for mass spectrometry analysis. N.Z., L.C., S.Y., S.L., Y. Zou, and P.W. contributed to the analysis and interpretation of the data. L.S., Y.S., and N.Z. contributed to writing the manuscript. Y.S. and L.S. supervised the study.

DECLARATION OF INTERESTS

The authors declare no competing interests.

STAR★METHODS

Detailed methods are provided in the online version of this paper and include the following:

- KEY RESOURCES TABLE
- EXPERIMENTAL MODEL AND STUDY PARTICIPANT DETAILS
  - Cell culture
  - Animals
- METHOD DETAILS
  - Metabolite interference compound screening
  - Plasmid transfection and viral infection
  - Cell viability measurement
  - SYTOX Green staining assay
  - Lactate measurement
  - Acetyl-CoA measurements
  - Nuclear and Cytoplasmic Protein Fractionation
  - Western blot and immunoprecipitation
  - Quantitative real-time PCR (qRT-PCR)
  - LC-MS/MS Analysis
  - Establishment of site-specific lysine lactylation
  - Immunofluorescence staining
  - Recombinant PCAF and MLKL purification
  - *In vitro* lactylation assay
  - *In vitro* kinase assay
  - PI staining
  - MST analysis
  - TNFα-induced SIRS model
  - Mouse myocardial I/R assay
  - Influenza virus infection experiment
  - Mouse high-intensity exercise assay and LDH inhibitor treatment
  - Muscle stem cells isolation and FACS analysis
  - TTC staining
  - H&E staining
- QUANTIFICATION AND STATISTICAL ANALYSIS

SUPPLEMENTAL INFORMATION

Supplemental information can be found online at https://doi.org/10.1016/j.cmet.2026.08.022.

Received: June 13, 2026
Revised: August 7, 2026
Accepted: August 31, 2026
Published: September 23, 2026

REFERENCES

1. Newton, K., Strasser, A., Kayagaki, N., and Dixit, V.M. (2024). Cell death. Cell *187*, 235–256. https://doi.org/10.1016/j.cell.2023.11.044.
2. Yuan, J., and Ofengeim, D. (2024). A guide to cell death pathways. Nat. Rev. Mol. Cell Biol. *25*, 379–395. https://doi.org/10.1038/s41580-023-00689-6.
3. Rickard, J.A., O'Donnell, J.A., Evans, J.M., Lalaoui, N., Poh, A.R., Rogers, T., Vince, J.E., Lawlor, K.E., Ninnis, R.L., Anderton, H., et al. (2014). RIPK1 regulates RIPK3-MLKL-driven systemic inflammation and emergency hematopoiesis. Cell *157*, 1175–1188. https://doi.org/10.1016/j.cell.2014.04.019.
4. Gong, T., Liu, L., Jiang, W., and Zhou, R. (2020). DAMP-sensing receptors in sterile inflammation and inflammatory diseases. Nat. Rev. Immunol. *20*, 95–112. https://doi.org/10.1038/s41577-019-0215-7.
5. Linkermann, A., Hackl, M.J., Kunzendorf, U., Walczak, H., Krautwald, S., and Jevnikar, A.M. (2013). Necroptosis in immunity and ischemia-reperfusion injury. Am. J. Transplant. *13*, 2797–2804. https://doi.org/10.1111/ajt.12448.
6. Balachandran, S., and Rall, G.F. (2020). Benefits and Perils of Necroptosis in Influenza Virus Infection. J. Virol. *94*, e01101-19. https://doi.org/10.1128/JVI.01101-19.
7. Duprez, L., Takahashi, N., Van Hauwermeiren, F., Vandendriessche, B., Goossens, V., Vanden Berghe, T., Declercq, W., Libert, C., Cauwels, A., and Vandenabeele, P. (2011). RIP kinase-dependent necrosis drives lethal systemic inflammatory response syndrome. Immunity *35*, 908–918. https://doi.org/10.1016/j.immuni.2011.09.020.
8. Zhou, S.A., Zhang, W., Cai, G., Ding, Y., Wei, C., Li, S., Yang, Y., Qin, J., Liu, D., Zhang, H., et al. (2020). Myofiber necroptosis promotes muscle stem cell proliferation via releasing Tenascin-C during regeneration. Cell Res. *30*, 1063–1077. https://doi.org/10.1038/s41422-020-00393-6.
9. Ai, Y., Meng, Y., Yan, B., Zhou, Q., and Wang, X. (2024). The biochemical pathways of apoptotic, necroptotic, pyroptotic, and ferroptotic cell death. Mol. Cell *84*, 170–179. https://doi.org/10.1016/j.molcel.2023.11.040.
10. Jiao, H., Wachsmuth, L., Kumari, S., Schwarzer, R., Lin, J., Eren, R.O., Fisher, A., Lane, R., Young, G.R., Kassiotis, G., et al. (2020). Z-nucleic-acid sensing triggers ZBP1-dependent necroptosis and inflammation. Nature *580*, 391–395. https://doi.org/10.1038/s41586-020-2129-8.
11. Sun, L., Wang, H., Wang, Z., He, S., Chen, S., Liao, D., Wang, L., Yan, J., Liu, W., Lei, X., et al. (2012). Mixed lineage kinase domain-like protein mediates necrosis signaling downstream of RIP3 kinase. Cell *148*, 213–227. https://doi.org/10.1016/j.cell.2011.11.031.
12. Cai, Z., Jitkaew, S., Zhao, J., Chiang, H.C., Choksi, S., Liu, J., Ward, Y., Wu, L.G., and Liu, Z.G. (2014). Plasma membrane translocation of trimerized MLKL protein is required for TNF-induced necroptosis. Nat. Cell Biol. *16*, 55–65. https://doi.org/10.1038/ncb2883.
13. Chen, X., Li, W., Ren, J., Huang, D., He, W.T., Song, Y., Yang, C., Li, W., Zheng, X., Chen, P., et al. (2014). Translocation of mixed lineage kinase domain-like protein to plasma membrane leads to necrotic cell death. Cell Res. *24*, 105–121. https://doi.org/10.1038/cr.2013.171.
14. Dondelinger, Y., Declercq, W., Montessuit, S., Roelandt, R., Goncalves, A., Bruggeman, I., Hulpiau, P., Weber, K., Sehon, C.A., Marquis, R.W., et al. (2014). MLKL compromises plasma membrane integrity by binding to phosphatidylinositol phosphates. Cell Rep. *7*, 971–981. https://doi.org/10.1016/j.celrep.2014.04.026.
15. Hildebrand, J.M., Tanzer, M.C., Lucet, I.S., Young, S.N., Spall, S.K., Sharma, P., Pierotti, C., Garnier, J.M., Dobson, R.C.J., Webb, A.I., et al. (2014). Activation of the pseudokinase MLKL unleashes the four-helix bundle domain to induce membrane localization and necroptotic cell

death. Proc. Natl. Acad. Sci. USA *111*, 15072–15077. https://doi.org/10.1073/pnas.1408987111.

16. Wang, H., Sun, L., Su, L., Rizo, J., Liu, L., Wang, L.F., Wang, F.S., and Wang, X. (2014). Mixed lineage kinase domain-like protein MLKL causes necrotic membrane disruption upon phosphorylation by RIP3. Mol. Cell *54*, 133–146. https://doi.org/10.1016/j.molcel.2014.03.003.
17. Samson, A.L., Zhang, Y., Geoghegan, N.D., Gavin, X.J., Davies, K.A., Mlodzianoski, M.J., Whitehead, L.W., Frank, D., Garnish, S.E., Fitzgibbon, C., et al. (2020). MLKL trafficking and accumulation at the plasma membrane control the kinetics and threshold for necroptosis. Nat. Commun. *11*, 3151. https://doi.org/10.1038/s41467-020-16887-1.
18. Murphy, J.M., Czabotar, P.E., Hildebrand, J.M., Lucet, I.S., Zhang, J.G., Alvarez-Diaz, S., Lewis, R., Lalaoui, N., Metcalf, D., Webb, A.I., et al. (2013). The pseudokinase MLKL mediates necroptosis via a molecular switch mechanism. Immunity *39*, 443–453. https://doi.org/10.1016/j.immuni.2013.06.018.
19. Cho, Y.S., Challa, S., Moquin, D., Genga, R., Ray, T.D., Guildford, M., and Chan, F.K.M. (2009). Phosphorylation-driven assembly of the RIP1-RIP3 complex regulates programmed necrosis and virus-induced inflammation. Cell *137*, 1112–1123. https://doi.org/10.1016/j.cell.2009.05.037.
20. He, S., Wang, L., Miao, L., Wang, T., Du, F., Zhao, L., and Wang, X. (2009). Receptor interacting protein kinase-3 determines cellular necrotic response to TNF-alpha. Cell *137*, 1100–1111. https://doi.org/10.1016/j.cell.2009.05.021.
21. Zhang, D.W., Shao, J., Lin, J., Zhang, N., Lu, B.J., Lin, S.C., Dong, M.Q., and Han, J. (2009). RIP3, an energy metabolism regulator that switches TNF-induced cell death from apoptosis to necrosis. Science *325*, 332–336. https://doi.org/10.1126/science.1172308.
22. Szobi, A., Gonçalvesová, E., Varga, Z.V., Leszek, P., Kuśmierczyk, M., Hulman, M., Kyselovič, J., Ferdinandy, P., and Adameová, A. (2017). Analysis of necroptotic proteins in failing human hearts. J. Transl. Med. *15*, 86. https://doi.org/10.1186/s12967-017-1189-5.
23. Koudstaal, S., Oerlemans, M.I.F.J., Van der Spoel, T.I.G., Janssen, A.W.F., Hoefer, I.E., Doevendans, P.A., Sluijter, J.P.G., and Chamuleau, S.A.J. (2015). Necrostatin-1 alleviates reperfusion injury following acute myocardial infarction in pigs. Eur. J. Clin. Invest. *45*, 150–159. https://doi.org/10.1111/eci.12391.
24. Luedde, M., Lutz, M., Carter, N., Sosna, J., Jacoby, C., Vucur, M., Gautheron, J., Roderburg, C., Borg, N., Reisinger, F., et al. (2014). RIP3, a kinase promoting necroptotic cell death, mediates adverse remodelling after myocardial infarction. Cardiovasc. Res. *103*, 206–216. https://doi.org/10.1093/cvr/cvu146.
25. Zhang, T., Yin, C., Boyd, D.F., Quarato, G., Ingram, J.P., Shubina, M., Ragan, K.B., Ishizuka, T., Crawford, J.C., Tummers, B., et al. (2020). Influenza Virus Z-RNAs Induce ZBP1-Mediated Necroptosis. Cell *180*, 1115–1129.e13. https://doi.org/10.1016/j.cell.2020.02.050.
26. Gautam, A., Boyd, D.F., Nikhar, S., Zhang, T., Siokas, I., Van de Velde, L.A., Gaevert, J., Meliopoulos, V., Thapa, B., Rodriguez, D.A., et al. (2024). Necroptosis blockade prevents lung injury in severe influenza. Nature *628*, 835–843. https://doi.org/10.1038/s41586-024-07265-8.
27. Wang, Y., Hao, Q., Florence, J.M., Jung, B.G., Kurdowska, A.K., Samten, B., Idell, S., and Tang, H. (2019). Influenza Virus Infection Induces ZBP1 Expression and Necroptosis in Mouse Lungs. Front. Cell. Infect. Microbiol. *9*, 286. https://doi.org/10.3389/fcimb.2019.00286.
28. Kuriakose, T., Man, S.M., Malireddi, R.K.S., Karki, R., Kesavardhana, S., Place, D.E., Neale, G., Vogel, P., and Kanneganti, T.D. (2016). ZBP1/DAI is an innate sensor of influenza virus triggering the NLRP3 inflammasome and programmed cell death pathways. Sci. Immunol. *1*, aag2045. https://doi.org/10.1126/sciimmunol.aag2045.
29. Wei, W., Riley, N.M., Lyu, X., Shen, X., Guo, J., Raun, S.H., Zhao, M., Moya-Garzon, M.D., Basu, H., Sheng-Hwa Tung, A., et al. (2023). Organism-wide, cell-type-specific secretome mapping of exercise training in mice. Cell Metab. *35*, 1261–1279.e11. https://doi.org/10.1016/j.cmet.2023.04.011.
30. Yang, Y., Zhang, J., Lv, M., Cui, N., Shan, B., Sun, Q., Yan, L., Zhang, M., Zou, C., Yuan, J., et al. (2024). Defective prelamin A processing promotes unconventional necroptosis driven by nuclear RIPK1. Nat. Cell Biol. *26*, 567–580. https://doi.org/10.1038/s41556-024-01374-2.
31. Weber, K., Roelandt, R., Bruggeman, I., Estornes, Y., and Vandenabeele, P. (2018). Nuclear RIPK3 and MLKL contribute to cytosolic necrosome formation and necroptosis. Commun. Biol. *1*, 6. https://doi.org/10.1038/s42003-017-0007-1.
32. Yoon, S., Bogdanov, K., Kovalenko, A., and Wallach, D. (2016). Necroptosis is preceded by nuclear translocation of the signaling proteins that induce it. Cell Death Differ. *23*, 253–260. https://doi.org/10.1038/cdd.2015.92.
33. Degterev, A., Hitomi, J., Germscheid, M., Ch'en, I.L., Korkina, O., Teng, X., Abbott, D., Cuny, G.D., Yuan, C., Wagner, G., et al. (2008). Identification of RIP1 kinase as a specific cellular target of necrostatins. Nat. Chem. Biol. *4*, 313–321. https://doi.org/10.1038/nchembio.83.
34. Yang, D., Liang, Y., Zhao, S., Ding, Y., Zhuang, Q., Shi, Q., Ai, T., Wu, S.Q., and Han, J. (2020). ZBP1 mediates interferon-induced necroptosis. Cell. Mol. Immunol. *17*, 356–368. https://doi.org/10.1038/s41423-019-0237-x.
35. He, S., Liang, Y., Shao, F., and Wang, X. (2011). Toll-like receptors activate programmed necrosis in macrophages through a receptor-interacting kinase-3-mediated pathway. Proc. Natl. Acad. Sci. USA *108*, 20054–20059. https://doi.org/10.1073/pnas.1116302108.
36. Zhang, D., Tang, Z., Huang, H., Zhou, G., Cui, C., Weng, Y., Liu, W., Kim, S., Lee, S., Perez-Neut, M., et al. (2019). Metabolic regulation of gene expression by histone lactylation. Nature *574*, 575–580. https://doi.org/10.1038/s41586-019-1678-1.
37. Gaffney, D.O., Jennings, E.Q., Anderson, C.C., Marentette, J.O., Shi, T., Schou Oxvig, A.M., Streeter, M.D., Johannsen, M., Spiegel, D.A., Chapman, E., et al. (2020). Non-enzymatic Lysine Lactoylation of Glycolytic Enzymes. Cell Chem. Biol. *27*, 206–213.e6. https://doi.org/10.1016/j.chembiol.2019.11.005.
38. Zhang, N., Zhang, Y., Xu, J., Wang, P., Wu, B., Lu, S., Lu, X., You, S., Huang, X., Li, M., et al. (2023). α-myosin heavy chain lactylation maintains sarcomeric structure and function and alleviates the development of heart failure. Cell Res. *33*, 679–698. https://doi.org/10.1038/s41422-023-00844-w.
39. Chen, H., Li, Y., Li, H., Chen, X., Fu, H., Mao, D., Chen, W., Lan, L., Wang, C., Hu, K., et al. (2024). NBS1 lactylation is required for efficient DNA repair and chemotherapy resistance. Nature *631*, 663–669. https://doi.org/10.1038/s41586-024-07620-9.
40. Zong, Z., Xie, F., Wang, S., Wu, X., Zhang, Z., Yang, B., and Zhou, F. (2024). Alanyl-tRNA synthetase, AARS1, is a lactate sensor and lactyltransferase that lactylates p53 and contributes to tumorigenesis. Cell *187*, 2375–2392.e33. https://doi.org/10.1016/j.cell.2024.04.002.
41. Mao, Y., Zhang, J., Zhou, Q., He, X., Zheng, Z., Wei, Y., Zhou, K., Lin, Y., Yu, H., Zhang, H., et al. (2024). Hypoxia induces mitochondrial protein lactylation to limit oxidative phosphorylation. Cell Res. *34*, 13–30. https://doi.org/10.1038/s41422-023-00864-6.
42. Chen, Y., Wu, J., Zhai, L., Zhang, T., Yin, H., Gao, H., Zhao, F., Wang, Z., Yang, X., Jin, M., et al. (2024). Metabolic regulation of homologous recombination repair by MRE11 lactylation. Cell *187*, 294–311.e21. https://doi.org/10.1016/j.cell.2023.11.022.
43. Shvedunova, M., and Akhtar, A. (2022). Modulation of cellular processes by histone and non-histone protein acetylation. Nat. Rev. Mol. Cell Biol. *23*, 329–349. https://doi.org/10.1038/s41580-021-00441-y.
44. Clements, A., Rojas, J.R., Trievel, R.C., Wang, L., Berger, S.L., and Marmorstein, R. (1999). Crystal structure of the histone acetyltransferase domain of the human PCAF transcriptional regulator bound to coenzyme A. EMBO J. *18*, 3521–3532. https://doi.org/10.1093/emboj/18.13.3521.
45. Varner, E.L., Trefely, S., Bartee, D., von Krusenstiern, E., Izzo, L., Bekeova, C., O'Connor, R.S., Seifert, E.L., Wellen, K.E., Meier, J.L., et al. (2020). Quantification of lactoyl-CoA (lactyl-CoA) by liquid chromatography mass spectrometry in mammalian cells and tissues. Open Biol. *10*, 200187. https://doi.org/10.1098/rsob.200187.

46. Santos-Rosa, H., Valls, E., Kouzarides, T., and Martínez-Balbás, M. (2003). Mechanisms of P/CAF auto-acetylation. Nucleic Acids Res. *31*, 4285–4292. https://doi.org/10.1093/nar/gkg655.

47. Blanco, J.C., Minucci, S., Lu, J., Yang, X.J., Walker, K.K., Chen, H., Evans, R.M., Nakatani, Y., and Ozato, K. (1998). The histone acetylase PCAF is a nuclear receptor coactivator. Genes Dev. *12*, 1638–1651. https://doi.org/10.1101/gad.12.11.1638.

48. Fuernau, G., Desch, S., de Waha-Thiele, S., Eitel, I., Neumann, F.-J., Hennersdorf, M., Felix, S.B., Fach, A., Böhm, M., Pöss, J., et al. (2020). Arterial Lactate in Cardiogenic Shock: Prognostic Value of Clearance Versus Single Values. JACC Cardiovasc. Interv. *13*, 2208–2216. https://doi.org/10.1016/j.jcin.2020.06.037.

49. Zhang, W., Wang, G., Xu, Z.-G., Tu, H., Hu, F., Dai, J., Chang, Y., Chen, Y., Lu, Y., Zeng, H., et al. (2019). Lactate Is a Natural Suppressor of RLR Signaling by Targeting MAVS. Cell *178*, 176–189.e15. https://doi.org/10.1016/j.cell.2019.05.003.

50. Zhang, Y., Chang, L., Xin, X., Qiao, Y., Qiao, W., Ping, J., Xia, J., and Su, J. (2024). Influenza A virus-induced glycolysis facilitates virus replication by activating ROS/HIF-1α pathway. Free Radic. Biol. Med. *225*, 910–924. https://doi.org/10.1016/j.freeradbiomed.2024.10.304.

51. Newton, K., Dugger, D.L., Maltzman, A., Greve, J.M., Hedehus, M., Martin-McNulty, B., Carano, R.A., Cao, T.C., van Bruggen, N., Bernstein, L., et al. (2016). RIPK3 deficiency or catalytically inactive RIPK1 provides greater benefit than MLKL deficiency in mouse models of inflammation and tissue injury. Cell Death Differ. *23*, 1565–1576. https://doi.org/10.1038/cdd.2016.46.

52. Mao, C., Wang, M., Zhuang, L., and Gan, B. (2024). Metabolic cell death in cancer: ferroptosis, cuproptosis, disulfidptosis, and beyond. Protein Cell *15*, 642–660. https://doi.org/10.1093/procel/pwae003.

53. Yang, X.J., Ogryzko, V.V., Nishikawa, J., Howard, B.H., and Nakatani, Y. (1996). A p300/CBP-associated factor that competes with the adenoviral oncoprotein E1A. Nature *382*, 319–324. https://doi.org/10.1038/382319a0.

54. Wong, K., Zhang, J., Awasthi, S., Sharma, A., Rogers, L., Matlock, E.F., Van Lint, C., Karpova, T., McNally, J., and Harrod, R. (2004). Nerve growth factor receptor signaling induces histone acetyltransferase domain-dependent nuclear translocation of p300/CREB-binding protein-associated factor and hGCN5 acetyltransferases. J. Biol. Chem. *279*, 55667–55674. https://doi.org/10.1074/jbc.M408174200.

55. Chakravarti, D., Ogryzko, V., Kao, H.Y., Nash, A., Chen, H., Nakatani, Y., and Evans, R.M. (1999). A viral mechanism for inhibition of p300 and PCAF acetyltransferase activity. Cell *96*, 393–403. https://doi.org/10.1016/s0092-8674(00)80552-8.

56. Gjesdal, G., Braun, O.Ö., Smith, J.G., Scherstén, F., and Tydén, P. (2018). Blood lactate is a predictor of short-term mortality in patients with myocardial infarction complicated by heart failure but without cardiogenic shock. BMC Cardiovasc. Disord. *18*, 8. https://doi.org/10.1186/s12872-018-0744-1.

57. Zymliński, R., Biegus, J., Sokolski, M., Siwołowski, P., Nawrocka-Millward, S., Todd, J., Jankowska, E.A., Banasiak, W., Cotter, G., Cleland, J.G., et al. (2018). Increased blood lactate is prevalent and identifies poor prognosis in patients with acute heart failure without overt peripheral hypoperfusion. Eur. J. Heart Fail. *20*, 1011–1018. https://doi.org/10.1002/ejhf.1156.

58. Biegus, J., Zymliński, R., Sokolski, M., Jankowska, E.A., Banasiak, W., and Ponikowski, P. (2019). Elevated lactate in acute heart failure patients with intracellular iron deficiency as identifier of poor outcome. Kardiol. Pol. *77*, 347–354. https://doi.org/10.5603/KP.a2019.0014.

59. Stanley, W.C., Hall, J.L., Stone, C.K., and Hacker, T.A. (1992). Acute myocardial ischemia causes a transmural gradient in glucose extraction but not glucose uptake. Am. J. Physiol. *262*, H91–H96. https://doi.org/10.1152/ajpheart.1992.262.1.H91.

60. Vogt, A.M., Ackermann, C., Yildiz, M., Schoels, W., and Kübler, W. (2002). Lactate accumulation rather than ATP depletion predicts ischemic myocardial necrosis: implications for the development of lethal myocardial injury. Biochim. Biophys. Acta *1586*, 219–226. https://doi.org/10.1016/s0925-4439(01)00100-4.

61. Williamson, J.R., Schaffer, S.W., Ford, C., and Safer, B. (1976). Contribution of tissue acidosis to ischemic injury in the perfused rat heart. Circulation *53*, I3–I14.

62. Thyrsted, J., Storgaard, J., Blay-Cadanet, J., Heinz, A., Thielke, A.L., Crotta, S., de Paoli, F., Olagnier, D., Wack, A., Hiller, K., et al. (2021). Influenza A induces lactate formation to inhibit type I IFN in primary human airway epithelium. iScience *24*, 103300. https://doi.org/10.1016/j.isci.2021.103300.

63. Chen, F., Elgaher, W.A.M., Winterhoff, M., Büssow, K., Waqas, F.H., Graner, E., Pires-Afonso, Y., Casares Perez, L., de la Vega, L., Sahini, N., et al. (2022). Citraconate inhibits ACOD1 (IRG1) catalysis, reduces interferon responses and oxidative stress, and modulates inflammation and cell metabolism. Nat. Metab. *4*, 534–546. https://doi.org/10.1038/s42255-022-00577-x.

64. Keshavarz, M., Solaymani-Mohammadi, F., Namdari, H., Arjeini, Y., Mousavi, M.J., and Rezaei, F. (2020). Metabolic host response and therapeutic approaches to influenza infection. Cell. Mol. Biol. Lett. *25*, 15. https://doi.org/10.1186/s11658-020-00211-2.

65. Ferriero, R., Nusco, E., De Cegli, R., Carissimo, A., Manco, G., and Brunetti-Pierri, N. (2018). Pyruvate dehydrogenase complex and lactate dehydrogenase are targets for therapy of acute liver failure. J. Hepatol. *69*, 325–335. https://doi.org/10.1016/j.jhep.2018.03.016.

66. Fehrenbach, E., and Schneider, M.E. (2006). Trauma-induced systemic inflammatory response versus exercise-induced immunomodulatory effects. Sports Med. *36*, 373–384. https://doi.org/10.2165/00007256-200636050-00001.

67. Brooks, G.A. (1986). The lactate shuttle during exercise and recovery. Med. Sci. Sports Exerc. *18*, 360–368. https://doi.org/10.1249/00005768-198606000-00019.

68. Philp, A., Macdonald, A.L., and Watt, P.W. (2005). Lactate–a signal coordinating cell and systemic function. J. Exp. Biol. *208*, 4561–4575. https://doi.org/10.1242/jeb.01961.

STAR★METHODS

KEY RESOURCES TABLE

REAGENT or RESOURCE	SOURCE	IDENTIFIER
Antibodies		
Anti-RIPK3	Cell Signaling Technology	Cat# 95702S; RRID: AB_2721823
Anti-phospho-RIPK3	Cell Signaling Technology	Cat# 91702S; RRID: AB_2937060
Anti-MLKL	Abcam	Cat# ab243142; RRID: AB_3718640
Anti-phospho-MLKL	Abcam	Cat# ab208910; RRID: AB_2687465
Anti-pan L-lactyl-lysine (Pan-Kla)	PTM Biolabs	Cat# PTM-1401RM; RRID: AB_2942013
Anti-RIPK3-K63 lactyl-lysine (RIPK3-K63la)	HuaBio	N/A
Anti-acetylated-lysine	Cell Signaling Technology	Cat# 9441L; RRID: AB_331805
Anti-PCAF (KAT2B)	Cell Signaling Technology	Cat# 3378S; RRID: AB_2128409
Anti-MYST1 (MOF / KAT8)	Cell Signaling Technology	Cat# 46862S; RRID: AB_2799311
Anti-MYST2 (HBO1 / KAT7)	Cell Signaling Technology	Cat# 58418S; RRID: AB_2799547
Anti-TIP60 (KAT5)	Proteintech	Cat# 10827-1-AP; RRID: AB_2128431
Anti-GCN5 (KAT2A)	Proteintech	Cat# 66575-1-Ig; RRID: AB_2881935
Anti-HAT1	Proteintech	Cat# 11432-1-AP; RRID: AB_2116435
Anti-GTF3C4	Proteintech	Cat# 17653-1-AP; RRID: AB_2115253
Anti-NAA60	Affinity Biosciences	Cat# DF13864; RRID: N/A
Anti-AARS2	Abcam	Cat# ab197367; RRID: AB_2943036
Anti-LDHA	Proteintech	Cat# 19987-1-AP; RRID: AB_10646429
Anti-LDHB	Proteintech	Cat# 14824-1-AP; RRID: AB_2134953
Anti-Flag	Abmart	Cat# M20008M; RRID: AB_2713960
Anti-HA	Cell Signaling Technology	Cat# 3724S; RRID: AB_1549585
Anti-Myc	Cell Signaling Technology	Cat# 2276S; RRID: AB_331783
Anti-GAPDH	Proteintech	Cat# 10494-1-AP; RRID: AB_2263076
Anti-Lamin B1	Proteintech	Cat# 12987-1-AP; RRID: AB_2136290
Anti-Tubulin	Proteintech	Cat# 11224-1-AP; RRID: AB_2210206
Anti-PAX7	DSHB	Cat# PAX7; RRID: AB_528428
Normal rabbit IgG	Beyotime Biotechnology	Cat# A7016; RRID: AB_2905533
Normal mouse IgG	Beyotime Biotechnology	Cat# A7028; RRID: AB_2909433
Normal rat IgG	Beyotime Biotechnology	Cat# A21040; RRID: AB_3739885
Alexa Fluor 488 goat anti-rabbit IgG	Invitrogen	Cat# A11034; RRID: AB_2576217
Alexa Fluor 488 goat anti-mouse IgG	Invitrogen	Cat# A11029; RRID: AB_2534088
Alexa Fluor 546 F(ab')2 goat anti-mouse IgG	Invitrogen	Cat# A11018; RRID: AB_2534085
PerCP/Cy5.5 anti-CD45	BD Biosciences	Cat# 550994; RRID: AB_394003
PerCP/Cy5.5 anti-CD11b	BioLegend	Cat# 101228; RRID: AB_893232
PerCP/Cy5.5 anti-CD31	BioLegend	Cat# 102420; RRID: AB_10613644
AF700 anti-Sca1	BioLegend	Cat# 108142; RRID: AB_2565959
Biotin anti-mouse CD106	BioLegend	Cat# 105704; RRID: AB_313205
PE/Cy7-Streptavidin	BioLegend	Cat# 405206; RRID: N/A
Bacterial and virus strains		
Influenza A virus A/Common Shelduck/HB3/Hebei/2021 (H5N1)	Key Laboratory of Jilin Province for Zoonoses Prevention and Control	N/A
E. coli BL21(DE3)	GoldBio	Cat# CC-103
Chemicals, peptides, and recombinant proteins		
TNF-α (recombinant), mouse	MedChemExpress	Cat# HY-P7090
TNF-α (recombinant), human	MedChemExpress	Cat# HY-P7058

(*Continued on next page*)

Continued

REAGENT or RESOURCE	SOURCE	IDENTIFIER
z-VAD-FMK	MedChemExpress	Cat# HY-16658B
LCL161 (Smac mimetic)	MedChemExpress	Cat# HY-15518
Necrostatin-1 (Nec-1)	MedChemExpress	Cat# HY-15760
Cycloheximide (CHX)	ApexBio Technology	Cat# A8244
Lipopolysaccharide (LPS)	Sigma-Aldrich	Cat# L4130
Poly(I:C)	TargetMol	Cat# T23171
Galloflavin	MedChemExpress	Cat# HY-W040118
FX11	MedChemExpress	Cat# HY-16214
GSK2837808A	MedChemExpress	Cat# HY-100681
Sodium oxamate	MedChemExpress	Cat# HY-W013032A
Stiripentol	MedChemExpress	Cat# HY-103392
PCAF-IN-1	MedChemExpress	Cat# HY-147894
CPTH2	MedChemExpress	Cat# HY-W013274
Leptomycin B (LMB)	MedChemExpress	Cat# HY-16909
Selinexor	MedChemExpress	Cat# HY-17536
Recombinant Flag-PCAF (KAT2B)	Active Motif	Cat# 81142, 81842
IPTG	AMRESCO	Cat# 0487
Lipofectamine 3000	Invitrogen	Cat# L3000015
HiGene	Applygen	Cat# c1506
jetPRIME	Polyplus	Cat# PT114-15
Protein A/G magnetic beads	Biotool	Cat# B23202
WB and IP lysis buffer	Beyotime Biotechnology	Cat# P0013
TRIzol Reagent	Thermo Fisher Scientific	Cat# 15596026CN
RBC lysis buffer	Thermo Fisher Scientific	Cat# 00-4333-57
Dispase II	Roche	Cat# 04942078001
Collagenase, Type IV	Thermo Fisher Scientific	Cat# 17104019
Cell strainers (40 μm, 70 μm)	WHB Scientific	Cat# WHB-40UM; WHB-70UM
2,3,5-Triphenyltetrazolium chloride (TTC)	Solarbio	Cat# G3005
Lactyl-CoA	MedChemExpress	Cat# HY-141540
ATP	MedChemExpress	Cat# HY-B2176
Sodium butyrate	Sigma-Aldrich	Cat# B5887
L-Glutathione reduced	MedChemexpress	Cat# HY-D0187
PMSF	MedChemExpress	Cat# HY-B0496
DAPI	MedChemExpress	Cat# HY-D0814
SYTOX Green Nucleic Acid Stain	Thermo Fisher Scientific	Cat# S7020
Tamoxifen	MedChemExpress	Cat# HY-13757A
His-RIPK3 kinase domain	Shanghai Institute of Materia Medica, Chinese Academy of Sciences	N/A
Recombinant mouse MLKL (181–464 aa), His-tagged	Shanghai Institute of Materia Medica, Chinese Academy of Sciences	N/A
Critical commercial assays		
CellTiter-Glo Luminescent Cell Viability Assay Kit	Promega	Cat# G7573
Annexin V-AbFluor™ 488/PI Apoptosis Detection Kit	Abbkine	Cat# KTA0002
CheKine™ Lactate Assay Kit	Abbkine	Cat# KTB1100
CheKine™ Acetyl-CoA Assay Kit	Abbkine	Cat# KTB1260
PrimeScript™ RT Master Mix	Takara	Cat# RR036A
ChamQ Universal SYBR qPCR Master Mix	Vazyme	Cat# Q711-02
Enhanced BCA Protein Assay Kit	Beyotime	Cat# P0009

(*Continued on next page*)

Continued

REAGENT or RESOURCE	SOURCE	IDENTIFIER
Deposited data		
Raw and analyzed proteomics data	This paper	iProX database (https://www.iprox.cn/) Accession number: IPX0019163000
Raw data for graphs and uncropped blots	This paper	Data S1
Experimental models: Cell lines		
Mouse: L929	Procell	Cat# CL-0137
Human: HEK293T	Procell	Cat# CL-0005
Mouse: *Ripk3*-KO L929	This paper	N/A
Mouse: primary MEF	This paper	N/A
Mouse: primary BMDM	This paper	N/A
Mouse: shRIPK3-L929	This paper	N/A
Experimental models: Organisms/strains		
Mouse: RIPK3-K63R knock-in (C57BL/6J background)	Shanghai Model Organisms Center	N/A
Mouse: $Mlkl^{-/-}$ (C57BL/6J background)	This paper	N/A
Mouse: *Myh6-Cre*$^{+}$; $Ldha^{f/f}$ (C57BL/6J background)	Shanghai Model Organisms Center	N/A
Mouse: C57BL/6J (wild-type)	N/A	N/A
Oligonucleotides		
siRNA targeting sequence: Scramble: UUCUCCGAACGUGUCACGU	This paper	N/A
siRNA targeting sequence: Ldha: CCAUCAGUAUCUUAAUGAA	This paper	N/A
siRNA targeting sequence: Ldhb: GGGAAAGUCUCUGGCUGAU	This paper	N/A
siRNA targeting sequence: Pcaf: GAAGAAGUGUAUAGUCAAA	This paper	N/A
siRNA targeting sequence: Hbo1-464: CGACGUCGAUUUCACGAAA	This paper	N/A
siRNA targeting sequence: Hbo1-905: GAGGAUUUGGAGAAGUUAA	This paper	N/A
siRNA targeting sequence: Hbo1-1410: GGAAGAUGCUGAUCGAUUU	This paper	N/A
siRNA targeting sequence: Tip60-236: GCAAUGAAAUUUACCGCAA	This paper	N/A
siRNA targeting sequence: Tip60-390: GACGGAGUAUGACUGCAAA	This paper	N/A
siRNA targeting sequence: Tip60-424: GGCUACUUCUCCAAGGAAA	This paper	N/A
siRNA targeting sequence: Hat1-600: GCUACAUGACAGUCUAUAA	This paper	N/A
siRNA targeting sequence: Hat1-990: GCUACAGACUGGAUAUUAA	This paper	N/A
siRNA targeting sequence: Hat1-1177: CAUUGAGCGACUUGCUCAA	This paper	N/A
siRNA targeting sequence: Aars2-273: GGCAGGCUUCCGACGUGUA	This paper	N/A
siRNA targeting sequence: Aars2-319: GGACCGAUUGUGUCUUGAU	This paper	N/A
siRNA targeting sequence: Aars2-590: CCUUCGGACCACAAGAGAA	This paper	N/A
siRNA targeting sequence: Gtf3c4-77: CAAUGGGUUGUGAUGCAAA	This paper	N/A

(*Continued on next page*)

Continued

REAGENT or RESOURCE	SOURCE	IDENTIFIER
siRNA targeting sequence: Gtf3c4-209: GUCUUUAUGAGACUAGUUA	This paper	N/A
siRNA targeting sequence: Gtf3c4-717: GAAGUGUAGCUGUAGCUUA	This paper	N/A
siRNA targeting sequence: Naa60-7: GUAGCUGAAAUAAAGAAUA	This paper	N/A
siRNA targeting sequence: Naa60-241: GCAAUAAACUUCUAUGAAA	This paper	N/A
siRNA targeting sequence: Naa60-508: GGCAUAGAGUACAGCCGUA	This paper	N/A
siRNA targeting sequence: Mof-595: GGCAAACUCAGCUACAGAA	This paper	N/A
siRNA targeting sequence: Mof-710: GGAAGGAGAUCUAUCGAAA	This paper	N/A
siRNA targeting sequence: Mof-1343: CGAAGCACAAACAAGUCAA	This paper	N/A
siRNA targeting sequence: Gcn5-560: CAGACACCAAACAAGUCUA	This paper	N/A
siRNA targeting sequence: Gcn5-841: GCUACCUACAAAGUCAAUU	This paper	N/A
siRNA targeting sequence: Gcn5-1883: GCCGCUAUCUGGGCUACAU	This paper	N/A
Primer: Gapdh Forward: ACTCCCACTCTTCCACCTTCG	This paper	N/A
Primer: Gapdh Reverse: CACCCTGTTGCTGTAGCCGTA	This paper	N/A
Primer: IL-6 Forward: TAGTCCTTCCTACCCCAATTTCC	This paper	N/A
Primer: IL-6 Reverse: TTGGTCCTTAGCCACTCCTTC	This paper	N/A
Primer: Ccl2 Forward: TGGCTCAGCCAGATGCAGT	This paper	N/A
Primer: Ccl2 Reverse: TTGGGATCATCTTGCTGGTG	This paper	N/A
Primer: Cxcl10 Forward: GTCTGAGTGGGACTCAAGGGATCCC	This paper	N/A
Primer: Cxcl10 Reverse: CATCGTGGCAATGATCTCAACACGT	This paper	N/A
Primer: Ifi47 Forward: GTTAGAACCAAGGTGGATAGTGAC	This paper	N/A
Primer: Ifi47 Reverse: CGAGATATTGGGCAAGAGCA	This paper	N/A
Primer: Ifi44 Forward: AACTGACTGCTCGCAATAATGT	This paper	N/A
Primer: Ifi44 Reverse: GTAACACAGCAATGCCTCTTGT	This paper	N/A
Primer: Inhba Forward: AGGTGCTGCTCAAGTGCCAATA	This paper	N/A
Primer: Inhba Reverse: TCTTTCGGGTCCCTTCTGTTTT	This paper	N/A
Primer: Cxcl1 Forward: CTGGGATTCACCTCAAGAACATC	This paper	N/A
Primer: Cxcl1 Reverse: CAGGGTCAAGGCAAGCCTC	This paper	N/A

(*Continued on next page*)

Continued

REAGENT or RESOURCE	SOURCE	IDENTIFIER
Primer: Cxcl2 Forward: GGCAAGGCTAACTGACCTGGAAAGG	This paper	N/A
Primer: Cxcl2 Reverse: ACAGCGAGGCACATCAGGTACGA	This paper	N/A
Primer: IL-23α Forward: TGTGACCCACAAGGACTCAAG	This paper	N/A
Primer: IL-23α Reverse: GATCCTTTGCAAGCAGAACTGG	This paper	N/A
Primer: Tgtp1 Forward: TGCACAGATGGGGATGAATTTC	This paper	N/A
Primer: Tgtp1 Reverse: TCACTGTCGAGAGACTCCTGA	This paper	N/A
Primer: Ccr2 Forward: GCTCTACATTCACTCCTTCCAC	This paper	N/A
Primer: Ccr2 Reverse: ACCACTGTCTTTGAGGCTTG	This paper	N/A
Primer: Cxcl12 Forward: ACCAGTCAGCCTGAGCTACC	This paper	N/A
Primer: Cxcl12 Reverse: TAATTTCGGGTCAATGCACA	This paper	N/A
Primer: IL-1b Forward: TGCCACCTTTTGACAGTGATG	This paper	N/A
Primer: IL-1b Reverse: AAGGTCCACGGGAAAGACAC	This paper	N/A
Primer: Cxcr3 Forward: GCGTGTACTGCAGCTAGTGG	This paper	N/A
Primer: Cxcr3 Reverse: TAGCAGTAGGCCATGACCAGA	This paper	N/A
Primer: Gbp4 Forward: TGGGGGACACAGGCTCTACA	This paper	N/A
Primer: Gbp4 Reverse: GCCTGCAGGATGGAACTCTCAA	This paper	N/A
Recombinant DNA		
Plasmid: Flag-mRIPK3-WT	GeneChem	GOSE0347066
Plasmid: Flag-mRIPK3-K63R	GeneChem	GOSE0347067
Plasmid: Myc-mRIPK3-WT	This paper	N/A
Plasmid: Myc-mRIPK3-K63R	This paper	N/A
Plasmid: Myc-hRIPK3-WT	This paper	N/A
Plasmid: Myc-hRIPK3-K62R	This paper	N/A
Plasmid: Flag-hMLKL (C-terminal)	This paper	N/A
Plasmid: Flag-mPCAF	GeneChem	GOSE0417943
Plasmid: Flag-mp300	GeneChem	GOSE0417641
Plasmid: Flag-mCBP	GeneChem	GOSE0417642
Plasmid: Myc-mGCN5	GeneChem	GOSE5021640
Plasmid: NLS-Flag-mRIPK3	This paper	N/A
Plasmid: Myc-mMOF (KAT8)	GeneChem	GOSE5021634
Plasmid: Myc-mHBO1 (KAT7)	GeneChem	GOSE5021635
Plasmid: Myc-mTIP60 (KAT5)	GeneChem	GOSE5021636
Plasmid: Myc-mHAT1	GeneChem	GOSE5021637
Plasmid: Myc-mGTF3C4	GeneChem	GOSE5021638
Plasmid: Myc-mNAA60	GeneChem	GOSE5021639

(*Continued on next page*)

Continued

REAGENT or RESOURCE	SOURCE	IDENTIFIER
Plasmid: HA-mAARS1	GeneChem	GOSE5001299
Plasmid: HA-mAARS2	GeneChem	GOSE5002932
Software and algorithms		
GraphPad Prism 10.0	Software	https://www.graphpad.com/
SPSS 22.0	Software	https://www.ibm.com/
ImageJ	Software	https://imagej.nih.gov/ij/
Incucyte software	Software	https://www.sartorius.com/
FlowJo V10	Software	https://www.flowjo.com/
MO.Affinity Analysis v2.3	Software	https://nanotempertech.com/
MaxQuant v1.6.15.0	Software	https://www.maxquant.org/
Proteome Discoverer 2.4	Software	https://www.thermofisher.com/

EXPERIMENTAL MODEL AND STUDY PARTICIPANT DETAILS

Cell culture

L929 and HEK293T cells were obtained from the American Type Culture Collection. shRIPK3 L929 was kindly provided by Prof. Cao Liu. Embryos were removed from pregnant mice at 14 to 16 days of gestation. After removal of the head and viscera, the tissues were minced and digested with trypsin to obtain single-cell suspensions, which were then cultured to establish MEFs. Mouse bone marrow-derived macrophages (BMDMs) were isolated from C57BL/6J mice. Tibias and femurs of mice were dissected and their marrow flushed out. Cells were seeded in 96-well plates and differentiated for 7 days at 37 °C in medium containing 50 ng/mL M-CSF. Generally, cells were cultured in high-glucose Dulbecco's Modified Eagle Medium (DMEM) supplemented with 10% fetal bovine serum (FBS), 100 μg/mL penicillin, and 100 μg/mL streptomycin. Cultures were maintained in a humidified atmosphere of 5% CO_2 at 37 °C.

Animals

RIPK3-K63R knock-in (KI) mice, with K63R point mutations in the *Ripk3* gene and the *Myh6-Cre*$^{+}$*; Ldha*$^{f/f}$ mice, with myocardium-specific Ldha knockout, were generated by the Shanghai Model Organisms Center, Inc. (Shanghai, China). The RIPK3-K63R KI mice were created using CRISPR/Cas9 technology to introduce the K63R point mutation through homologous recombination repair. Briefly, Cas9 mRNA and guide RNA (gRNA) were synthesized via *in vitro* transcription, and the donor DNA oligo was synthesized. The Cas9 mRNA, gRNA, and donor DNA were microinjected into fertilized C57BL/6J mouse eggs to produce F0 mice. Genotyping was performed by PCR and sequencing using the following primers: F1: 5'-TCTGGTGAGCCGTGAAGAAC-3'; R1: 5'-TAGGTAGCACATCCCCAGCA-3'.

To induce *Ldha* knockout in *Myh6-Cre*$^{+}$*; Ldha*$^{f/f}$ mice, male mice (8–10 weeks old) were administered 50 mg/kg tamoxifen intraperitoneally for 5 consecutive days. In a separate group, mice were treated with either DMSO or 50 mg/kg/day of the LDHA inhibitor Galloflavin.

Mice were housed in a specific-pathogen-free (SPF) barrier facility under a 12 h light/dark cycle (22–24 °C, 40–60% humidity), with *ad libitum* access to food and water. All anmals were healthy and were not immune compromised. The animal procedures were approved by the Animal Science Committee of China Medical University and were conducted in accordance with the Animal Welfare Regulations of China Medical University (CMU20250065, CMU20241390, CMU20251385); by the Research Ethics Committee, Center for Excellence in Molecular Cell Science, Chinese Academy of Sciences (SIBCB-S361-1807-023); and by the Institutional Animal Care and Use Committee of the Academy of Military Medical Sciences (IACUC of AMMS-2024-046). This study adhered to the guidelines for the care and use of laboratory animals set forth by the National Institutes of Health (NIH Publication Nos. 85-23, revised in 1985).

METHOD DETAILS

Metabolite interference compound screening

Compound screening was performed using a compound library comprising a wide range of Metabolite Interference Compound. Compounds were dispensed onto L929 cells for pre-treatment using the Bravo robotic system (Agilent), with a 12-hour incubation period. Each plate included a positive control (Necrostatin-1) and a negative control (DMSO). After pre-treatment, necroptosis was induced in L929 cells by adding TNFα and z-VAD for 6 hours. Cell viability was assessed by measuring luminescence-based ATP levels using the CellTiter-Glo ATP assay (Promega).

Plasmid transfection and viral infection

Myc-RIPK3-WT (mouse and human), Myc-mRIPK3-K63R, Myc-hRIPK3-K62R, NLS(nuclear localization signal)-Flag-mRIPK3 and Flag-hMLKL were cloned into pHAGE plasmid and delivered into cells with lentivirus. Plasmid sequences were confirmed by DNA

sequencing prior to transfection. Plasmid transfections into L929 cells were performed using Lipofectamine 3000 (Cat# L3000015; Invitrogen, USA), HiGene (Cat# C1506; Applygen, China), and jetPRIME (Cat# PT114-15; Polyplus, France) according to the manufacturer's instructions. Cells were harvested 48–72 h post-transfection for further analysis.

siRNA transfections into L929 cells were performed using jetPRIME transfection reagent according to the manufacturer's protocol. Cells were harvested 48–72 h post-transfection for further analysis. The specific siRNA sequences are summarized in the key resources table.

Cell viability measurement

L929 cells (8,000–10,000 cells/well) were seeded in 96-well plates and cultured for 24 hours. Similarly, MEFs (8,000 cells/well) were inoculated in 96-well plates and cultured for 24 hours. Intracellular ATP levels were measured in the remaining cells to assess cell viability using the CellTiter-Glo Luminescent Cell Viability Assay Kit (Cat#G7573; Promega) according to the manufacturer's instructions.

SYTOX Green staining assay

L929 cells were transfected with Flag-RIPK3 (WT or K63R) via Lipofectamine 3000. After 24 h, cells were pretreated with Galloflavin (100 μM) or DMSO for 24 h, followed by TNF-α (50 ng/mL) and zVAD (20 μM) stimulation. SYTOX Green (Thermo Fisher Scientific, 100 nM) was added 10 min pre-imaging. Images were captured hourly for 8 h using Incucyte system. SYTOX Green-positive cells were quantified using Incucyte software.

Lactate measurement

Lactate concentrations in mouse heart tissues, gastrocnemius muscles, L929 cells, and MEFs (intracellular lactate) were measured using the CheKine™ Lactate Assay Kit (Cat#KTB1100; Abbkine, China) according to the manufacturer's instructions.

Acetyl-CoA measurements

Intracellular acetyl-CoA was quantified by ultra-high-performance liquid chromatography coupled to high-resolution tandem mass spectrometry. Cells were extracted with 600 μL ice-cold (−20 °C) methanol and homogenized (60 Hz, 60 s); 600 μL ice-cold chloroform was then added (1,400 rpm, 1 min), followed by 240 μL room-temperature ultrapure water, and the mixture was kept on ice for 10 min. After centrifugation (12,000 rpm, 2 min, 4 °C), 250 μL of the supernatant was evaporated to dryness in a vacuum concentrator, reconstituted in 50 μL methanol/water (3:2, v/v), and 2 μL was injected. Chromatographic separation was performed on a Waters CSH C18 column (2.1 × 50 mm, 1.7 μm) at 40 °C, using mobile phase A (10 mM ammonium acetate in ultrapure water) and mobile phase B (acetonitrile) at 0.4 mL/min (6.5% to 95% B over 0–3 min, held to 5 min; total run 7.5 min). Detection was carried out on a Thermo Scientific Vanquish Core UHPLC coupled to a Q Exactive HF-X Orbitrap mass spectrometer in positive electrospray ionization mode (spray voltage 3,200 V; capillary temperature 320 °C; sheath gas 30 arb; auxiliary gas 10 arb) with a Full MS/dd-MS2 acquisition. Acetyl-CoA was identified by matching its precursor and MS2 product ions against an acyl-CoA spectral library and quantified by external calibration against authentic standards (linear range 10–2,000 ng/mL; $R^2 > 0.99$), with correction for matrix effect and dilution. Acetyl-CoA content was normalized to total protein and expressed as ng per mg protein.

Intracellular Acetyl-CoA content was quantified using the CheKine Acetyl-CoA Assay Kit (Abbkine, Cat# KTB1260). Briefly, cells were homogenized in Extraction Buffer and centrifuged at 13,000 g for 10 min at 4°C. The Acetyl-CoA concentration in the supernatant was determined by monitoring the NADH generation rate via absorbance at 340 nm. Acetyl-CoA content was normalized to total protein and expressed as nmol per mg protein.

Nuclear and Cytoplasmic Protein Fractionation

Cells were harvested by trypsinization, washed with ice-cold PBS, and collected by centrifugation at 1,000 rpm for 3 min at 4°C. For cytoplasmic protein extraction, the cell pellet was resuspended in NP-40 lysis buffer (0.1% NP-40 in PBS) supplemented with protease and phosphatase inhibitors. After gentle vortexing and incubation on ice, the lysates were centrifuged at 1,200 rpm for 5 min at 4°C. The supernatant was collected as the cytoplasmic fraction.

The remaining nuclear pellet was washed once with NP-40 lysis buffer and twice with PBS to minimize cytoplasmic contamination. The pellet was then resuspended in Western/IP lysis buffer supplemented with inhibitors and subjected to sonication (30-40 pulses). Following centrifugation at 16,000 g for 10 min at 4°C, the supernatant was collected as the nuclear fraction. Protein concentrations were determined by BCA assay. The efficiency of the fractionation was validated by Western blot using GAPDH as the cytoplasmic marker and Lamin B1 as the nuclear marker.

Western blot and immunoprecipitation

Cells and tissues (myocardium, gastrocnemius muscle, lung, or small intestin) were lysed in lysis buffer (P0013; Beyotime) supplemented with protease inhibitors, phosphatase inhibitors, 10 mM sodium butyrate, and 10 mM nicotinamide. Tissues were homogenized at 4°C prior to centrifugation. Protein concentrations were determined via BCA assay. For Western blot, 10–50 μg of samples were resolved by SDS-PAGE and transferred to PVDF membranes. Target proteins (e.g., p-MLKL, p-RIPK3, RIPK3, LDHA) were detected using specific primary antibodies.

For co-immunoprecipitation (Co-IP), 2 mg of protein lysate was incubated with 2–3 μg of primary antibodies (specifically anti-RIPK3, anti-MLKL, anti-PCAF, or anti-Flag) and 30 μL of Protein A/G magnetic beads (#B23202; Biotool), anti-Myc beads, or anti-Flag affinity gel for 12 h at 4°C. Beads were washed with cold lysis buffer, and protein complexes were eluted with SDS loading buffer for further analysis.

Quantitative real-time PCR (qRT-PCR)

Total RNA was isolated using TRIzol Reagent (Thermo Fisher Scientific, Cat# 15596026CN) following the manufacturer's instructions. RNA concentration and quality were determined using a NanoDrop 2000 spectrophotometer (Thermo Fisher Scientific), with A260/A280 ratios ranging from 1.8 to 2.0. cDNA was synthesized from 1 μg total RNA using PrimeScript™ RT Master Mix (Takara, Cat# RR036A) in a 20 μL reaction (incubation at 37°C for 15 min, followed by enzyme inactivation at 85°C for 5 s). qPCR was performed in 20 μL reactions containing 2 μL cDNA, 10 μL 2× ChamQ Universal SYBR qPCR Master Mix (Vazyme, Cat# Q711-02), 0.4 μL each of forward and reverse primer (10 μM stock; 0.2 μM final), and 7.2 μL ddH_2O, using the CFX96 Real-Time PCR System (Bio-Rad). Amplification conditions were: initial denaturation at 95°C for 10 min, followed by 40 cycles of 95°C for 15 s and 60°C for 60 s. Melt curve analysis was performed from 65°C to 95°C with 0.5°C increments to verify specificity. Relative gene expression was calculated using the $2^{-\Delta\Delta Ct}$ method, with Gapdh as the reference gene. All reactions were run in technical triplicates, and data represents at least three independent biological experiments. The primer sequences are provided in the key resources table.

LC-MS/MS Analysis

Sample Preparation and Digestion

For endogenous lactylation analysis, L929 cells were treated with TNF-α (50 ng/mL) and zVAD (20 μM) for 6 h to induce necroptosis. Cells were lysed in lysis buffer supplemented with protease and phosphatase inhibitors, 10 mM sodium butyrate, and 10 mM nicotinamide. To enhance detection sensitivity, nuclear fractions were first enriched as described above. Endogenous RIPK3 was then immunoprecipitated from nuclear lysates using an anti-RIPK3 antibody. For *in vitro* samples, RIPK3 was recovered from the *in vitro* lactylation reaction described below.

Immunoprecipitated endogenous RIPK3 was digested directly on the beads: trypsin (Promega) was added to a final concentration of 20 ng/μL for overnight digestion, followed by reduction with 5 mM DTT at 37°C for 60 min and alkylation with 11 mM iodoacetamide in the dark at room temperature for 45 min; a second aliquot of trypsin was then added to 10 ng/μL for a further 4 h, and the resulting peptides were acidified and desalted. The *in vitro* reaction product was digested in solution: trypsin was added at a 1:50 enzyme-to-protein mass ratio for overnight digestion, followed by the same reduction and alkylation steps, a second digestion at a 1:100 ratio for 4 h, and desalting on a Strata-X SPE column (Phenomenex, 10 mg/1 mL).

DDA-based Discovery Mass Spectrometry

Peptides were reconstituted in 0.1% formic acid and separated using an EASY-nLC 1200 UPLC system (Thermo Fisher Scientific). Samples were loaded onto a 25-cm home-made reversed-phase analytical column (100 μm i.d.). The mobile phase consisted of solvent A (0.1% formic acid, 2% acetonitrile in water) and solvent B (0.1% formic acid in 90% acetonitrile). Peptides were separated with a 90-min gradient at a constant flow rate of 500 nL/min, using the following gradient of solvent B: 6%–23% for 0–68 min, 23%–32% for 68–82 min, 32%–80% for 82–86 min, and 80% for 86–90 min.

Mass spectrometry was performed on an Orbitrap Exploris 480 (Thermo Fisher Scientific) equipped with a nano-electrospray ion source and a FAIMS Pro interface. The electrospray voltage was set to 2300 V, with FAIMS compensation voltages of −45 V and −65 V. Full MS scans were acquired at a resolution of 60,000 (scan range: 400–1200 m/z), and MS/MS scans at a resolution of 15,000 with a fixed first mass of 110 m/z. Up to 25 most abundant precursors were selected for further MS/MS analyses with a dynamic exclusion of 20 s. HCD fragmentation was performed at a normalized collision energy (NCE) of 27%. Automatic Gain Control (AGC) target was set at 100%, with an intensity threshold of 5e4 ions/s and a maximum injection time set to Auto.

PRM-based Targeted Mass Spectrometry

For the *in vitro* lactylation reaction product, peptides were reconstituted in 0.1% formic acid and separated using an EASY-nLC 1200 UPLC system (Thermo Fisher Scientific). Samples were loaded onto a 25-cm home-made reversed-phase analytical column (100 μm i.d.). The mobile phase consisted of solvent A (0.1% formic acid, 2% acetonitrile in water) and solvent B (0.1% formic acid in 90% acetonitrile). Peptides were separated with a 60-min gradient at a constant flow rate of 500 nL/min, using the following gradient of solvent B: 8%–22% for 0–40 min, 22%–32% for 40–52 min, 32%–80% for 52–56 min, and 80% for 56–60 min.

Mass spectrometry was performed on an Orbitrap Exploris 480 (Thermo Fisher Scientific) in Parallel Reaction Monitoring (PRM) mode. The nano-electrospray voltage was set to 2100 V. Full MS scans were acquired at a resolution of 60,000 (scan range: 500–800 *m/z*), followed by targeted MS/MS scans at a resolution of 15,000 for specified RIPK3 precursors. HCD fragmentation was performed at a normalized collision energy (NCE) of 27%. Automatic Gain Control (AGC) targets were set at 300% for MS1 and 100% for MS/MS, with maximum injection times of 50 ms and 220 ms, respectively. The isolation window was set at 0.5 *m/z*.

For the endogenous RIPK3 immunoprecipitate, peptides were separated on a Vanquish Neo UPLC system (Thermo Fisher Scientific) using a 15-cm column (100 μm i.d.), with solvent A (0.1% formic acid in water) and solvent B (0.1% formic acid in 80% acetonitrile), over a 12-min gradient at a constant flow rate of 200 nL/min. Mass spectrometry was performed on an Orbitrap Astral (Thermo Fisher Scientific) in PRM mode, with a nano-electrospray voltage of 1900 V; precursors were detected in the Orbitrap analyzer and fragment ions in the Astral analyzer. Full MS scans were acquired at a resolution of 240,000 (scan range: 400–800 m/z), followed by targeted MS/MS scans at a resolution of 80,000. HCD fragmentation was performed at a normalized collision

energy (NCE) of 25%. The MS/MS Automatic Gain Control (AGC) target was set at 200%, with a maximum injection time of 20 ms and an isolation window of 0.6 m/z.

Data Processing and Site Identification

DDA raw data were processed using Proteome Discoverer 2.4. Tandem mass spectra were searched against the sequence of mouse RIPK3 as a single-entry database. Trypsin/P was specified as the cleavage enzyme allowing up to 4 missing cleavages; mass tolerances were 10 ppm for precursor ions and 0.02 Da for fragment ions. Carbamidomethyl on Cys was specified as fixed modification, and acetylation on protein N-terminal, oxidation on Met, and lactylation on Lys as variable modifications. The peptide ion score threshold was set above 0 and peptide confidence was set to low; as the search space comprised a single protein sequence, target–decoy FDR estimation was not applicable. PRM raw data were processed using MaxQuant (v1.6.15.0) and searched against the sequence of mouse RIPK3, concatenated with reverse decoy and contaminant databases. Trypsin/P was specified as the cleavage enzyme allowing up to 4 missing cleavages, with a maximum of 5 modifications per peptide; mass tolerances for precursor ions were 20 ppm in the first search and 4.5 ppm in the main search, and 20 ppm for fragment ions. Fixed and variable modifications were as described above. For the *in vitro* reaction product, the minimum peptide length was 7 amino acids and the FDR for protein, peptide and PSM identification was adjusted to < 1%. For the endogenous immunoprecipitate, the minimum peptide length was 6 amino acids and the FDR for protein and PSM identification was set to 5%.

Establishment of site-specific lysine lactylation

RIPK3-lacK63-specific antibody was prepared by Hua'an Biotechnology (Hangzhou, China). The RIPK3-lacK63 peptide (KISWEVK[Lactyl]AMVNLC) was first coupled to keyhole limpet hemocyanin and BSA, followed by multiple subcutaneous injections to immunize New Zealand white rabbits. Thereafter, blood was collected from the rabbits and the presence of RIPK3-lacK63-specific antibodies in the serum was evaluated using enzyme-linked immunosorbent assay (ELISA). For final antibody purification, the serum was eluted through the RIPK3-lacK63 peptide column and then passed through a non-RIPK3-lacK63 peptide column to obtain the specific antibody.

Immunofluorescence staining

To assess the intracellular localization of RIPK3 and PCAF, plasmids encoding Flag-RIPK3 were transfected into *Ripk3*-KO L929 cells, which were then treated with TNFα and z-VAD. For immunofluorescence staining, cells were first fixed in 4% paraformaldehyde (PFA) for 15 minutes, permeabilized with 0.3% Triton X-100 for 10 minutes, and blocked with 10% goat serum in PBS for 1 hour at room temperature. The cells were incubated overnight at 4°C with primary antibodies (anti-Flag and anti-PCAF). Following primary antibody incubation, cells were incubated with fluorescently conjugated secondary antibodies (Alexa Fluor 488 goat anti-rabbit IgG, Alexa Fluor 546 goat anti-mouse IgG, Invitrogen) for 1 hour at room temperature. The nuclei were counterstained with DAPI. Confocal images were acquired using a TCS SP8 STED X confocal microscope (Leica).

For PAX7 immunofluorescence, muscle tissue sections were brought to room temperature and fixed in 4% PFA for 20 minutes, followed by permeabilization with pre-chilled methanol for 10 minutes. Sections were then blocked with 5% BSA in PBS for 1 hour at room temperature. The sections were incubated overnight at 4°C with the primary antibody (anti-PAX7). Afterward, they were incubated with the fluorescent secondary antibody (Alexa Fluor 488 goat anti-mouse IgG, Invitrogen) for 1 hour at room temperature. Nuclei were stained with DAPI. Images were acquired using a BX53 microscope (Olympus).

Recombinant PCAF and MLKL purification

Recombinant Flag-PCAF (KAT2B) protein was purchased from Active Motif (CAT#81142, 81842, USA). Plasmid of recombinant MLKL (181-464aa) was transfected into E. coli BL21(DE3), and cultured at 37 °C. Protein expression was induced by adding 1 mM IPTG (AMRESCO, Cat# 0487) at OD600 = 0.6–0.8. Cells were cultured at 16 °C overnight. The harvested cells were lysed by sonication with lysis buffer (150 mM NaCl, 50 mM Tris-HCl, pH 8.0, 200 μg/mL PMSF and 0.2 mM β-mercaptoethanol), and centrifuged to remove the precipitate. The supernatant was incubated with GST agarose at 4 °C overnight. The GST agarose was subsequently washed and then eluted with 30 mM reduced glutathione (GSH). The eluted protein was further purified by gel filtration chromatography using the Superdex 200 10/300 GL column (GE Healthcare) at 4 °C in ÄKTA FPLC system (GE Healthcare).

In vitro lactylation assay

For *in vitro* lactylation, a reaction buffer containing 50 mM HEPES, 30 mM NaCl, 2.5 mM DTT, and 5 mM sodium butyrate was adjusted to a final pH of 7.5 prior to the addition of purified proteins. Purified His-tagged RIPK3 kinase domain (2 ug) and recombinant Flag-PCAF were then incubated in this buffer, supplemented with 20 μM lactyl-CoA and 1 mM ATP. The total volume was adjusted to 30 uL using ddH_2O. After incubation at 37°C for 30 min, the reaction was terminated by adding 6x SDS loading buffer and heating at 95°C for 7 min. Products were resolved by SDS-PAGE for subsequent western blotting or LC-MS/MS analysis as detailed above.

In vitro kinase assay

Flag-tagged RIPK3 (WT or K63R) was transfected into HEK293T cells, with or without Flag-tagged PCAF co-transfection where indicated. After 48 h, cells were harvested and lysed, and the Flag-tagged proteins were immunoprecipitated using anti-Flag affinity beads. The beads were washed three times with wash buffer [20 mM $MgCl_2$, 2 mM DTT, and 50 mM Tris-HCl (pH 7.5)]. For the kinase reaction, 5 μL of the protein-bound beads were resuspended in 29 μL of kinase buffer [20 mM $MgCl_2$, 100 μM ATP, 2 mM DTT, and

50 mM Tris-HCl (pH 7.5)] with the addition of purified recombinant MLKL (residues 181–464) as a substrate where indicated. The mixture was incubated at 30°C for indicated time intervals (0, 2, and 5 min). Reactions were terminated by adding 10 μL of 4× sample loading buffer and boiling at 100°C for 10 min. The resulting samples were resolved by SDS-PAGE and analyzed by immunoblotting using antibodies against p-MLKL, MLKL, p-RIPK3, and RIPK3.

PI staining

The Annexin V-AbFluor™ 488/PI Apoptosis Detection Kit (Cat#KTA0002; Abbkine) was used to assess cell death. Adherent L929 cells were stained by incubating with Annexin V buffer and propidium iodide (PI) for 15 minutes at room temperature in the dark. After incubation, cells were washed with 1× Annexin V Binding Buffer. The stained cells were then analyzed under a fluorescence microscope (Leica), and the cell death rate was quantified using ImageJ software.

MST analysis

Binding affinities between Lactyl-CoA and fluorescently labeled PCAF proteins were measured in binding buffer using a MONOLITH NT.115 system (NanoTemper Technologies). At room temperature, 10 μL of the target protein was mixed with 10 μL of twofold serially diluted Lactyl-CoA ligand. Measurements were performed on independent protein preparations, and data were analyzed by plotting Lactyl-CoA concentrations against fluorescence changes (change in raw fluorescence on the y-axis). Curve fitting was carried out, and dissociation constant (Kd) values were determined using MO.Affinity Analysis v2.3 software.

TNFα-induced SIRS model

8 weeks old mice were given intravenous injections of TNFα (430ng/kg). Mouse survival was monitored at 60-min intervals. The body temperature was monitored every 2 hours. The small intestines were collected right after the mice were euthanized and rinsed with PBS buffer. Intestines were then rolled into a Swiss roll and placed in 4% formalin buffer for 48 hours. The small intestine tissues were dehydrated and then embedded in paraffin. Samples were cut into 5-μm thick sections and stained with H&E.

Mouse myocardial I/R assay

For the myocardial ischemia/reperfusion (I/R) assay, mice were anesthetized with isoflurane (2%, ∼1500 mL/min) in oxygen. Adequate anesthesia depth was confirmed by the absence of the retraction reflex in the mid-scapular region. After endotracheal intubation, mice were ventilated with a miniature ventilator. The left anterior descending coronary artery (LAD) was ligated using a 6-0 suture (sham surgery without ligation). After 45 minutes of ischemia, reperfusion was initiated by releasing the knot for 4 hours. Following reperfusion, animals were sacrificed, and myocardial tissue was collected.

Influenza virus infection experiment

The A/Common Shelduck/HB3/Hebei/2021 (H5N1) virus used in this study was maintained in Key Laboratory of Jilin Province for Zoonoses Prevention and Control. Male WT and RIPK3-K63R KI mice, aged 9–10 weeks, were purchased from the Shanghai Model Organisms Center, Inc. All animal procedures were conducted in an animal biosafety level 3 (ABSL-3) facility.

For the infection, 10 mice per group were anesthetized with 1.25% avertin and intranasally inoculated with H5N1 at a dose of $10^{-7.0}$ LD50 in 50 μL per animal. At 7 days post-infection, three mice from each group were randomly selected for pathological examination. Their lungs were aseptically collected; a portion of the tissue was fixed in 4% paraformaldehyde for 48 hours and then sent to Jilin Hengjia Biotechnology Co., Ltd. for histopathological analysis. The remaining lung tissue was used for viral load quantification via fluorescence-based detection.

Mouse high-intensity exercise assay and LDH inhibitor treatment

The experiment was conducted using an FLS-PT treadmill (Future Life Science). The treadmill was equipped with a rear electrical stimulus grid set to deliver a 0.2 mA electric shock. Mice were considered to have reached the point of exhaustion when they could no longer continue running and made contact with the grid.

Prior to the formal testing, 8–10-week-old mice underwent a three-day acclimation period. During this period, mice ran on the treadmill with a 0-degree incline at a speed of 5 m/min for 10 minutes each day to familiarize them with the treadmill environment. After the acclimation phase, endurance running tests were conducted on the first and seventh days, while strength exercises were performed on the third and fifth days.

The exercise protocol began with a 5-minute warm-up at 5 m/min on a 0-degree incline. Following the warm-up, the treadmill speed gradually increased: the mice ran at 10 m/min for 10 minutes, followed by 15 m/min for 30 minutes. Finally, the speed was increased to 20 m/min, which was maintained until the mice could no longer keep up and exhausted. The time to exhaustion was recorded as the total running time from the start of the protocol until the mice reached exhaustion.

For localized pharmacological inhibition, a separate cohort of mice received bilateral intramuscular injections into the gastrocnemius muscle 30 min prior to the exercise challenge. Mice were treated with either Galloflavin (50 mg/kg/day), GSK2837808A (40 mg/kg/day), or vehicle (DMSO). Endurance capacity was subsequently assessed following the same exhaustion protocol described above.

Muscle stem cells isolation and FACS analysis

Mice after high-intensity exercise were euthanized by cervical dislocation, in accordance with institutional ethical guidelines for animal care. The gastrocnemius muscles were dissected and placed in 1 mL of muscle digestion solution (1.2 mg/mL Dispase II, 2 mg/mL Collagenase Type IV, and DMEM). The tissues were incubated at 37°C for 60 minutes to allow enzymatic digestion. Following digestion, 0.5 mL of fetal bovine serum (FBS) was added to terminate the reaction. The resulting cell suspension was filtered through a 70 μm cell strainer (WHB Scientific, Shanghai, China) to remove undigested tissue fragments. The cells were then subjected to red blood cell lysis by incubating with 3 mL of RBC lysis buffer (Thermo Fisher Scientific, Cat #00-4333-57) for 3 minutes, followed by washing with FACS buffer (PBS containing 1% FBS). After RBC lysis, the cell suspension was filtered again through a 40 μm cell strainer (WHB Scientific, Shanghai, China) to remove any remaining debris. For cell surface marker staining, a cocktail of antibodies was added, including PerCP/Cy5.5-CD45, CD11b, CD31, AF700-Sca1, and Biotin-Vcam (BioLegend), with each antibody used at a concentration of 0.5 μL per sample. The antibody mixture was incubated for 30 minutes on ice. After washing, cells were re-stained with PE/Cy7-Streptavidin (BioLegend) for an additional 15 minutes. For viability staining, SYTOX Green (Thermo Fisher Scientific, Cat# S7020) was added to a final concentration of 2.5 μM and incubated for 5 minutes on ice. Cells were washed with FACS buffer and analyzed using an LSRFortessa flow cytometer (BD Biosciences). The analyzed cell population, classified as MuSCs (Muscle Stem Cells), was selected based on the following markers: SYTOX $Green^{-}CD45^{-}CD11b^{-}CD31^{-}Sca1^{-}Vcam^{+}$. A total of 20,000 cells per sample were used for analysis.

TTC staining

2,3,5-Triphenyltetrazolium chloride (TTC) (Cat#G3005; Solarbio) staining was used to assess the mouse myocardial infarct area. The mouse heart was collected immediately after sacrifice and frozen at −80°C for 10 minutes. The heart was then sectioned into 1–2 mm slices and incubated in 2% TTC solution in a dark incubator at 37°C for 20 minutes. Following incubation, the heart slices were fixed in 4% paraformaldehyde for 24 hours. The infarct areas were photographed and analyzed using ImageJ software.

H&E staining

Intestinal tissues from TNFα-injected mice, and gastrocnemius muscles following exercise, were dehydrated through a graded ethanol series, embedded in paraffin, and sectioned to a thickness of 5 μm. Sections were then dewaxed, rehydrated, and stained with hematoxylin and eosin (H&E) to visualize nuclei and cytoplasm. Images of stained tissue sections were acquired using a high-resolution camera (Leica).

QUANTIFICATION AND STATISTICAL ANALYSIS

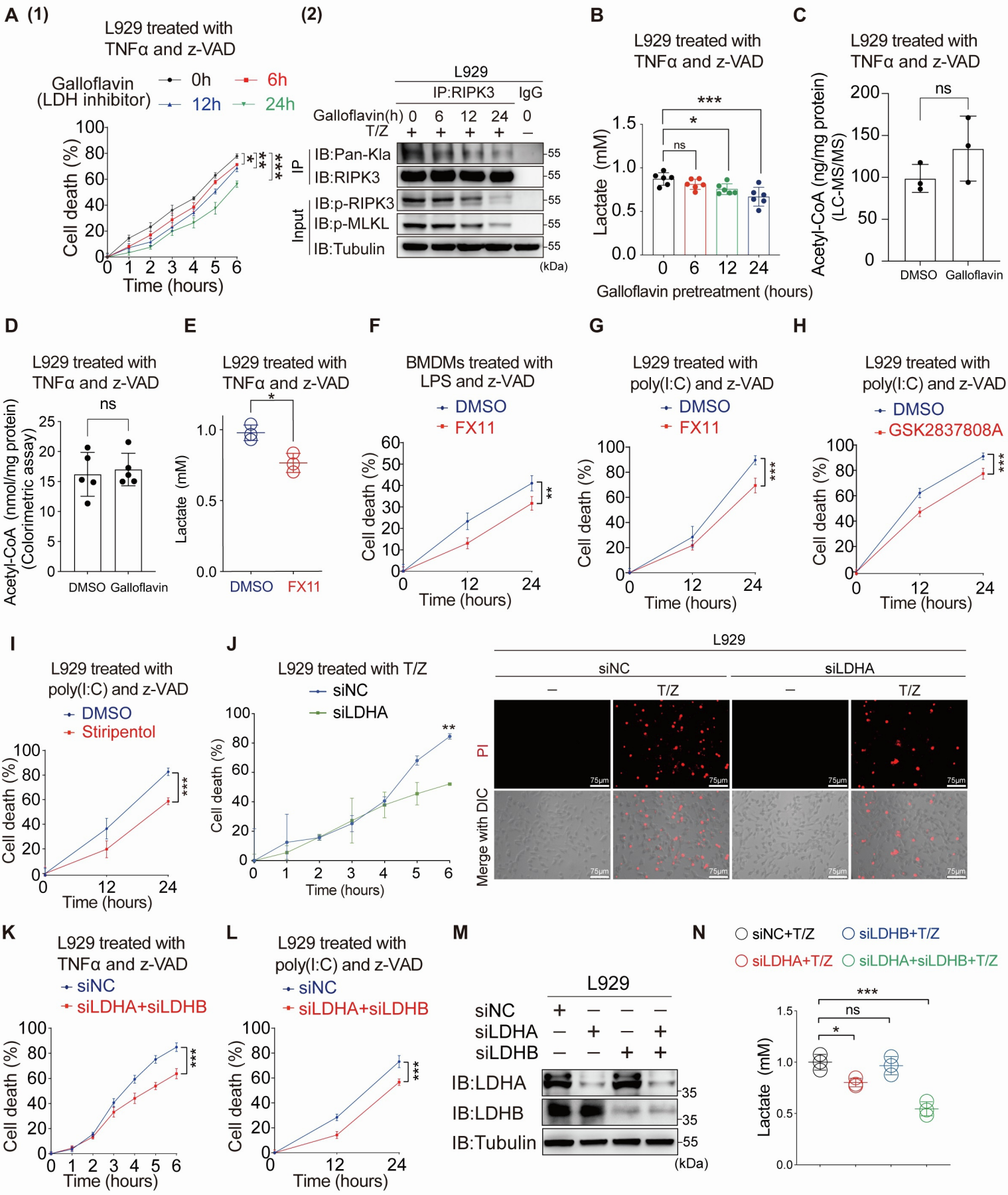
Data are presented as the mean ± standard deviation (SD). The F-test (for two groups) or the Brown–Forsythe test (for three or more groups) was used to assess the homogeneity of variances. The Shapiro–Wilk test was employed to evaluate the normality of the data. For comparisons between two groups, Student's t-test was used when variances were equal, and Welch's t-test was applied when variances were unequal. For multi-group comparisons, one-way or two-way ANOVA followed by Bonferroni's post-hoc test was performed. Mouse survival curves were analyzed using the Kaplan-Meier method and compared via the log-rank (Mantel-Cox) test. P-values were adjusted for multiple comparisons when appropriate. Statistical analyses were conducted using GraphPad Prism 10.0 (GraphPad, USA) and SPSS 22.0 (SPSS, USA), with a P-value of less than 0.05 considered statistically significant.

Cell Metabolism, Volume *38*

Supplemental information

Lactate couples metabolic state to necroptosis across pathological and physiological conditions

Naijin Zhang, Xinyue Huang, Saien Lu, Yuanming Zou, Guozhe Sun, Wei Zhang, Huijun Lu, Limin Wang, Xinxin Lu, Zhaobo Zhang, Cheng Cheng, Shilong You, He Zhang, Ying Zhang, Pengbo Wang, Pan Zhou, Juan Luo, Yuyi Chen, Feng Wu, Jiayan Guo, Anqi Ning, Yushan Guo, Liu Cao, Liming Sun, and Yingxian Sun



Supplementary Figure 1 | Pharmacological and genetic inhibition of LDHA/B confirms that blocking LDH suppresses necroptosis.

A. Time-course analysis of Galloflavin inhibition of necroptosis and its effects on RIPK3 lactylation. L929 cells were pre-treated with Galloflavin (100 μM) for 0, 6, 12, or 24 h, followed by T/Z (TNFα: 50 ng/mL; z-VAD: 20 μM) treatment for 6 h. (**1**) Time-course of cell death. (**2**) Whole cell lysates were immunoprecipitated with an anti-RIPK3 antibody or control IgG, followed by immunoblotting with the indicated antibodies.

B. Intracellular lactate levels in L929 cells pre-treated with Galloflavin (100 μM) for 0, 6, 12, or 24 h, followed by T/Z treatment for 6 h. Data were normalized to live cell number. n = 6 independent experiments.

C–D. Intracellular acetyl-CoA levels in L929 cells treated with DMSO or Galloflavin (100 μM, 24 h), measured by C, targeted LC–MS/MS and D, a colorimetric assay kit. Data were normalized to total protein. n = 3 (**C**) and n = 5 (**D**) independent experiments.

E. Quantification of intracellular lactate levels regulated by the LDHA inhibitor FX11. L929 cells were pre-treated with DMSO or FX11 (20 μM, 24 h) followed by T/Z treatment for 6 h. Data were normalized to total protein. n = 3 independent experiments.

F–G. The LDHA inhibitor FX11 suppresses necroptosis. Time-course analysis of cell death in cells treated with DMSO or FX11 (20 μM, 24 h) followed by necroptosis induction by F, LPS + z-VAD in BMDMs; G, Poly(I:C) + z-VAD in L929 cells. Cell viability was assessed by ATP levels.

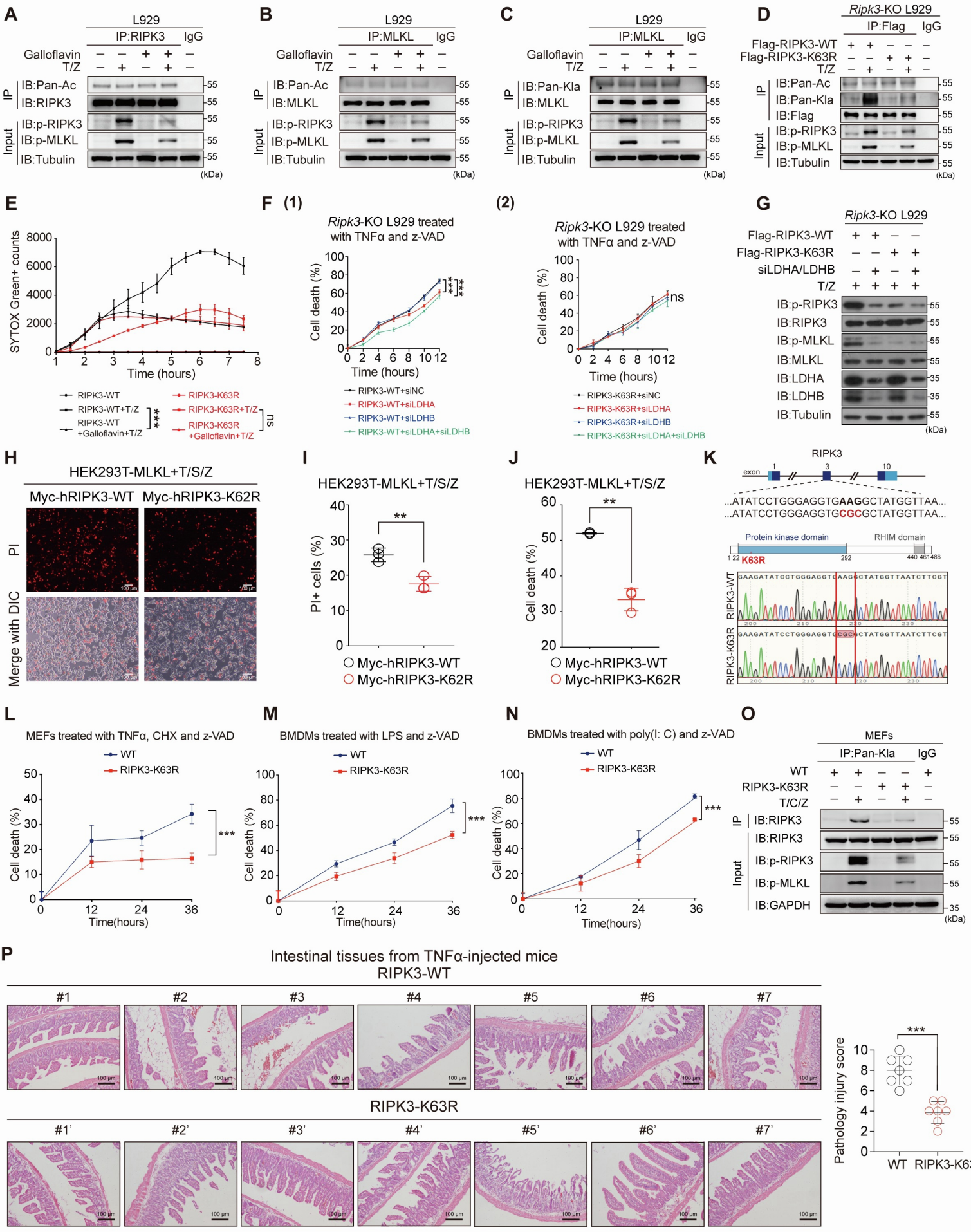
H. The LDHA inhibitor GSK2837808A suppresses necroptosis. Time-course analysis of cell viability in L929 cells treated with Poly(I:C) + z-VAD in the presence or absence of GSK2837808A (40 μM, 24 h). Cell viability was assessed by ATP levels.

I. The LDH inhibitor Stiripentol suppresses necroptosis. Time-course analysis of cell viability in L929 cells treated with DMSO or Stiripentol (250 μM, 24 h) followed by necroptosis induction by Poly(I:C) + z-VAD. Cell viability was assessed by ATP levels.

J. LDHA knockdown suppresses T/Z-induced necroptosis. L929 cells were transfected with siNC or siLDHA for 48 h, then treated with T/Z. Left: Time-course analysis of cell viability (ATP levels). Right: Representative PI staining at 3 h. Scale bar: 75 μm.

K–N. Simultaneous knockdown of LDHA and LDHB alleviates necroptosis and reduces lactate accumulation. L929 cells were transfected with siNC, siLDHA, siLDHB, or siLDHA plus siLDHB and stimulated with T/Z or Poly(I:C) + z-VAD.**K**. Time-course analysis of cell viability under T/Z stimulation. **L**. Time-course analysis of cell viability under Poly(I:C) + z-VAD stimulation. **M**. Immunoblot analysis validating LDHA and LDHB knockdown efficiency.**N**. Analysis of intracellular lactate concentration following T/Z treatment for 6 h. Knockdown of LDHA, and to a greater extent combined knockdown of LDHA and LDHB, reduced lactate accumulation during necroptosis.

Data are presented as mean ± SD; individual data points represent independent experiments. Statistical analysis for **B** was performed using one-way ANOVA with Dunnett's multiple comparisons test; **C–E** were analyzed using unpaired two-tailed t test with Welch's correction; **A (1), F–L**, and **N** were analyzed using two-way ANOVA with Bonferroni's multiple comparisons test. ns, not significant; *, $p < 0.05$; **, $p < 0.01$; ***, $p < 0.001$. Unless otherwise indicated, n = 3 independent experiments. All experiments were repeated at least three independent times; statistical analysis was conducted on pooled data from all replicates.



Supplementary Figure 2 | RIPK3-K63 lactylation promotes necroptosis in human and mouse cells.

A–C. Galloflavin does not affect RIPK3/MLKL acetylation or MLKL lactylation during necroptosis. L929 cells were pretreated with the LDH inhibitor Galloflavin (100 μM, 24 h), followed by treatment with or without T/Z (TNFα: 50 ng/mL; z-VAD: 20 μM) for 6 h. Endogenous RIPK3 (**A**) or MLKL (**B, C**) was immunoprecipitated from whole-cell lysates using the indicated antibodies or control IgG. The resulting precipitates were immunoblotted to analyze acetylation using a pan-acetyl-lysine antibody (**A, B**) or lactylation using a pan–L-lactyl lysine (pan-Kla) antibody (**C**). Levels of p-RIPK3 and p-MLKL were also assessed in whole-cell lysates. Tubulin was used as a loading control.

D. The K63R mutation abolished T/Z-induced RIPK3 lactylation, whereas acetylation was unaffected by either T/Z treatment or K63R substitution. Flag-RIPK3-WT or Flag-RIPK3-K63R was expressed in Ripk3-knockout L929 cells. After 24 h, cells were stimulated with or without T/Z for 6 h. Flag-RIPK3 was immunoprecipitated with anti-Flag antibody or control IgG, and lactylation and acetylation were analyzed by immunoblotting.

E. Incucyte live-cell analysis showing that the K63R mutation confers resistance to necroptosis, mimicking the effect of Galloflavin. Time-course quantification of cell death (SYTOX Green positive cell count) in Ripk3-knockout L929 cells reconstituted with Flag-RIPK3-WT or Flag-RIPK3-K63R, treated with or without T/Z in the presence or absence of Galloflavin (100 μM, 24 h pretreatment).

F–G. The protective effect of LDHA and LDHB knockdown against necroptosis requires RIPK3 K63 lactylation. Ripk3-knockout L929 cells were reconstituted with Flag-RIPK3-WT or Flag-RIPK3-K63R, transfected with siNC, siLDHA, siLDHB, or siLDHA plus siLDHB, and stimulated with T/Z.F. Time-course analysis of cell death. Knockdown of LDHA and LDHB protected WT-reconstituted cells (**1**) from necroptosis, an effect that was lost in K63R-reconstituted cells (**2**). G. Immunoblot analysis of p-RIPK3 and p-MLKL expression in the indicated cells following LDHA and LDHB knockdown and T/Z treatment.

H–J. The conserved RIPK3-K62R mutation reduces T/S/Z (TNFα/Smac mimetic/z-VAD-fmk)-induced necroptosis in human HEK293T cells. HEK293T cells were co-transfected with C-terminal Flag-tagged hMLKL and either Myc-hRIPK3-WT or Myc-hRIPK3-K62R (corresponding to K63 in mouse RIPK3; see Figure 2C) plasmids. Following transfection, cells were treated with T/S/Z for 6 h to induce necroptosis. Treatment conditions: TNFα (50 ng/mL), Smac mimetic (100 nM), and z-VAD (20 μM). **H**. Representative images of propidium iodide (PI) staining showing necroptotic cell death. Scale bar: 100 μm. **I**. Quantification of PI-positive necroptotic cells. **J**. Cell viability was measured by ATP levels and expressed as cell death (%) relative to untreated controls.

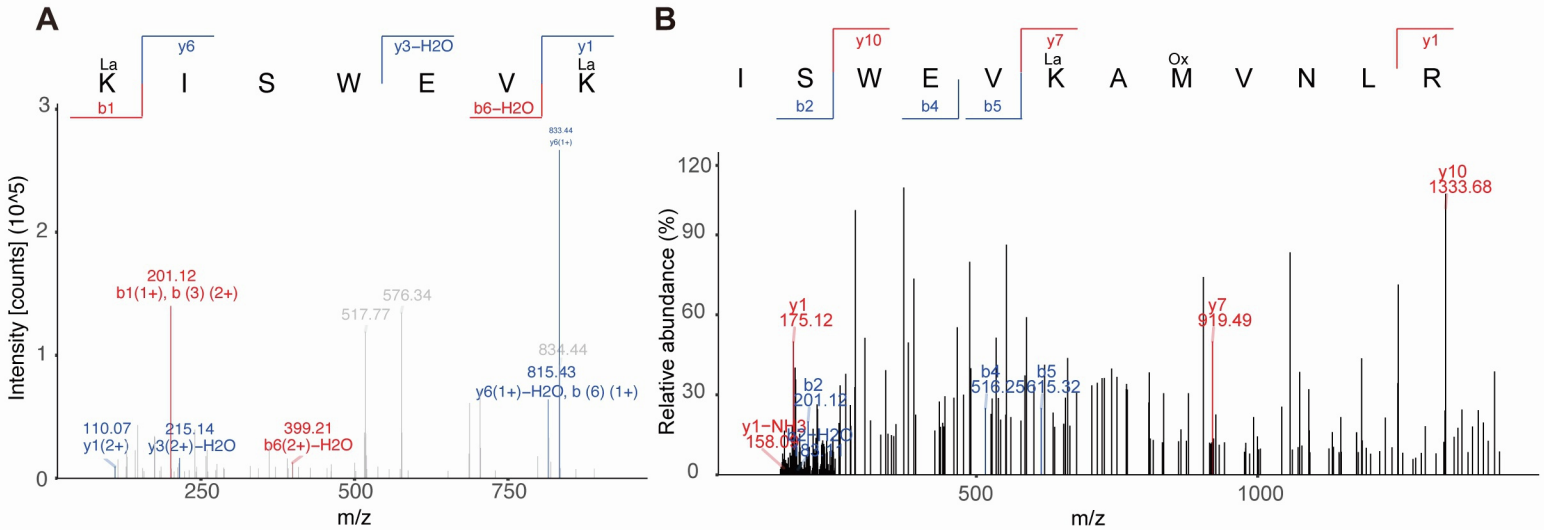
K. Strategy for generating RIPK3-K63R knock-in mice. Schematic representation of the RIPK3-K63R mutation strategy. Lysine at position 63 was replaced with arginine. The upper panel shows the targeting strategy and the nucleotide substitutions (AAG → CGC); the middle panel indicates the position of K63 within the protein kinase domain; the lower panel shows Sanger sequencing chromatograms confirming the mutation.

L–N. RIPK3-K63R mutation reduces necroptosis in primary MEF and BMDM cells. Cell death was assessed by ATP-based viability assay. n = 3 mice per genotype. Treatment conditions: TNFα (50 ng/mL), CHX (1 μg/mL), z-VAD (20 μM), LPS (100 ng/mL), and Poly(I:C) (50 ng/mL).**L**. Time-course analysis of necroptosis in primary mouse embryonic fibroblasts (MEFs) treated with T/C/Z (TNFα/cycloheximide/z-VAD). **M**. Time-course analysis of necroptosis in bone marrow-derived macrophages (BMDMs) treated with LPS + z-VAD. **N**. Necroptosis analysis in BMDMs treated with Poly(I:C) + z-VAD.**O**. RIPK3-K63R mutation abolishes RIPK3 lactylation in primary MEF cells.

Primary MEFs isolated from WT and RIPK3-K63R knock-in mice were treated with T/C/Z for 6 h. Lysates were immunoprecipitated with an anti-pan-Kla antibody or control IgG and immunoblotted for RIPK3.

P. Histological assessment of intestinal tissue injury. **Left**: Representative H&E-stained Swiss-roll sections of small intestine from WT and RIPK3-K63R mice, collected at death or at the experimental endpoint after intravenous TNFα injection (430 ng/kg). Scale bar: 100 μm. **Right**: Quantification of intestinal pathology injury scores. n = 7 mice per group.

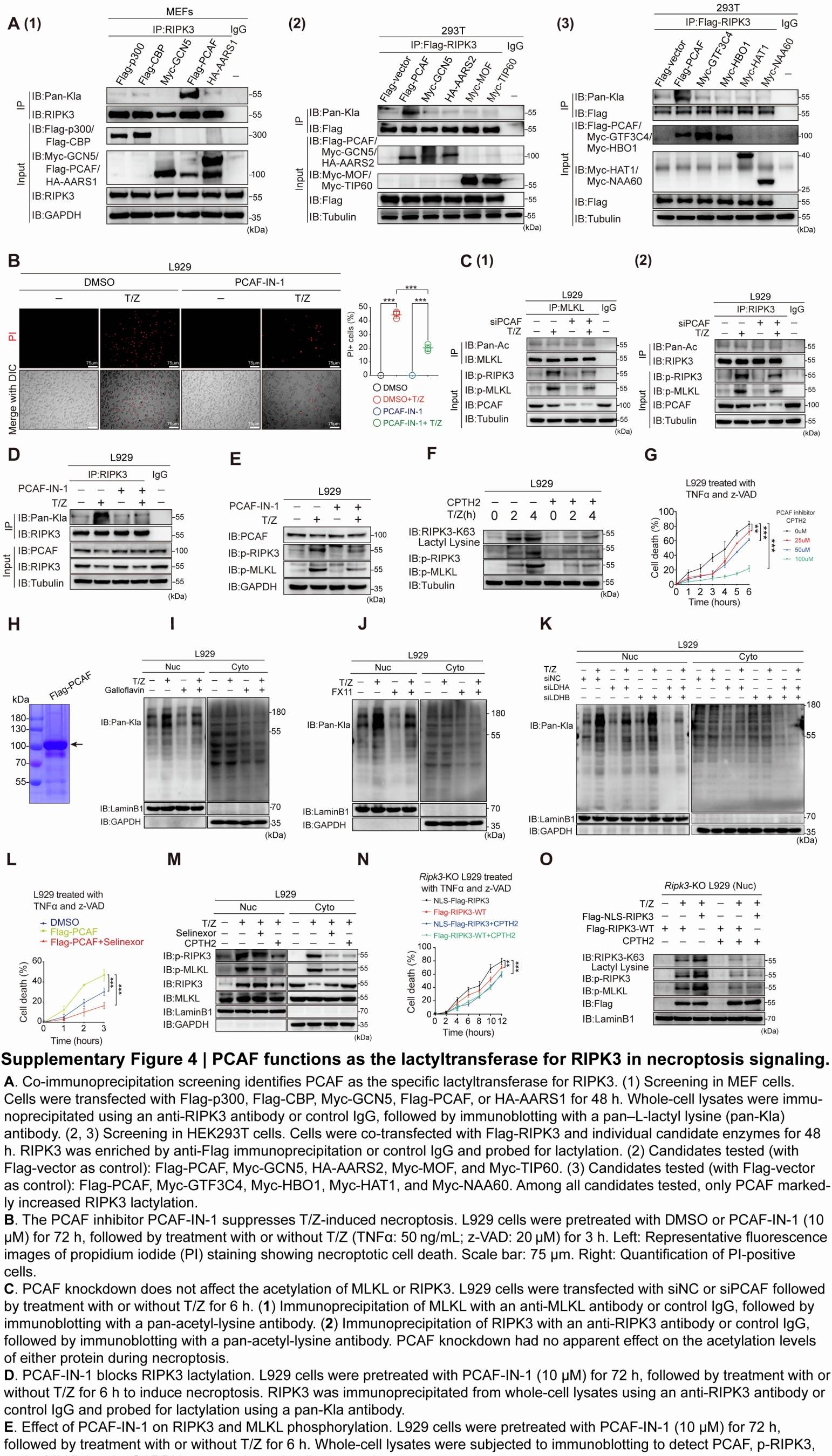
Data are presented as mean ± SD; individual data points represent independent experiments (**I, J**) or individual mice (**P**). Statistical analysis for **E, F (1), F (2),** and **L–N** was performed using two-way ANOVA with Bonferroni's multiple comparisons test; **I, J,** and **P** were analyzed using unpaired two-tailed t test with Welch's correction. ns, not significant; **, $p < 0.01$; ***, $p < 0.001$. Unless otherwise indicated, n = 3 independent experiments. In vitro experiments were repeated at least three independent times; statistical analysis was conducted on pooled data from all replicates.



Supplementary Figure 3 | Complementary mass spectrometry identification of endogenous RIPK3 K63 lactylation.

A. Non-targeted DDA LC-MS/MS spectrum of the endogenous RIPK3 lactylated peptide (Kla)ISWEV(Kla). The lactylated peptide (Kla)ISWEV(Kla) was detected from nuclear-enriched RIPK3 immunoprecipitated from T/Z (TNFα: 50 ng/mL; z-VAD: 20 μM) -treated L929 cells undergoing necroptosis. The x-axis represents m/z; the y-axis represents ion intensity (counts, $\times 10^5$). Matched y-type fragment ions are annotated above the peptide sequence (blue), including y6(1+) at m/z 833.44 (highest-intensity fragment), y3(2+)−H_2O at m/z 215.14, and y1(2+) at m/z 110.07, with the associated neutral-loss ion y6(1+)−H_2O at m/z 815.43. b-type ions (red) are also annotated, including b1 at m/z 201.12 and b6(2+)−H_2O at m/z 399.21.

B. Targeted PRM LC-MS/MS spectrum confirming endogenous RIPK3 K63 lactylation. Endogenous RIPK3 was immunoprecipitated from T/Z-treated L929 cells undergoing necroptosis and subjected to on-bead trypsin digestion. Tryptic peptides were analyzed by PRM on an Orbitrap Astral. The MS/MS spectrum identifies the lactylated peptide ISWEV(Kla)AM(Ox)VNLR (aa 58–69). The x-axis represents m/z; the y-axis represents relative abundance (%). Matched fragment ions are annotated above the peptide sequence, including b-ions (blue; b2: 201.12, b4, b5: 516.25/615.32) and y-ions (red; y1: 175.12, y1-NH_3: 158.09, y7: 919.49, y10: 1333.68), with y7 at m/z 919.49 and the dominant y10 at m/z 1333.68 confirming the intact lactylated peptide sequence. As K63 is the sole lysine residue within this tryptic peptide, the lactylation is unambiguously localized to K63 of RIPK3.



Supplementary Figure 4 | PCAF functions as the lactyltransferase for RIPK3 in necroptosis signaling.

A. Co-immunoprecipitation screening identifies PCAF as the specific lactyltransferase for RIPK3. (1) Screening in MEF cells. Cells were transfected with Flag-p300, Flag-CBP, Myc-GCN5, Flag-PCAF, or HA-AARS1 for 48 h. Whole-cell lysates were immunoprecipitated using an anti-RIPK3 antibody or control IgG, followed by immunoblotting with a pan–L-lactyl lysine (pan-Kla) antibody. (2, 3) Screening in HEK293T cells. Cells were co-transfected with Flag-RIPK3 and individual candidate enzymes for 48 h. RIPK3 was enriched by anti-Flag immunoprecipitation or control IgG and probed for lactylation. (2) Candidates tested (with Flag-vector as control): Flag-PCAF, Myc-GCN5, HA-AARS2, Myc-MOF, and Myc-TIP60. (3) Candidates tested (with Flag-vector as control): Flag-PCAF, Myc-GTF3C4, Myc-HBO1, Myc-HAT1, and Myc-NAA60. Among all candidates tested, only PCAF markedly increased RIPK3 lactylation.

B. The PCAF inhibitor PCAF-IN-1 suppresses T/Z-induced necroptosis. L929 cells were pretreated with DMSO or PCAF-IN-1 (10 μM) for 72 h, followed by treatment with or without T/Z (TNFα: 50 ng/mL; z-VAD: 20 μM) for 3 h. Left: Representative fluorescence images of propidium iodide (PI) staining showing necroptotic cell death. Scale bar: 75 μm. Right: Quantification of PI-positive cells.

C. PCAF knockdown does not affect the acetylation of MLKL or RIPK3. L929 cells were transfected with siNC or siPCAF followed by treatment with or without T/Z for 6 h. (**1**) Immunoprecipitation of MLKL with an anti-MLKL antibody or control IgG, followed by immunoblotting with a pan-acetyl-lysine antibody. (**2**) Immunoprecipitation of RIPK3 with an anti-RIPK3 antibody or control IgG, followed by immunoblotting with a pan-acetyl-lysine antibody. PCAF knockdown had no apparent effect on the acetylation levels of either protein during necroptosis.

D. PCAF-IN-1 blocks RIPK3 lactylation. L929 cells were pretreated with PCAF-IN-1 (10 μM) for 72 h, followed by treatment with or without T/Z for 6 h to induce necroptosis. RIPK3 was immunoprecipitated from whole-cell lysates using an anti-RIPK3 antibody or control IgG and probed for lactylation using a pan-Kla antibody.

E. Effect of PCAF-IN-1 on RIPK3 and MLKL phosphorylation. L929 cells were pretreated with PCAF-IN-1 (10 μM) for 72 h, followed by treatment with or without T/Z for 6 h. Whole-cell lysates were subjected to immunoblotting to detect PCAF, p-RIPK3, and p-MLKL levels. GAPDH was used as a loading control.

F. Immunoblot analysis of RIPK3-K63 lactylation, p-RIPK3, and p-MLKL in L929 cells pretreated with the GCN5/PCAF inhibitor CPTH2 (100 μM) for 48 h, followed by T/Z treatment for 0, 2, or 4 h. Tubulin was used as a loading control.

G. CPTH2 dose-dependently suppresses T/Z-induced necroptosis. L929 cells were pretreated with the GCN5/PCAF inhibitor CPTH2 (0, 25, 50, or 100 μM) for 48 h and then treated with T/Z. Cell viability was assessed by ATP levels.

H. SDS-PAGE analysis of purified recombinant Flag-PCAF. N-terminally Flag-tagged PCAF was purified and resolved by SDS-PAGE, followed by Coomassie brilliant blue staining. The arrow indicates PCAF.

I–J. LDH inhibition reduces global protein lactylation in both nuclear and cytoplasmic fractions. Nuclear and cytoplasmic fractions were analyzed by immunoblotting for Pan-Kla. L929 cells were pre-treated with J, Galloflavin (100 μM) or J, FX11 (20 μM) for 24 h, followed by treatment with or without T/Z for 6 h. Lamin B1 and GAPDH served as nuclear and cytoplasmic controls, respectively.

K. Knockdown of LDHA and LDHB reduces global protein lactylation. L929 cells were transfected with siNC, siLDHA, siLDHB or siLDHA plus siLDHB, followed by treatment with or without T/Z (6 h). Nuclear (Nuc) and cytoplasmic (Cyto) fractions were analyzed by immunoblotting for global protein lactylation. Fractionation markers Lamin B1 (nuclear) and GAPDH (cytoplasmic) were used as controls.

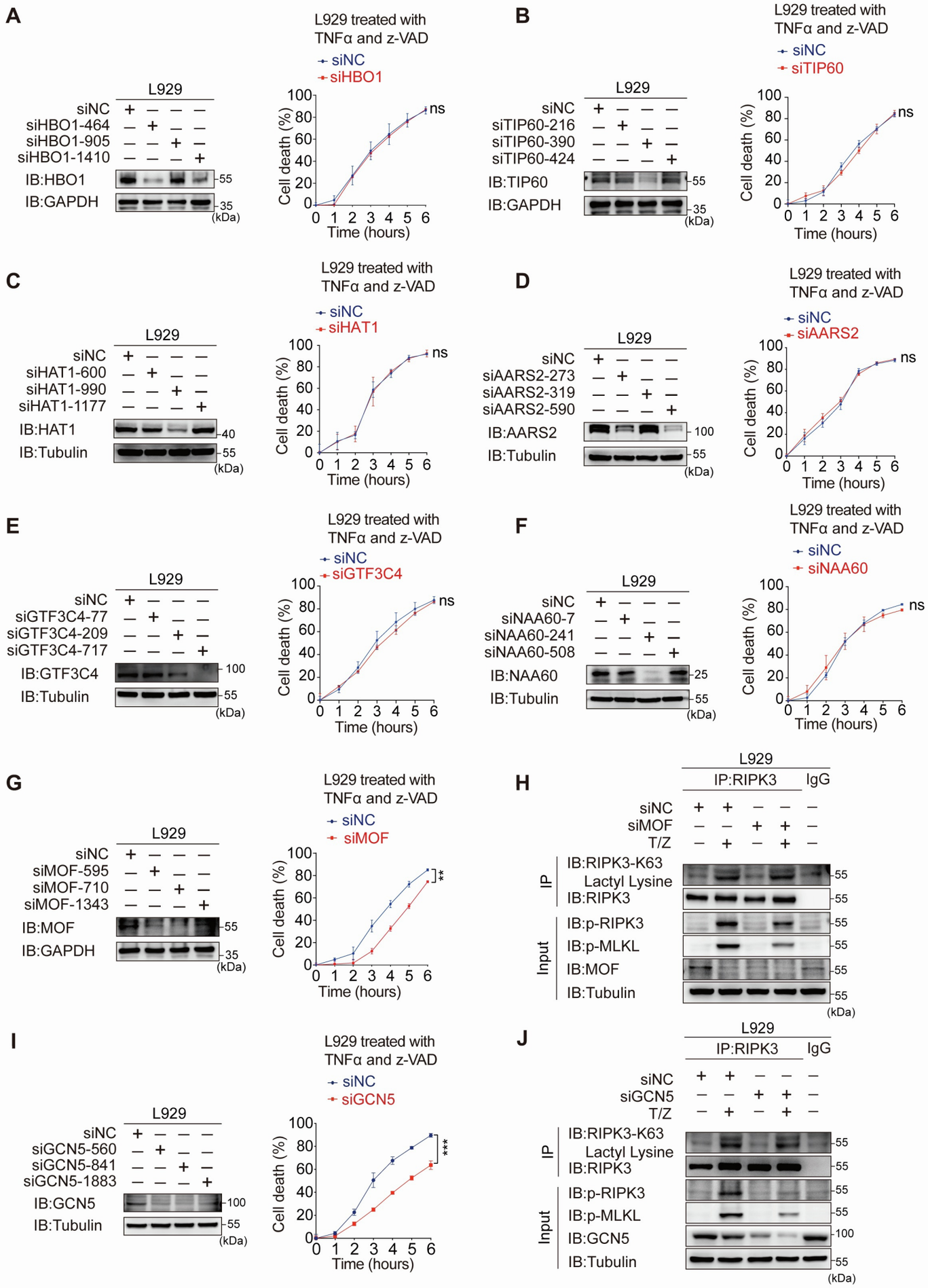
L. Overexpression of PCAF promoted T/Z-induced necroptosis, an effect reversed by Selinexor. L929 cells were transfected with Flag-vector or Flag-PCAF, with or without the nuclear export inhibitor Selinexor (10 μM, 24 h). Cell viability was assessed by ATP levels.

M. Blocking RIPK3 nuclear export reduced RIPK3 and MLKL phosphorylation, similar to CPTH2 treatment. L929 cells were treated with T/Z (6 h) in the presence or absence of Selinexor (10 μM, 24 h) or CPTH2 (100 μM, 48 h). Cytoplasmic and nuclear fractions were analyzed by immunoblotting for p-RIPK3, p-MLKL, RIPK3, and MLKL. Lamin B1 and GAPDH served as nuclear and cytoplasmic markers, respectively.

N. Ripk3-knockout L929 cells reconstituted with Flag-RIPK3-WT or nuclear-localized NLS-Flag-RIPK3 were treated with T/Z for the indicated times (0–12 h) in the presence or absence of CPTH2 (100 μM, 48 h). Cell viability was assessed by ATP levels.

O. Ripk3-knockout L929 cells reconstituted with Flag-RIPK3-WT or NLS-Flag-RIPK3 were treated with T/Z (6 h) in the presence or absence of CPTH2 (100 μM, 48 h). Nuclear (Nuc) fractions were analyzed by immunoblotting for RIPK3-K63 lactylation, p-RIPK3, p-MLKL, and Flag. Lamin B1 served as a nuclear marker.

Data are presented as mean ± SD; individual data points represent independent experiments. Statistical analysis for **B, G, L**, and **N** was performed using two-way ANOVA with Bonferroni's multiple comparisons test. **, $p < 0.01$; ***, $p < 0.001$. Unless otherwise indicated, n = 3 independent experiments. All experiments were repeated at least three independent times; statistical analysis was conducted on pooled data from all replicates.

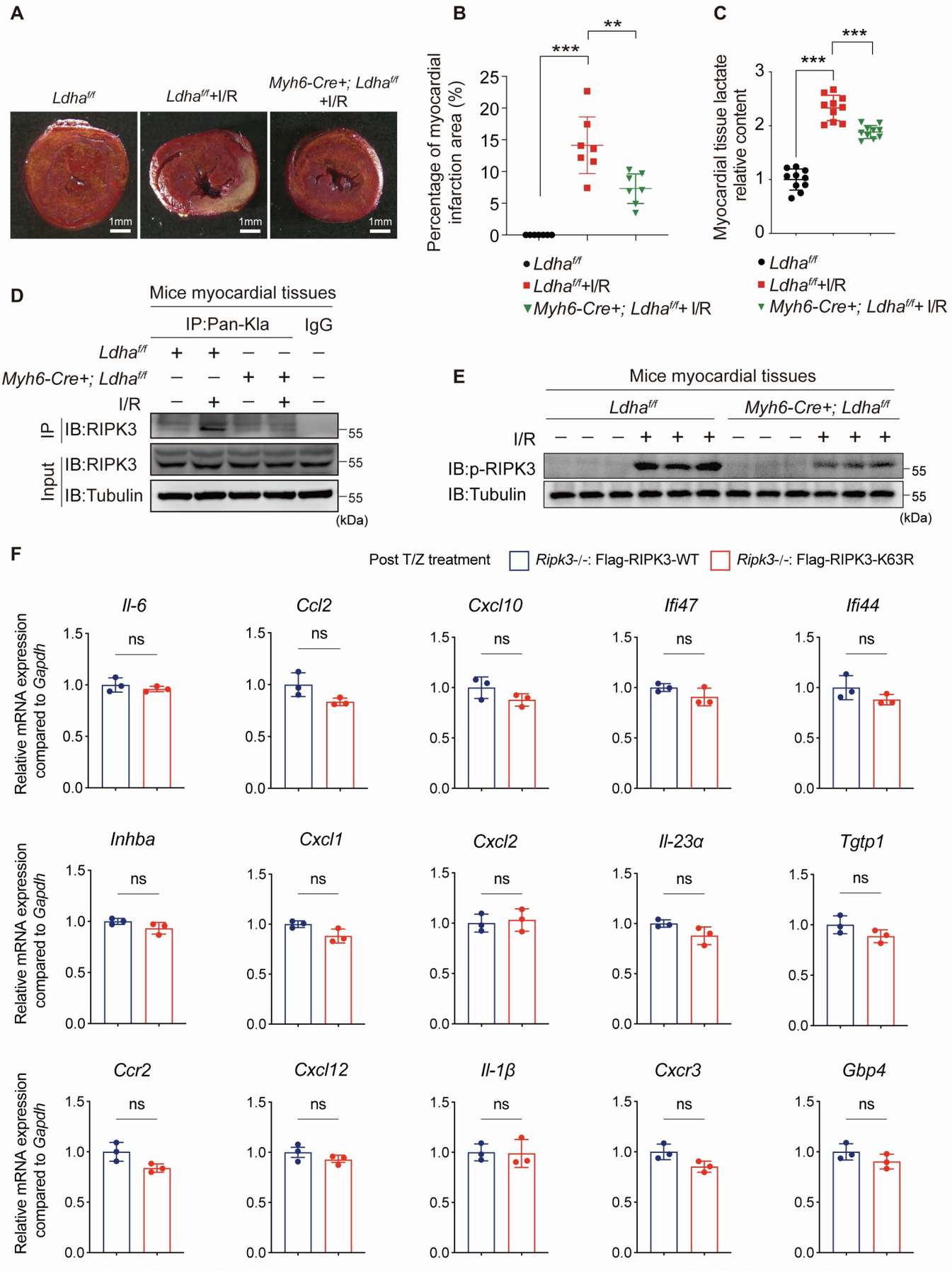


Supplementary Figure 5 | Other candidate enzymes do not contribute to RIPK3-K63 lactylation.

A–F. Knockdown efficiency and functional impact of candidate enzymes in necroptosis. L929 cells were transfected with each of three independent siRNAs targeting HBO1 (**A**), TIP60 (**B**), HAT1 (**C**), AARS2 (**D**), GTF3C4 (**E**), or NAA60 (**F**). **Left**: Immunoblot analysis showing knockdown efficiency of three independent siRNAs per gene. Tubulin or GAPDH served as loading controls. **Right**: Cell viability assessed by ATP levels following T/Z (TNFα: 50 ng/mL; z-VAD: 20 μM) treatment. The siRNA exhibiting the highest knockdown efficiency was selected for the functional assay (siHBO1-464, siTIP60-390, siHAT1-990, siAARS2-590, siGTF3C4-717, and siNAA60-241, respectively).

G–J. Knockdown of MOF or GCN5 attenuates necroptosis independently of RIPK3-K63 lactylation. (**G, I**) Knockdown validation and functional analysis. L929 cells were transfected with each of three independent siRNAs targeting MOF (**G**) or GCN5 (**I**). **Left**: Immunoblot analysis of knockdown efficiency. **Right**: Cell viability assessed by ATP levels using the most efficient siRNA (siMOF-710 and siGCN5-841, respectively). (**H, J**) Analysis of RIPK3 lactylation. Cells were transfected with the most efficient siRNA and treated with or without T/Z for 6 h. RIPK3 was immunoprecipitated using an anti-RIPK3 antibody or control IgG and immunoblotted with an anti-RIPK3-K63 lactyl-lysine antibody. MOF (**H**) or GCN5 (**J**) knockdown did not apparently alter RIPK3-K63 lactylation, despite reducing p-RIPK3 and p-MLKL levels in whole-cell lysates, indicating that MOF and GCN5 influence necroptosis through mechanisms independent of RIPK3-K63 lactylation.

Data are presented as mean ± SD; individual data points represent independent experiments. **A–G** and **I** were analyzed using two-way ANOVA with Bonferroni's multiple comparisons test. ns, not significant; **, $p < 0.01$; ***, $p < 0.001$. Unless otherwise indicated, n = 3 independent experiments. All experiments were repeated at least three independent times; statistical analysis was conducted on pooled data from all replicates.



Supplementary Figure 6 | LDHA knockout protects mice from lactylated RIPK3-dependent myocardial ischemia/reperfusion injury.

A. Representative images of TTC staining for infarcted areas in hearts from Ldha$^{f/f}$ and Myh6-Cre+; Ldha$^{f/f}$ mice with or without ischemia/reperfusion (I/R) injury (45 min ischemia followed by 4 h reperfusion). Hearts were collected immediately after reperfusion, frozen at −80°C for 10 min, and sectioned into 1–2 mm slices. Sections were incubated in 2% TTC at 37°C for 20 min in the dark. Scale bar: 1 mm.

B. Quantification of infarct size in hearts from Ldha$^{f/f}$ and Myh6-Cre+; Ldha$^{f/f}$ mice with or without I/R injury. Data are presented as mean ± SD. n = 7 mice per group.

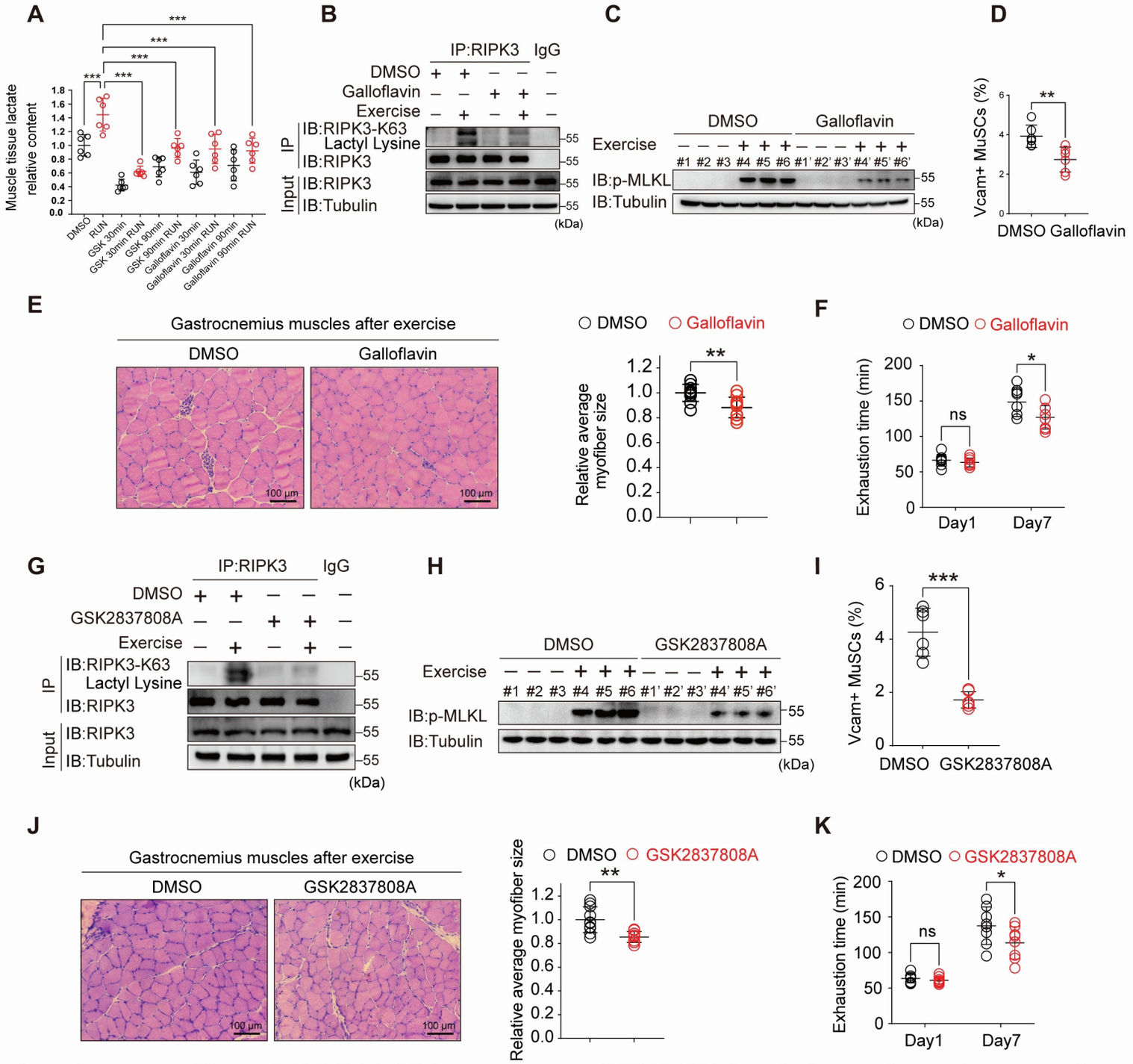
C. Measurement of relative lactate levels in myocardial tissues from Ldha$^{f/f}$ and Myh6-Cre+; Ldha$^{f/f}$ mice with or without I/R injury. Lactate content was normalized to the Ldha$^{f/f}$ group without I/R. n = 10 mice per group.

D. Effect of cardiomyocyte-specific Ldha knockout on RIPK3 lactylation. Whole heart tissue lysates from Ldha$^{f/f}$ and Myh6-Cre+; Ldha$^{f/f}$ mice with or without I/R injury were immunoprecipitated with an anti-Pan-Kla antibody or control IgG to enrich lactylated proteins, followed by immunoblotting for RIPK3. Tubulin was used as a loading control.

E. Immunoblot analysis of phosphorylated RIPK3 (p-RIPK3) in myocardial tissue from Ldha$^{f/f}$ and Myh6-Cre+; Ldha$^{f/f}$ mice with or without I/R injury. Lysates from three mice per condition were analyzed. Tubulin was used as a loading control.

F. Ripk3-knockout L929 cells were reconstituted with Flag-RIPK3-WT or Flag-RIPK3-K63R and treated with T/Z for 6 h. Total RNA was isolated, and relative mRNA levels were measured by qRT-PCR with Gapdh as internal control. For each independent experiment, cells from one independent culture dish were pooled prior to RNA extraction. Genes analyzed are shown in the figure. No significant difference was detected for any individual gene between RIPK3-WT– and RIPK3-K63R–reconstituted cells; P values were not adjusted for multiple comparisons.

Data are presented as mean ± SD; individual data points represent individual mice (**B, C**) or independent experiments (**F**). Statistical analysis for **B** and **C** was performed using one-way ANOVA with Bonferroni's multiple comparisons test; **F** was analyzed using unpaired two-tailed t test with Welch's correction. ns, not significant; **, $p < 0.01$; ***, $p < 0.001$. In vitro experiments were repeated at least three independent times; statistical analysis was conducted on pooled data from all replicates.



Supplementary Figure 7 | LDHA inhibitors suppress RIPK3-K63 lactylation and muscle stem cell activation in exercise-induced muscle remodeling.

A. LDH inhibition lowers baseline muscle lactate and attenuates its exercise-induced increase. Mice (8–10 weeks old) were acclimated to a motorized treadmill for three days. Mice were administered Galloflavin (50 mg/kg) or the LDHA-specific inhibitor GSK2837808A (40 mg/kg) via intramuscular injection, with DMSO serving as the vehicle control. Following a 30- or 90-min rest period, mice were subjected to treadmill running at 15 m/min for 30 min. Gastrocnemius muscles were harvested before and immediately after exercise, and tissue lactate levels were measured, normalized to protein concentration, and expressed relative to the vehicle group before exercise. n = 6 mice per group.

B–K. The effect of LDH inhibition on running endurance and muscle adaptation. Based on the results in **A**, mice were administered Galloflavin (**B–F**) or GSK2837808A (**G–K**) via intramuscular injection 30 min prior to each high-intensity running session, with DMSO-injected mice as controls. The exercise protocol included a 5-min warm-up at 5 m/min, followed by gradual increases (10 m/min for 10 min, 15 m/min for 30 min) and a final speed of 20 m/min until exhaustion. Muscle tissues were collected on day 7 after the exhaustion test for subsequent analyses. **B, G**. Effect of Galloflavin (**B**) and GSK2837808A (***G***) on RIPK3 lactylation in gastrocnemius muscle. Immunoprecipitation using an anti-RIPK3 antibody or control IgG was followed by immunoblotting with an anti-RIPK3-K63 lactyl-lysine antibody. Tubulin was used as a loading control. **C, H**. Immunoblot analysis of p-MLKL expression in gastrocnemius muscle from sedentary and exercised mice on day 7 following Galloflavin (**C**) or GSK2837808A (**H**) treatment. Each lane represents an individual mouse (n = 3 mice per condition). Tubulin served as the loading control. **D, I**. Flow cytometric analysis of muscle stem cells (MuSCs) in mice treated with Galloflavin (**D**) or GSK2837808A (**I**). Quantification of the percentage of MuSCs (SYTOX Green−CD11b−CD31−CD45−Sca1−Vcam+) among total digested mononuclear cells. n = 6 mice per group. **E, J**. Representative H&E staining of gastrocnemius muscle cross-sections (**Left**) and quantification of the average myofiber size (**Right**) collected after the exhaustion test on day 7 from Galloflavin- (**E**) or GSK2837808A-treated (**J**) mice. Myofiber size was normalized to the corresponding vehicle control. Scale bar: 100 μm. n = 10 mice per group. **F, K**. Running endurance assessed by time to exhaustion on days 1 and 7 in mice treated with Galloflavin (**F**) or GSK2837808A (**K**). n = 8 mice per group.

Data are presented as mean ± SD; individual data points represent individual mice. Statistical analysis for **A, F** and **K** were performed using two-way ANOVA with Bonferroni's multiple comparisons test; **D, E, I**, and **J** were analyzed using unpaired two-tailed t test with Welch's correction. ns, not significant; *, $p < 0.05$; **, $p < 0.01$; ***, $p < 0.001$.